Fabrication and modeling of SiGe Nanostructures Driven by Hetero-epitaxial Elasticity

Kailang Liu

THÈSE

présentée à

Ecole Centrale Marseille
Aix-Marseille Université

pour obtenir

LE GRADE DE DOCTEUR
ÈS

MATIÈRE CONDENSÉE et NANOSCIENCES

Fabrication and Modeling of SiGe Nanostructures Driven by Hetero-epitaxial Elasticity

---

par

Kailang Liu

soutenue le

16 Décembre 2016

devant le jury composé de

Chantal Fontaine	CNRS,Toulouse	Rapporteur
Frank Glas	CNRS,Paris	Rapporteur
Francesco Montalenti	UNIMIB, Milano	Examinateur
Julien Brault	CNRS, Valbonne	Examinateur
Peter Voorhees	Northwestern Univ. ,Evanston	Invité
Thomas Frisch	UNSA. , Nice	Invité
Antoine Ronda	CNRS, Marseille	Directeur de Thèse
Jean-Noël Aqua	UPMC, Paris	Directeur de Thèse
Isabelle Berbezier	CNRS, Marseille	Directeur de Thèse

IM2NP, Saint Jérôme Faculté, Marseille
INSP, Jussieu, Paris

To My Grandparents

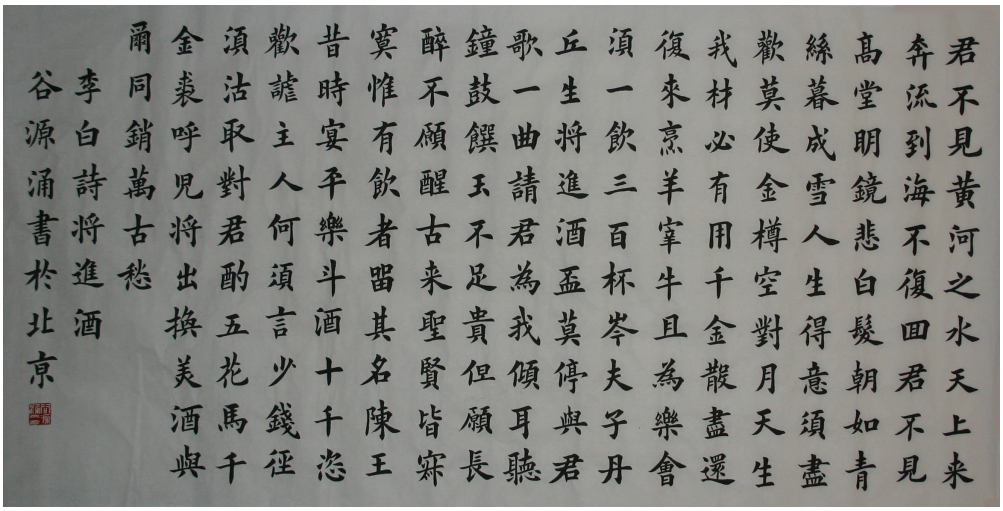

Acknowledgments

I would firstly thank my supervisors, Isabelle Berbezier, Jean-Noël Aqua and Antoine Ronda, for having given me the precious opportunity to study in France three years ago, which indeed opened the door to a much broader world, physical and spiritual. This eventually turned to the debut of this wonderful period of my life when I look back, and thank China Scholarship Council for offering the financial support while studying in France.

I am always very grateful that Isabelle kindly picked me up in Marseille airport, arranged my accommodation and introduced me to all the members in our group, which were really helpful at the beginning when I arrived like a lost child in France, only knowing "Merci" and "Bonjour". I would also like to say thanks to you for your patience, your generosities as well as the freedom you gave me in terms of scientific research, which allowed me to rapidly get familiar with our research topics in the group. I also appreciate your kindness, your encouragements and your inspiring responses with profound expertises every time when I was stocked by problems either in science or in life.

Many thanks of mine should also be dedicated to Jean-Noel for offering me the opportunity to find the charms of another face of scientific research, the modelling, which had been completely a new frontier for me. Thank you for your patience while teaching me the profound knowledge in physics and math, the ways of thinking, and the importance of rigorousness in research. In addition, I also appreciate the discussions with you on other diverse topics when I worked in Paris, from cultures to habits, from citizenship to politics...

Antoine is always warm-hearted when I have problems. Thank you so much for your kindness and forgiveness when I had wrongdoings in experiments or even broke some equipments. Thank you for your help and your professionalism as well as your huge efforts, having ensured our team always goes forward smoothly.

I feel very happy and thankful that all the members of jury for your time on reading my thesis and for your comments and advice. I acknowledge in particular Prof. Peter Voorhees for your fruitful and inspiring discussions and comments on our theoretical model.

I also want to thank Marco Abbarchi, Luc Favre ,Abdelmalek Benkouider and Meher Naffouti for your warm welcomes when I arrived, for your guides and helps in experiments, for your encouragements in research and for creating the wonderful , lively ,friendly and dynamic atmosphere in our team. Thank Jean-Benoït Claude for taking me everywhere with your lovely car, for discussing and playing football with me, for explaining everything I did not know. Special thanks go to Malek, Meher, Jean-benoït, Thomas David and others for keeping very patient to speak French with me from the very beginning, which surely has benefited me for my life here and will be benefiting me in the rest of my life.

I also want to express the gratitude to the literally new arrivals, who brought new research domains and innovative ideas and enormously enriched our research interests, including Professor David Grosso, Thomas Bottein, Elsa Alvarez, Tom Wood , Léo Métayer and Jérôme Loizillon. Thank the internship students for your helps and discussions. Among them are Mohamed, Maxime, Florian, Imen, Ibstisem ,Khawla...Thank all the members in our Lunch Organization for sharing globally diverse food.

Then I would like to thank the researcher and students in group "Physico-chimie et dynamique des surfaces " of lab INSP who helped me a lot when I worked in Paris, some of them are listed here: Geoffroy Prévot, Bernard Croset, Olivier Pluchery, Emmanuelle Lacaze, Nathalie Bonatout, Léo Bossard-Giannesini, Mattia Farronato, Danilo Longo, Alberto Curcella.

I also acknowledge the secretaries Sarah Mostefa, Michele Francia for your kindness and helps.

Many thanks go to those friends from China I met in France, including Bofei Peng, Wei Zhu, Haiying Du, Shihe Long, Zhiqing Kui, Rui Liu, Di Gao, Wei Liu, Lili Pu, Anqi Li et al. The homesick has been relieved because of your companions, your food and the time we spent together. I would particularly say thanks to Zuo Kerong for her sincerity of sharing her stories and feelings with me, and for what we have done together and what we have experienced together.

No words would really be appropriate to express my grateful feelings to my families. It is your expectations and supports that constantly motivate me all the way. All what I do is merely to make you proud.

Thank all the persons unnamed here.

Merci

Fabrication and modeling of SiGe Nanostructures Driven by Hetero-epitaxial Elasticity

Abstract

We investigate here the heteroepitaxy of silicon-germanium (SiGe), a system which is commonly regarded as the stereotype of semiconductor epitaxy. While this system has already attracted a tremendous amount of attention due to its applications for band-gap engineering in microelectronic industry, the major challenge facing the development of new SiGe-based devices remains the controllable epitaxial growth of self-assembled nanostructures. It is well-known that SiGe follows a Stranski-Krastanov growth mode, which proceeds via the growth of bi-dimensionnal layers followed by the growth of three-dimensional islands. Under this generic "Stranski-Krastanov" designation, several different behaviors can be identified. An overall understanding of all these behavior is still partially missing due to the complexity and the interplay of kinetics and energetic driving forces, preventing the development of new devices.

In this work we focus on the self-assembly of SiGe nanostructures following the quest of light emission for integrated Si-based photonic, optoelectronic and nanoelectronic devices.

Even if the innovation in Si-based devices has been boosted recently by the development of ultra-thin body fully depleted silicon on insulator transistors, a real breakthrough would be the demonstration of light emission and/or absorption by group IV elements since it allows the convenient integration into the nowadays semiconductors.

In this work we first demonstrate the different growth regimes of strained films, i.e. instability versus nucleation regimes. We develop a model which resolves the race of these two growth pathways and unveil the mechanisms of different modes of morphological evolution driven by elasticity.

In the second part, we examine in details the natural self-organisation of coherent islands. The direct elastic effect induces repulsion between coherent islands. However, the strain-dependent surface energy which has been overlooked previously in analysis of the island-island interaction is revealed to cause an attraction between islands. It may compensate the direct elastic repulsion during the initial state of nucleation and lead to the clustering of coherent islands.

In a third part we study the influence of miscut steps of vicinal substrate on the formation and self-organisation of islands. We demonstrate that the strain relaxation anisotropy produced by the step edges, is at the origin of the instability elongation perpendicular to steps. Quantitative agreement between the instability elongation and the anisotropy of strain relaxation is found, which deepens the understandings of hetero-epitaxial growth on vicinal substrate.

In the fourth part we develop a new process based on Ge condensation during thermal oxidation of dilute SiGe. The kinetics of SiGe condensation process is investigated and the fully strained SiGe epilayer is fabricated via this particular condensation process. This process can be applied in fabrication of SiGe core-shell nanostructures, for which the direct deposition and growth process is found to be cumbersome in terms of the control of morphology and composition.

As a whole, we studied the nanostructures of SiGe driven by its hetero-epitaxial elasticity. We proposed a model to compare two pathways of morphological evolution of SK growth and unearthed the mechanisms of the race and transition. We studied kinetics of island nucleation under the impact of elastic filed produced by an existing island. The peculiar role of strain-dependent surface energy is highlighted. Then the elasticity anisotropy induced by miscut steps on vicinal substrate is studied theoretically and experimentally. This anisotropy effectively induces the elongation of islands in one direction to form nanowires in good alignment. Then the kinetics of condensation of SiGe is studied, which is found to be an effective method in fabricating strained SiGe nanostructures.

Key Words: Si, Ge, Epitaxy, Strain, Nucleation, Quantum Dots

Contents

Chapter 1

SiGe Epitaxy and SiGe Quantum Dots

Contents

In the early stages, epitaxial growth of SiGe on Si substrate attracted tremendous research interests due to its promising applications in semiconductor integrated circuit (IC) industry; then the interests have been soaring with the development of new devices based on the strained SiGe quantum wells, superlattices or quantum dots, answering to another hot demand,the so-called strain engineering which aims at tuning the physical properties through the strain induced by lattice mismatch between SiGe and Si. On the other hand, SiGe/Si system is regarded as a prototype generic simple system that can serve to extract universal laws describing the hetero-epitaxial growth of semiconductor nanostructures where the growth is tuned significantly by both the strain field and the kinetics. Hetero-epitaxy stands as a widely-used fundamental technique to fabricate devices in electronics, optics, spintronics etc. In this part we will give an overall review on the fundamentals of SiGe hetero-epitaxial growth, the formation mechanism of SiGe QDs and their self-organization on nominal, vicinal and patterned substrates. This state of the art of this research domain will serve as the starting point of my work.

1.1 Importance of Semiconductor Epitaxy for applications and Fundamental Research

The technique of epitaxial growth has been one of cornerstones supporting the whole semiconductor industry since its emergence in early 1960s[1].In a semiconductor device, high-quality crystalline stacking layers and interfaces offer the possibilities to control the flow and confinement of charge carriers or photons, see Figure 1.1. Almost all these staking layers and functional interfaces are assembled via homoepitaxy(Material A on Material A) and hetroepitaxy(Material A on Material B). One good example to demonstrate the importance of high-quality crystalline epitaxy for a semiconductor device is the creation of blue LED (Light-Emitting Diode), for which Isamu Akasaki, Hiroshi Amano and Shuji Nakamura were rewarded the Nobel Prize in Physics in 2014. They would never be able to make a functioning device without the success in fabricating low-dislocation Nitrides(AlGaN, InGaN)single-crystalline layer on Sapphire thanks to the availability of growth techniques like MBE (Molecule Beam Epitaxy) and MOVPE (Metalorganic Vapour Phase Epitaxy)[2][3].

Along with advancements in high vacuum and purification of materials(mainly for the source materials) and the observation techniques like scanning microscopy including AFM (Atomic Force Microscopy),STM (Scanning Tunneling Microscope) and XRD (X-ray Diffraction) as well as in-situ observation techniques like RHEED (Reflection High Energy Electron Diffraction) and LEEM (Low Energy Electron Microscopy), allowing an ultimate nano-analysis of deposited thin films, a large number of material series can be effectively fabricated by hetero-epitaxy, including IV–IV systems (Si, Ge,

Sn...), III(Ga, In, Al)–V(As, N, Sb) systems and their alloys[4, 5], the II–VI systems(Zn, Cu, O, S...)[6]. Their electronic and optoelectronic features are widely used for in applications, especially in designing innovative electronics, optoelectronic devices, high-efficient catalysts and solar cells etc.

Among these materials, the epitaxy of Si and Ge stands as the very special one.

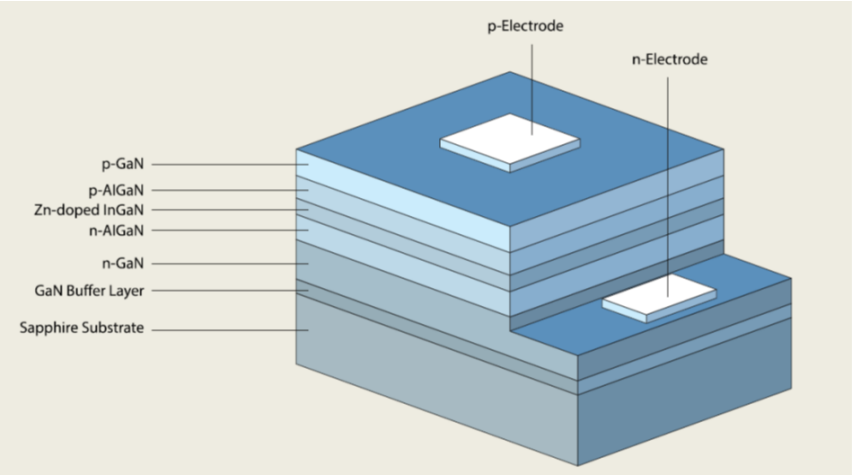

Figure 1.1: Schematic structure of the first blue LED[2]

1.2 Interests of Ge integrating onto Si

1.2.1 Si and Ge in semiconductor industry

Si is the ground on which all the nowadays semiconductor industry and our so-called Information Age are constructed. In the last decades, the advancement of Si processing and manufacturing techniques witnessed or defined the progress of semiconductor industry, the trajectory of which can be evidenced by Moore's law.

Ge, instead of Si, was the first semiconductor element chosen to manufacture almost all the solid-state devices just after the birth of transistors in 1950s. Until 1960s, Si took over Ge as the dominant industry material thanks to the discovery of SiO_2 dielectric passivation and the creation of MOSFET(Metal-Oxide-Semiconductor Field-Effect Transistor).

Recently in order to extend Moore's law, Ge is regarded by the semiconductor industry as a very promising alternative channel material of Si on the way to increase the charge-carrier mobility thence increase the performance of silicon transistors, because Ge has the highest hole mobility in all ever-known semiconductors, see 1.2b[7]. Another reason why Ge attracts enormous research interests from academies and industries is that it is technically convenient to integrate Ge into the Si-based industrial manufacturing processes owing to their similar properties, making it economically attractive to the semiconductor industry.

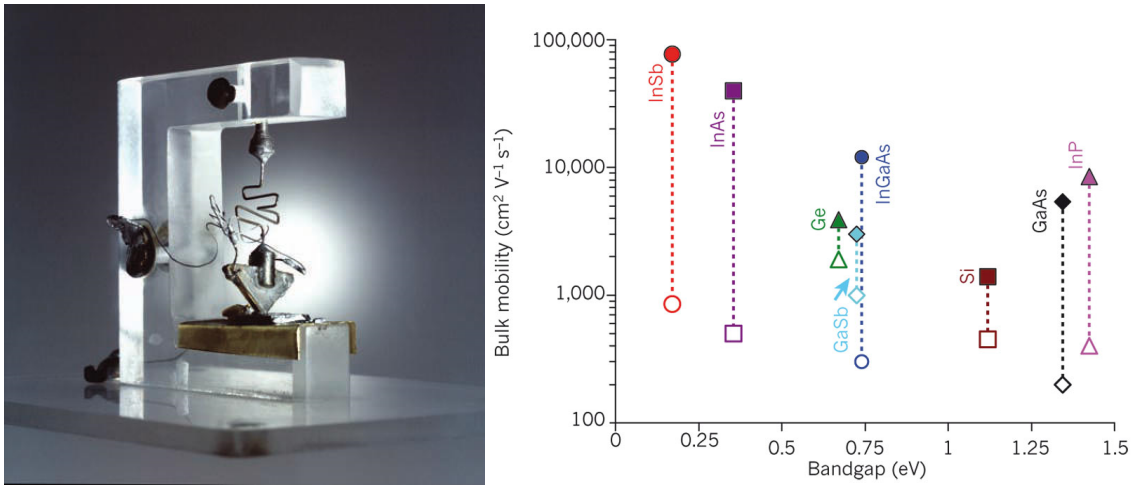

(a) **(b)**

Figure 1.2: (a)The first transistor in the world made of Ge. (b) The mobility landscape of semiconductors. The bulk mobility is plotted against the bandgap for silicon, germanium and a variety of group III–V materials. Filled symbols indicate electrons, and open symbolsindicate holes. Germanium offers the highest hole mobility of any known semiconductor material[7],

1.2.2 Si and Ge in nanodevices

In addition to be an alternative channel materials in Si transistors, the heteroepitaxy of Si and Ge produced lots of novel nanostructures including quantum wells(superlattices),nanowires, quantum dots, which confine the electrons in one, two and three dimensions respectively, tailoring their electron band structures and other properties. Embedded in these heteroepitaxial quantum structures is the effect of epitaxial strain, which turns to be a promising parameter to engineer various physical properties. This is normally called strain engineering. High strain can significantly tune the physical properties of materials. Such a high strain is impossible for bulk materials to sustain as the epitaxial strain is even higher than their yield strength. However the reduction of size to nanometric scale in nanodevices, characterized by the maxim "Smaller is Stronger" remarkably strengthens the materials[8]. Taking advantage of the epitaxial strain bewteen Si and Ge, strain engineering has succeeded in the applications in CMOS to increase charge- carrier mobility. Applying this epitaxial strain to Si on relaxed buffer SiGe layer,provides an increase of Si mobility a few hundred percent[9][10], which ensured Moore's law to continue since mid-2000s up to now. Benefits to semiconductor companies of billions of dollars have been generated thanks to the commercialization of the tensile strained Si on SiGe epitaxy[8]. The band gap structure of Si and Ge can also be turned from indirect band gap to quasi-direct by band folding due to epitaxial strain. Indeed, one of the major technical bottlenecks is the indirect band gap of Si and Ge, which hinders their efficiency in optoeletronic devices applications. Via the strain applied by heteroepitaxy, Si and Ge with quasi-direct band gap may be created, paving the way to further applications in a broader range[11].

During the last decades, SiGe nanowires, multi-core-shell nanowires and SiGe quantum dots have shown very promising properties in a wide range of applications including transistors, memories, photovoltaics, laser, thermoelectrics, quantum computing etc..

Below, we firstly go back to the very debut and basic concepts of hetero-epitaxy of Si and Ge and we introduce the kinetics and thermodynamics of crystal growth during heteroepitaxy, since these fundamentals are the prerequisites to design and fabricate any SiGe device. Then the formation of self-organized SiGe quantum dots via heteroepitaxy will be emphasized and a detailed research state of the art will be given.

1.3 SiGe heteroepitaxy and SiGe QDs

1.3.1 Stranski-Krastanov Growth of SiGe epiatxy

As briefly mentioned above, hetero-epitaxy refers to a crystal growth process where a material (s) incoherently or coherently grows on a foreign substrate (f). Mainly depending on the lattice mismatch between material (s) and (f) ($\delta = (a_s - a_f)/a_s$), as well as their surface energy γ_s and γ_f , three major classes of growth modes are distinguished: Frank-van der Merve mode refers to two dimensional (2D) growth, Stranski-Krastanov(SK) mode features a two-step process with 2D growth followed by 3D growth via the 2D-3D transition while in Volmer-Weber mode three-dimensional (3D) islands form directly on the substrate without a wetting layer, see Figure A.1.

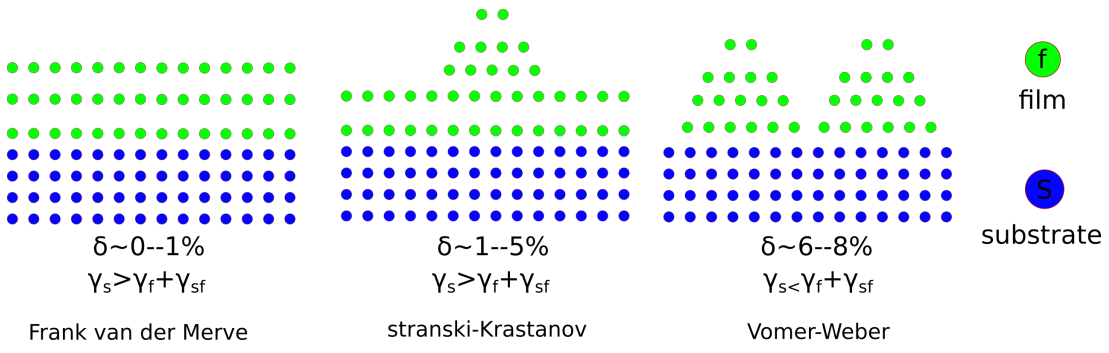

Figure 1.3: Different growth modes of epitaxy mainly resilting from mismatch δ

Si and Ge have the same diamond lattice structure but have different lattice constants (a_{Si} = 5.43 Å, a_{Ge} = 5.66 Å)[12]. Ge has a lattice mismatch $\delta = (a_{Ge} - a_{Si})/a_{Si}$ = 4.2% as compared to Si. Considering $Si_{1-x}Ge_x$ alloy is infinitely soluble, its lattice constant is then proportional to its composition x in an excellent approximation according to Vegard's law. Thence the lattice mismatch δ_x of $Si_{1-x}Ge_x$ on Si substrate can be written as:

$$\delta_x = \delta * x = x * 4.2\% \quad \textbf{(1.1)}$$

On Si(001) substrate, $Si_{1-x}Ge_x$ epitaxy follows the SK growth mode. As the deposition of $Si_{1-x}Ge_x$ starts, the surface undergoes a very complex process. The first stage can be seen as 2D layer or wetting layer growth. Afterwards the wetting layer reaches a critical thickness, the surface begins to roughen and 3D structures begin to form on the surface.

In the following part, we will follow this deposition pathway to demonstrate the SiGe epitaxial growth on Si(001) substrate.

1.3.2 Wetting layer growth

During the first stage of Ge deposition, the 2D wetting layer is stabilized by the reduction of surface energy since the deposition of Ge can dramatically decrease the surface energy of the system, which is quantitatively evidenced first-principle calculations[13], see Figure 1.4a. During the 2D wetting layer growth, the compressive strain induced by the lattice mismatch can be partially relaxed by intermixing, dimer vacancy line(DVL),see Figure 1.4b, and spontaneous formation of additional kinks and steps[14]. However

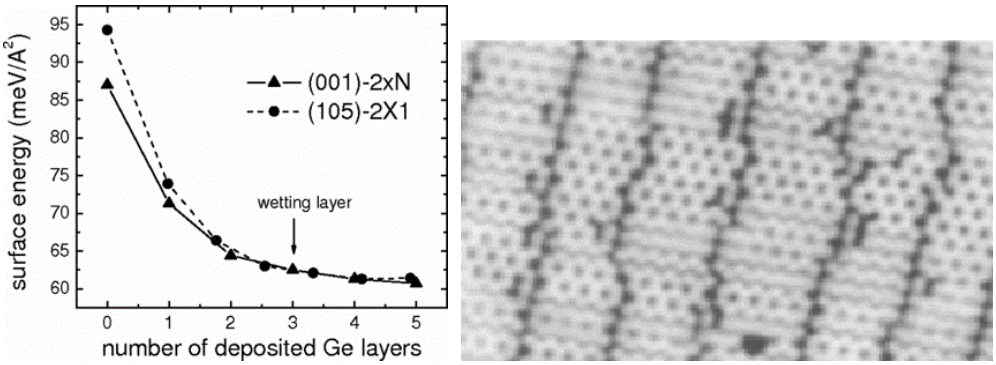

(a) **(b)**

Figure 1.4: (a) Surface energy as a function of the thickness of deposited Ge layers[15], (b)STM image of the Ge-covered Si(001) surface showing the $(2 \times n)$ reconstruction

these effects quickly saturate after depositing a few monolayers(about 3 monolayers), which is named the critical wetting layer thickness (h_c) , see Figure 1.4a. In the second step, 3D islands grow on the top of the wetting layer whose formation can continue to partially relax strain.

1.3.3 SiGe quantum dots

The highly strained epilayer finds new ways to relax the strain to reach a more stable state. Firstly the nucleation of dislocations, i.e. plastic relaxatio, is an effective way,Figure 1.5. However, the nucleation of dislocation should be suppressed for all the applications since dislocations are detrimental to all semiconductor devices. For this reason, ultra clean growth environment and careful control conditions are requested

as well. In this work, we thence focus only on the elastic relaxation. We have seen that when the the epilayer is thicker than h_c, a flat film can evolve from 2D to 3D islands, partially relaxing the strain and decrease the total energy of the system.

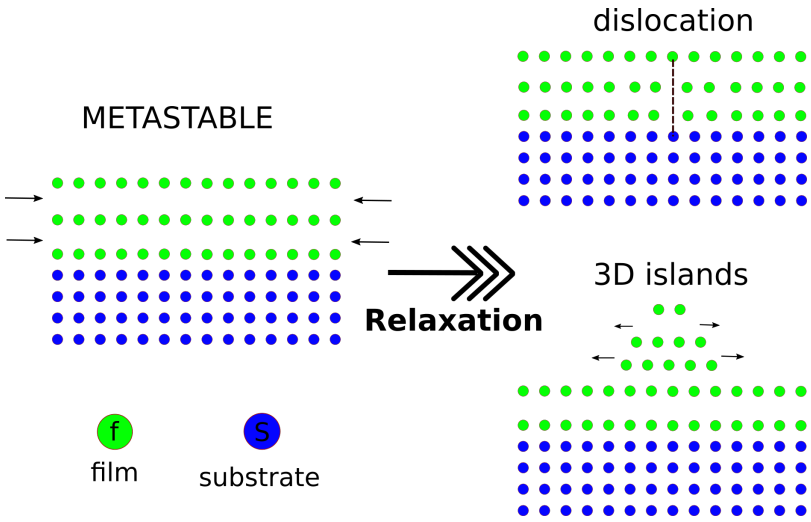

Figure 1.5: Schematic representation of the two ways followed by a strained epilayer to relax the strain: nucleation of dislocations and formation 3D islands respectively

Since 1990, the discovery by D.J.Eaglesham and M.Cerullo that this islands are free of dislocation at the first step of their formation, this research domain has attracted a huge amount of research interests. Indeed these nanometer-scale islands can be used as quantum dots. Furthermore, as the impurities or defects strongly degrade the physical properties of QDs, this approach of fabricating QDs is performed in clean-atmosphere chamber(for instance MBE) under ultrahigh vacuum and with monolayer precision in deposition rate, thence this approach opened a way to make ultra clean quantum dots[16].

For $Si_{1-x}Ge_x$ growth on Si(001) substrate, depending on strain level (composition x), one can find two different pathways of morphological evolution: nucleation of islands in high-strain regime and nucleationless formation of islands via ATG (Asaro-Tiller-Grinfeld) instability in low-strain regime.

Nucleation of islands in high-strain regime

Nucleation is the very first step in the phase change process via self-organization of atoms or molecules. It is a spontaneous process requiring systematic thermal fluctuations, which is ubiquitous ranging from the formation of bubbles in a glass of champagne to the formation of cloud[17]. During the deposition of Ge, with thickness above h_c, first 3D pre-pyramids nucleus nucleate stochastically on the wetting layer, Figure 1.6(c), and subsequently some of them grow into larger islands and some others shrink. The remaining nucleus immediately turn to (105) faceted pyramids or huts, see Figure 1.6(f).

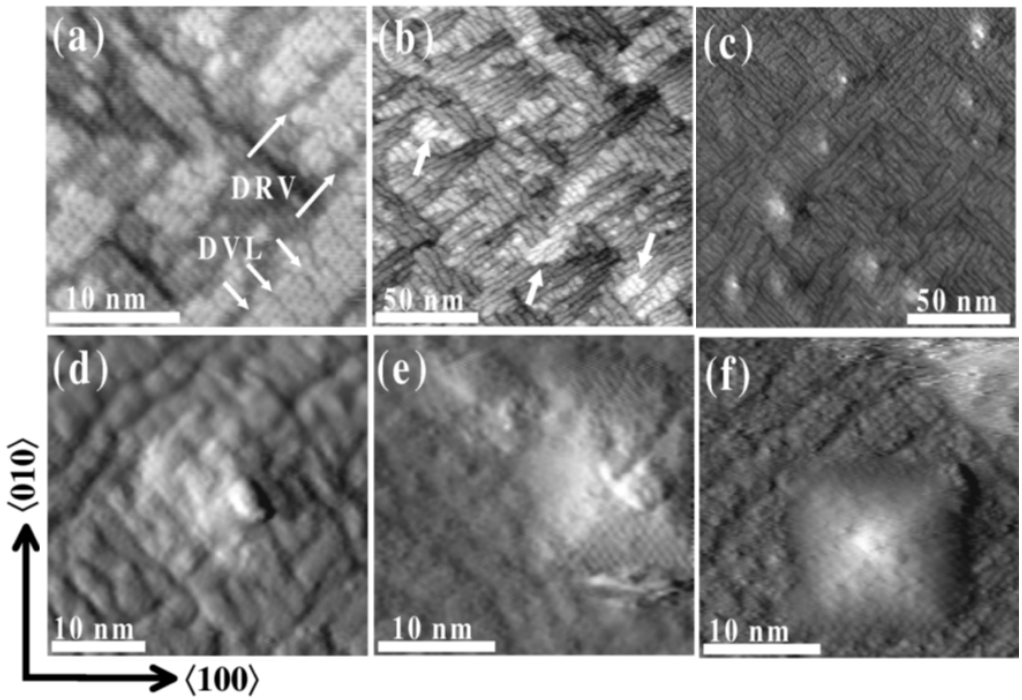

Figure 1.6: In-situ STM observation of the transition from 2D wetting layer to 3D island[18].

The formation of 3D islands is mainly driven by strain relaxation(ΔE^{el}) while still hindered by the energy cost of creating excess surfaces (ΔE^{s}) and edges between the facets (ΔE^{edge}). As a rough estimation, one would find that:

$$\Delta E^{el} \propto v \tag{1.2}$$

$$\Delta E^{s} \propto v^{2/3} \tag{1.3}$$

$$\Delta E^{edge} \propto v^{1/3} \tag{1.4}$$

where v is island volume. As a whole, the formation energies of island is written as:

$$\Delta E = \Delta E^{el} + \Delta E^{s} + \Delta E^{edge} \tag{1.5}$$

$$= A\,v + B\,v^{2/3} + C\,v^{1/3} \tag{1.6}$$

where A is negative, B, C are positive in principle. Finally the typical formation energy as a function of volume is plotted as in Figure 1.7, in which one can find the critical volume (V_c) and the energy barrier(ΔE_c) of island nucleation. According to the Classic Nucleation Theory, the nuclei size distribution follows Maxwell-Boltzmann distribution and those whose volume larger than (V_c) will grow and the rest will shrink. D. E. Jesson directly observed by in-situ STM, Ge clusters with size of some 270 atoms that formed and then shrank[19]. Nucleation sites are found to be at the vicinity of step edges as well as pits, where (V_c) and (ΔE_c) might be lowered[20].

The deposition and nucleation processes can be conveniently simulated via Kinetic Monte Carlo (KMC) method. The competition between deposition flux and diffusion flux F/D_f is found to control the island size and island density in the Solid-on-Solid (SOS) KMC simulations[21].

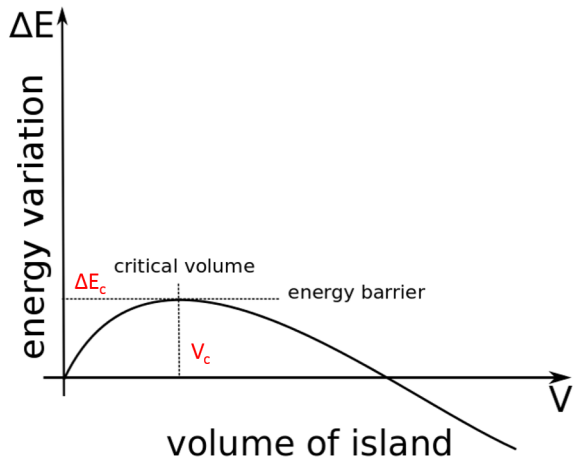

Figure 1.7: Typical formation energy of island as a function of its volume

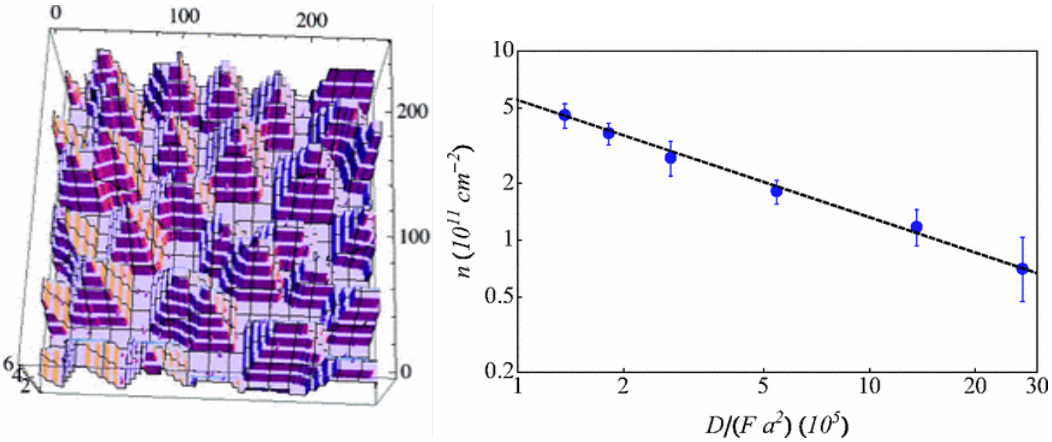

(a) **(b)**

Figure 1.8: KMC simulation of 3D islands (a) size, (b) density evolutions as a function of ratio diffusion constant over deposition flux at T = 500 K after deposition of 1.5 ML[21]

The (105) facets of the pyramid or hut islands are out of Wulff construction. Ab initio calculations have shown that (105) is stabilized by the reduction of surface energy due to its specific reconstruction.[22],[23].

For Ge epilayer(high strain regime), (105)-faceted islands (pyramid and hut) are often found unsustainable to the equilibrium state of epilayer due to its relatively low height-base-ratio($r = 0.1$). Such a shallow island is less effective than a dome or super dome ($r = 0.3$) in terms of elastic relaxation. This explains why during the subsequent Ge deposition, hut islands turn to domes and super domes[24].

ATG instability

In the low-strain regime, the 2D-3D transition shows a fully different scenario where the morphology roughens continuously and gradually on the whole surface. As a result

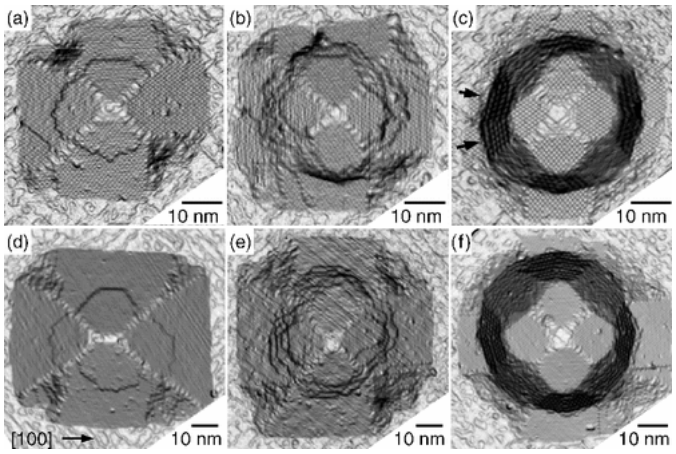

Figure 1.9: STM images of the transition from pyramid to domes during Ge deposition for increasing thickness[24]

of competition between elasticity and capillarity, a typical wavelength of the morphological roughening may be extracted from the long-range ordering[14][25], seeFigure 1.10.

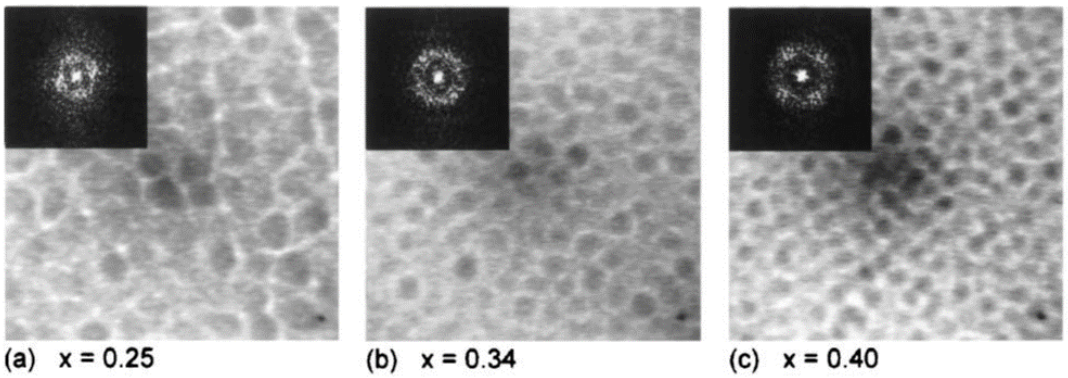

Figure 1.10: LEEM images of ATG istability in low-strain regime, for composition $x = 0.25, 0.34, 0.40$ respectively[25]

The mechanism of material transport is the surface diffusion driven by the local chemical potential gradients on the surface, which might be described through a continuum model. The epilayer is represented by morphological function $h(\mathbf{r}, t)$. A dynamic equation describing the morphological evolution can be written as Equation 1.7.

$$\partial h/\partial t = F + D\sqrt{1+|\nabla h|^2}\Delta_s \mu \tag{1.7}$$

where F is the deposition flux, D is the surface diffusion coefficient, Δ_s is the surface Laplacian and μ is the surface chemical potential including the contributions of surface energy and elastic energy[14]. In case of stationary evolution($F = 0$), a white noise perturbation $e^{i\mathbf{k}\cdot\mathbf{r}+\sigma t}$ on the surface will grow exponentially with growth rate(see Appendix B for details)

$$\sigma = |\mathbf{k}|^3 - \mathbf{k}^4 \tag{1.8}$$

in a dimensionless calculation, where the length scale and time scale are defined as:

$$l_0 = \frac{\gamma(1-\upsilon)}{2(1+\upsilon)Y\delta^2} \tag{1.9}$$

$$t_0 = \frac{l_0^4}{\gamma D} \tag{1.10}$$

where γ is the surface energy(constant at the initial state of ATG instability), υ is Poisson ratio, Y is shear Young's modulus and δ is mismatch.

The maximum growth rate σ_{max} is obtained when $k_{max} = 3/4$ corresponding to the typical wavelength of ATG instability

$$\lambda_{ATG} = \frac{2\pi}{k_{max}} l_0 = \frac{4\pi\gamma(1-\upsilon)}{3(1+\upsilon)Y\delta^2} \tag{1.11}$$

which evolves with misfit δ as $\lambda_{ATG} \propto \delta^{-2}$ when $F = 0$. The deposition flux F may induce a shift of the onset of ATG instability in unstationary case where F plays against the diffusion flux. This is demonstrated by P. Sutter and M. G. Lagally [26],see Figure 1.11.

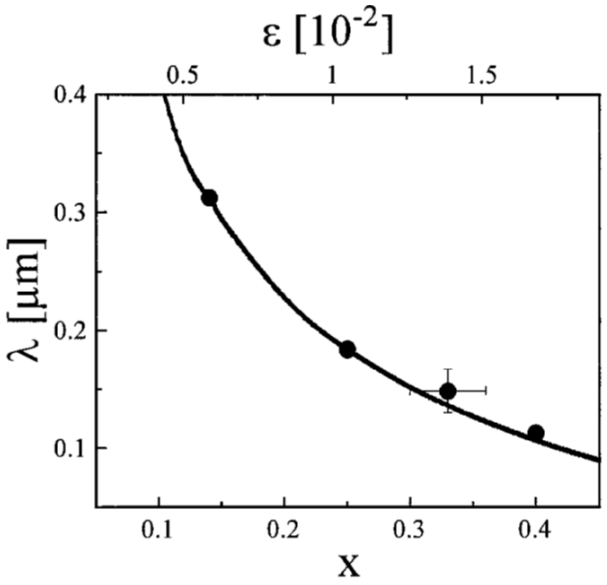

Figure 1.11: Dependence of ATG instability wavelength on composition x[26]

ATG instability builds long-range shallow undulations that turn to (105)-faceted pre-pyramids and eventually into hut islands during long-term annealing. Tersoff et al. proposed a continuum two-dimensional model taking into account the elastic energy, surface energy and corner edge energy. They predicted the main features of the transition from undulations to pyramid. The transient truncated pyramid was evidenced via in-situ STM observation[27].

The wetting effect in the SK growth plays a crucial role governing the kinetics and thermodynamics of 2D-3D transition of epilayer. A three-dimensional continuum model including elasticity, surface energy anisotropy and wetting effect proposed in the work

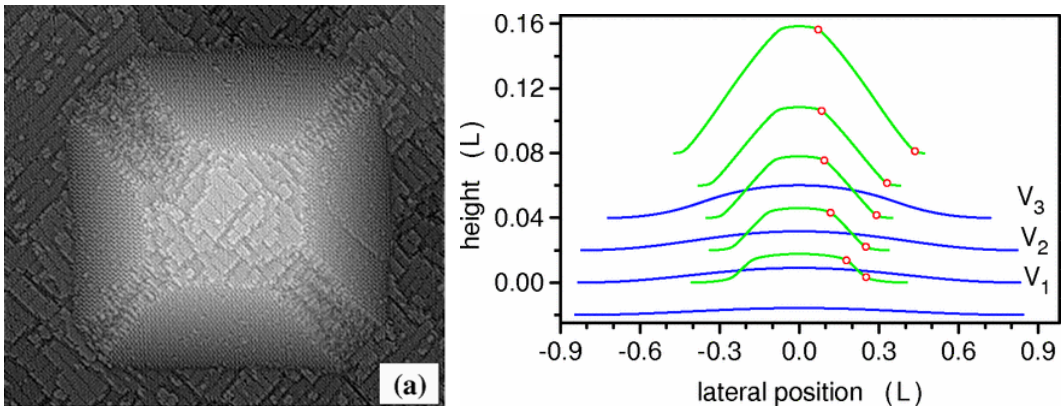

Figure 1.12: (a)STM image of truncated pyramidal island, (b) Schematic pathway of formation of faceted island

of Aqua et al. provided a quantitative description of the dynamics of epilayer evolution during long-time annealing[28]. In this model the non- linear effect of elasticity is elucidated in particular. It is shown that wetting effect enforces the stability of a epilayer thinner than critical thickness (h_c). The epilayer thicker than h_c begins to evolve via instability and kinetically interrupts when facet (105) form since the driving force for island coarsening vanishes. This interrupted coarsening is explained by the combination of wetting effect and surface energy anisotropy, in excellent agreement with experiments, seeFigure 1.13 and Figure 1.14.

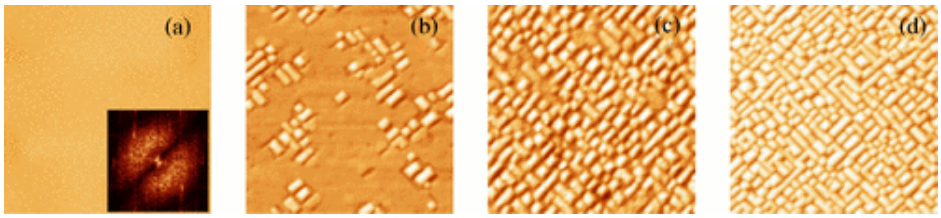

Figure 1.13: AFM images of a 5-nm-thin $Si_{0.70}Ge_{0.30}$ layer (a) as grown (Fourier transform in inset), (b) after 18-h annealing, and (c) after 54-h annealing at 550 °C . (d) Image of a 8nm film after 18h annealing. The ⟨110⟩ direction is horizontal. The scan area is $3\mu m \times 3\mu m$, and the vertical scale for all the images is 32 nm. [28]

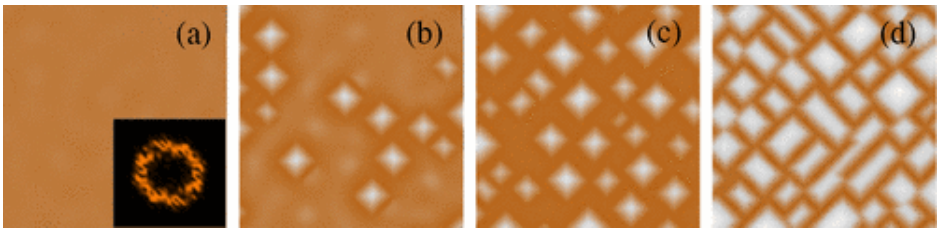

Figure 1.14: Numerical simulation of a surface for a 5-nm strained anisotropic film of $Si_{0.7}Ge_{0.3}$ (a) as-grown (Fourier transform in inset), after annealing time of (b) 18h, (c) 54h , and (d) simulation of a 8-nm film after 18h annealing. [The scan area is $1.2\mu m \times 1.2\mu m$, and the vertical scale is 31 nm.][28]

1.4 Controllable growth of SiGe quantum dots

1.4.1 Challenges toward applications

The physical properties of quantum dots profoundly depend on their size, composition ,even relative positions etc. However it is found that it is extremely difficult to control the self-organized growth of semiconductor quantum dots over large scale. First the size is difficult to control because the intermixing between deposited epilayer and substrate broadens the island size distribution [29]. Second the coexistence of various shapes (pyramid, hut, dome, superdome) on the same sample is often observed and third the islands nucleation is nearly random, see Figure 1.15a. In addition, the composition within an island is non-uniform. XRD and selective etching experiments showed different conclusions: it was reported that Ge tends to segregate onto the outer shell of domes, forming a Si-rich core and Ge-rich shell, see Figure 1.15b while other groups reported Ge-rich core and Si-rich shell. The intermixing for deposition for high growth temperature(>600 °C) allows to partially relax the strain and to decrease the entropy, which is crucial for high concentration epilayer(pure Ge). On the contrary, much less intermixing is found for the deposition of $Si_{1-x}Ge_x$ if $x < 0.6$ at relatively low temperature(<550 °C).

As a consequence, spontaneous quantum dots show large variety of characteristics, hindering their applications. Various approaches have been proposed to achieve the controllable growth of SiGe quantum dots.

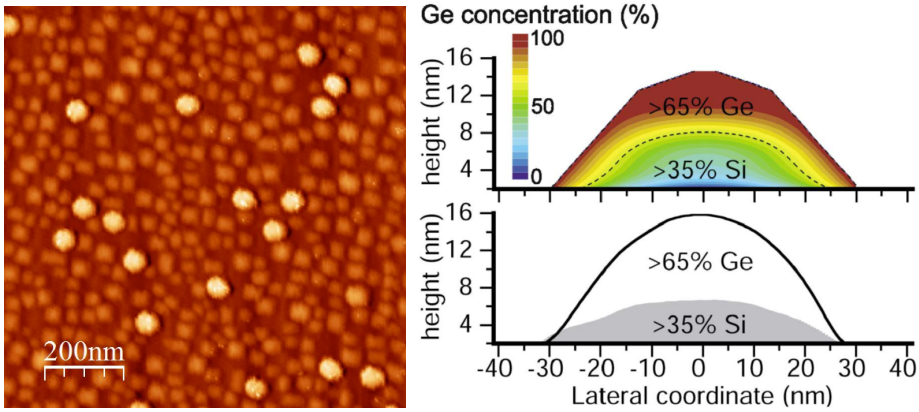

(a) **(b)**

Figure 1.15: (a) AFM image of spontaneous quantum dots through deposition of 1.9 nm $Si_{0.25}Ge_{0.75}$ on Si(001), unpublished result. (b) upper image is the real space chemical composition map for Ge domes; AFM line scans in lower image are taken on two Ge domes, before and after 31% H_2O_2 selective etching. It was concluded from these experiments that Si-rich core is present in the islands(The selective etching rate can be also dependent on strain state or crystallographic direction, which may modify these results).[29]

1.4.2 surfactants on substrate

The nucleation of 3D island is sensitive to its local environment and heterogeneous nucleation is always favorable than the homogeneous. The impurity atoms on the substrate can create nucleation sites in thermodynamic point of view. Furthermore the presence of surfactants segregating on the surface would influence the mobility of adatoms and kinetically change the nucleation of islands. Carbon-mediated growth of Ge was found to be an effective way to decrease the island size and increase island density. In this case, the C atoms act as nucleation centers for Si atoms decelerate and they decrease their diffusion length and suppress the intermixing of SiGe, thence increasing the Ge concentration in island. This has been reported to lead to the formation of smaller island[14].

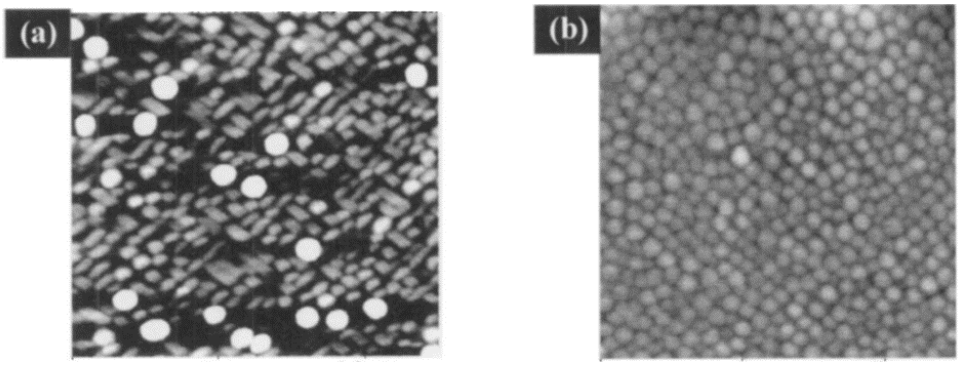

Figure 1.16: AFM image of 13ML Ge on (a) Si(001) and (b) with 1/2ML Sb on Si(001)[30]

A. Portavoce et al. investigated the influence of Sb surfactant on Si(001) on the for-

mation of Ge islands[30]. In this case, the shape and size are also significantly modified by the presence of Sb on surface. Non- faceted Sb-mediated Ge islands are observed, their size is significantly reduced with higher island density and the bimodal size distribution is remarkably suppressed, see Figure 1.16.

1.4.3 Symmetry-breaking of elasticity on vicinal substrate

Since the elasticity plays the major role in terms of kinetic pathway and thermodynamic formation of islands on Si nominal (001) substrate, slight changes of elasticity would dramatically modify the island formation. SiGe epitaxy on vicinal substrates with different miscut angles is proposed as a promising method toward controllable self-organization of islands, in which the symmetry-breaking of elasticity is the main playing factor. On a vicinal (001) substrate, miscut angles toward [011] direction presents a strain of parallel atomic steps along [110] direction. Stabilized by strain, facet (105) is still bounding the islands with asymmetrical shape, see Figure 1.17. Berbezier et al. and Persichetti et al. investigated the Ge island formation mechanisms on substrate with various miscut angles(0°, 1.5°, 2°, 4°). They demonstrated the stabilizing effect of (105) faceting in the island formation combined with energetic calculation[31].

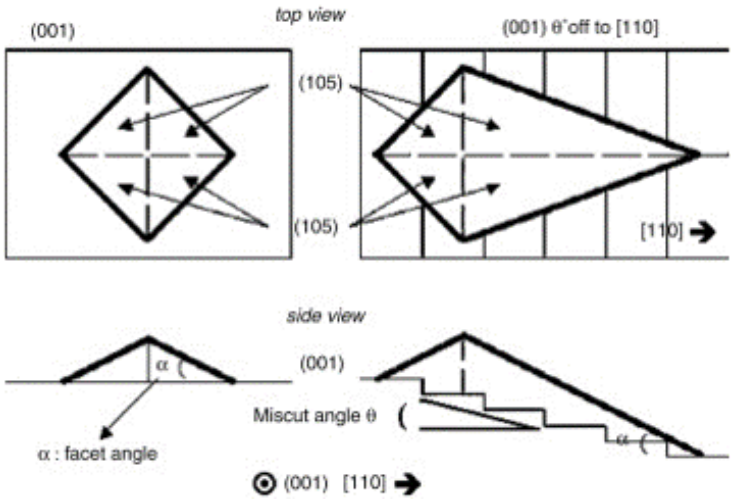

Figure 1.17: Schematic of islands lying a vicinal surface[14]

While the composition x of $Si_{1-x}Ge_x$ decreased, the formation pathway also switches from stochastic nucleation to gradual and continuous pathway of ATG instability similar as on nominal (001) substrate. When a 10 nm $Si_{0.7}Ge_{0.3}$ thin layer is deposited on Si (001) 10° off substrate at 550 °C , the as-grown sample shows non-faceted 1D ripples perpendicular to the step edges resulting from the asymmetry of substrate, seeFigure 1.19. During post-growth annealing, the ripples begin to evolve with the onset of (113) facets. Later on the ripples break into triangular islands elongated along miscut direction, Figure 1.19b, [32].

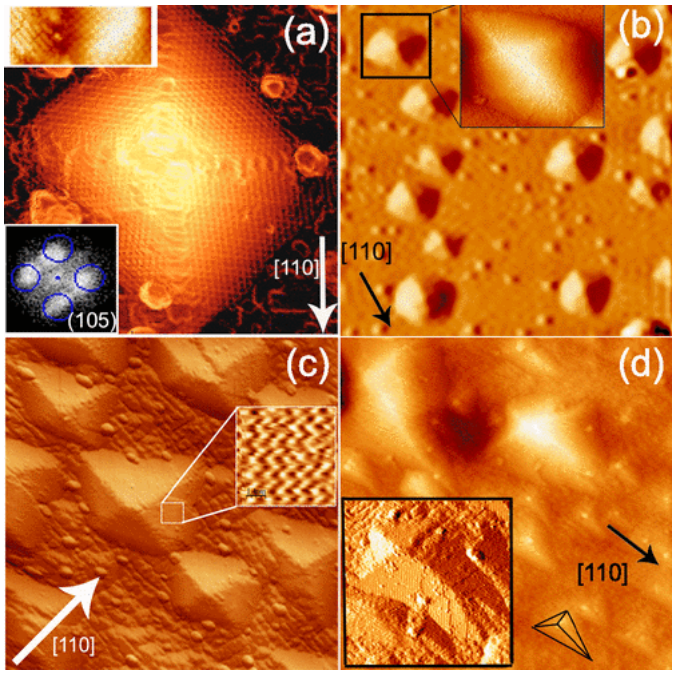

Figure 1.18: AFM image of 13ML on (a) Si(001) and (b) with 1/2ML Sb on Si(001)[31]

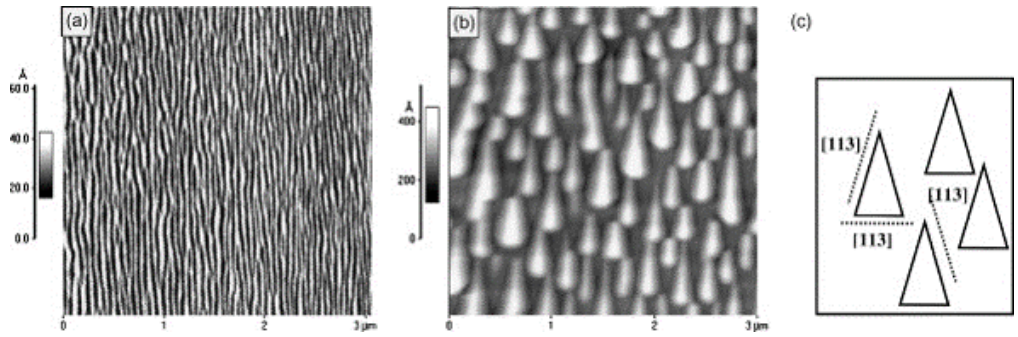

Figure 1.19: AFM image ($3 \times 3\ \mu m^2$) of $Si_{0.7}Ge_{0.3}$ islands obtained for a deposited thickness of 10 nm: (a) as-grown; (b) 18 h anneal; (c) is a schematic representation of (113) facets on the annealed sample.[32]

The influence of miscut angle toward [010] direction was also systematically studied by T. Zhou et al.[33]. In this study, the (105)-faceted islands elongate along the step edges resulting from the misorientation angle. They align [010] direction and form well-aligned planar 2D nanowires, see Figure 1.20b and c.

On the vicinal substrates, it is suggested that the step bunching is hindered. Until now it is still unclear how the large density of parallel steps on vicinal substrates can control the shape of the islands. It it an effect of elasticity or surface diffusion.? We will especially investigate this issue both from experimental and theoretic point of view in Chapter 4.

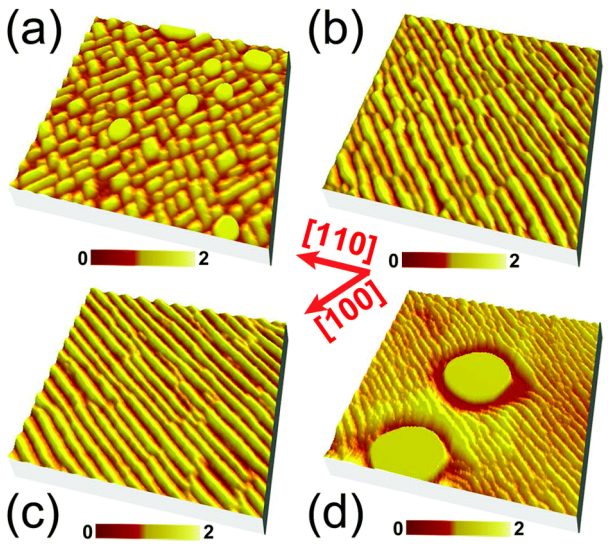

Figure 1.20: AFM images ($0.5 \times 0.5 \mu m^2$) of the surface morphologies: (a) 6 ML Ge deposition at 540 °C on Si (001)/[100] 0°; (b) 5.4 ML Ge deposition at 540 °C on Si (001)/[100] 7°; (c) 5.4 ML Ge deposition at 540 °C with a subsequent in-situ annealing for two hours on Si (001)/[100] 7°; (d) 5.4 ML Ge deposition at 650 °C on Si (001)/[100] 7°. The unit of color bar is nm.[33]

1.4.4 Pre-designed stressors

Another fascinating method to control the self-organization of SiGe QDs is to create some pre-designed stressors prior to their growth. Such modification is expected to create strain gradients in the substrate and should b a reliable way to control the formation kinetics and thermodynamics. J. Tersoff et al. firstly demonstrated that the self-organization of quantum dots would be tuned by the quantum dots buried beneath while fabricating stacking quantum dots superlattices[34]. The successive layers of quantum dots vertically self-align on each other. As the stacking inctrease, the network of QDs gradually become more uniform in size and spacing. It was claimed for instance that for $Si_{0.25}Ge_{0.75}$ after a dozen of layer stacking (20 layers shown in the article), the size distribution narrows and ordering increases compared with the first-layer spontaneous quantum dots. V. A. Zinovyev et al. used SiGe quantum dots as buried stressor to arrange the successive stacking quantum dots and fabricate quantum dot molecules[35]. The favorable nucleation sites of successive quantum dots are tailored by the buried stressor. For a strained surface , the chemical potential can be written as[35]

$$\mu = \mu_0 + \Omega\gamma k + \Omega E_s \tag{1.12}$$

where μ_0 is the chemical potential of flat unstrained surface γ is the free surface energy of the wetting layer per unit area, Ω is the atomic volume, k is the local surface curvature and E_s is the local strain energy at the surface. The effect of buried stressor mainly traced to the third term ΩE_s. FEM(Finite Element Method) was employed to determine the strain-dependent chemical potential E_s on the surface of the buried

stressor (truncated pyramid here). It is found that the nucleation sites of the stacking QDs are aligned on the buried stressor, corresponding to the sites with lowest chemical potential sites, see Figure 1.21.

Interestingly, the interaction between quantum dots through the stressor also shows fascinating results for the quantum dots on SiGe nanowires[36] and on thin Si membrane as substrate[37].

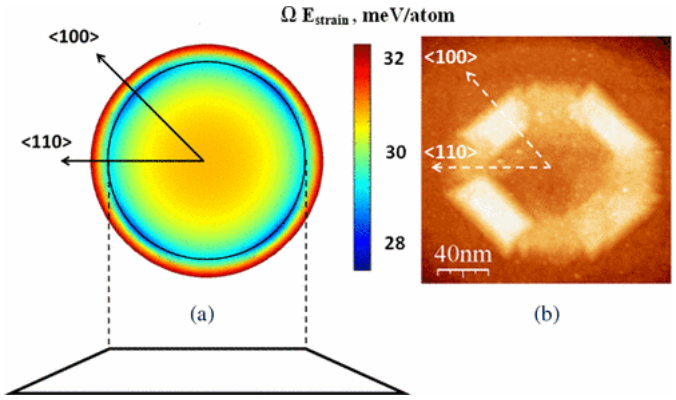

Figure 1.21: (a) Simulation by FEM of the surface distribution of strain-dependent chemical potential on the top of a SiGe disklike nanomound covered by a thin Ge wetting layer. The disklike nanomound was represented by a truncated cone with a height to base aspect ratio of 0.05 and a sidewall inclination angle of 14 deg. (b) STM image of spatial ordering of small 3D islands nucleated on the disklike nanomound after deposition of 3.5 MLs of Ge at 600 °C . [35]

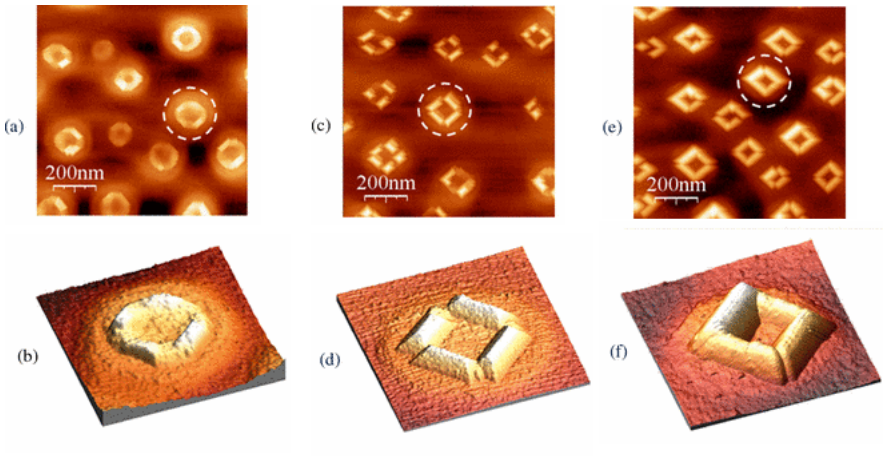

Figure 1.22: STM images ($1 \times 1 \mu m^2$) of the groups of closely spaced SiGe islands grown at 660 °C on a three-layered QD superlattice template with different thickness of deposited Ge:(a) 3.5 MLs, (c) 4 MLs, (e) 5 MLs. Image sides are oriented along the [011] directions. Figures (b), (d), and (f) correspond to three-dimensional representations of the fourfold symmetric QDMs, marked by dash circles in (a), (c), and (e), respectively[35].

1.4.5 Pre-patterning on substrate

Since the formation of QDs is very sensitive to the local chemical potential on the substrate, a geometrical designing of the substrate by pre-patterning a priori changes the capillarity and elasticity simultaneously and then opens an efficient way to organize the QDs. Furthermore, the ultra-high resolution processing techniques including photo-lithography, E-beam lithography and FIB (Focused Ion Beam) permit finer and more effective design and fabrication of patterns on substrate. The patterns create the preferential sites of island formation and thence offer the possibility to fabricate ordered islands with uniform composition.

Micrometer-scale patterns are fabricated by conventional photo lithography as nucleation centers for formation of Ge islands via epitaxy[38]. The islands are found to reside preferably at the concave and/or the convex region that correspond to the local minimum chemical potential depending on the shape of patterns. In order to elucidate the influence of pattern on the chemical potential, the contributions of surface energy and elastic energy are considered in Equation 1.12. The difference is that the second $\Omega\gamma k$ and third term ΩE_s are both a function of pattern geometry. In principle, atoms γk favors the concave position in terms of capillarity while it favors the convex position in terms of elasticity E_s. As a result of competition between γk and E_s, the chemical potential along a bumpy pattern is calculated and plotted in Figure. 1.23b.

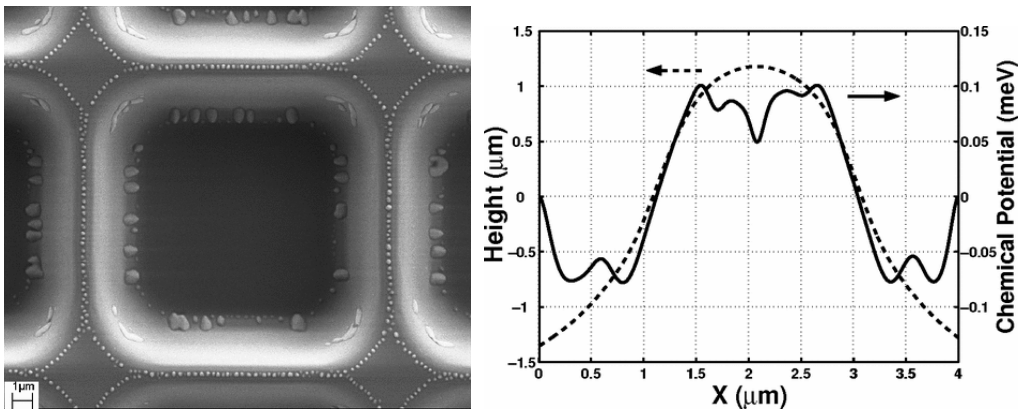

(a) **(b)**

Figure 1.23: (a)Scanning electron microscope image of Ge 3D islands ordered on patterned stripes on Si (001) with $Ge = 60\ MLs$. The stripes are oriented in ⟨110⟩ directions, but ordering of Ge QDs is independent of this direction. (b) variation of the local surface chemical potential of stripe structures with position X (solid line). The dashed line is the surface profile measured by AFM[38].

A more systematic kinetic model is proposed by Hu et al.[39] to elucidate strained islands formation on patterns . The surface energy anisotropy as well as elasticity are found to determine the preferential sites of island nucleation. The model considers the nucleation of islands on a sawtooth pattern with a constant slope of angle φ as

shown in Figure 1.24. Coherent island lies on the pattern with contact angle θ. The strain energy difference between the island and flat strained film can be calculated using Green's function method with small-slope approximation[39]:

$$E_e = -\frac{\sigma^2}{2}\iint dx\,dx'\chi(x-x')\partial_i t(x)\partial_i t(x') \tag{1.13}$$

where σ is the stress in the island, x and x' denote the position along the surface, χ is the Green's function and $t(x)$ is the epilayer thickness function. By solving Equation 1.13, the elastic energy change is simply:

$$E_e = \varepsilon_0 S(\tan\theta - \tan\varphi) \tag{1.14}$$

where $\varepsilon_0 = (2\ln 2)\sigma^2(1-\nu^2)/\pi Y$ is the strain energy of flat reference strained film, ν is Poisson ratio and Y is Young's modulus and $S = l^2(\tan\theta - \tan\varphi)$ is the island base area. While the surface energy of wetting layer and island facets are set as constant γ_w andγ_f, the excess surface energy created by island formation is:

$$E_s = 2l(\gamma_f \sec\theta - \gamma_w \sec\varphi) \tag{1.15}$$

The surface energy anisotropy is represented using a generic form of $\gamma_w = \gamma_0(1-\alpha\cos(n\phi))$ while the island facet is the first low-energy facet beyond flat surface, one can define $\theta = 2\pi/n$ then $\gamma_f = \gamma_0(1-\alpha)$. Here parameter α is introduced to describe the surface energy anisotropy. n is set as 32 to represent the (105) facet of island. Thence one can calculate the formation energy of island as:

$$E = E_e + E_s \tag{1.16}$$

and the competition between E_e and E_s produces the critical island size S_c and nucleation energy barrier Ec. The influence of pattern on the nucleation kinetics can be denoted as S_c and E_c, the critical volume and energy barrier of nucleation. They are the function of pattern shape parameter φ, surface energy anisotropy parameter α, which is plotted in Figure 1.25.

Nanometer-scale patterning became recently possible with the development of E-beam lithography and FIB. Chen.G et al. used E-beam lithography and subsequent reactive ion etching(RIE) to make patterns with large periodicity and aspect ratio. A thick buffer layer of more than 100 nm is deposited to cap the impurities and produce a clean starting surface while preserving the patterns. Ge domes with the same ordering of patterns can be fabricated as in Figure 1.26. FIB patterning is convenient technique to fabricate adjustable patterns with tunable characteristics such as hole size, pitch distance etc. with a precision of dozens of nanometers. During patterning process the ions would locally implant in the substrate. They can either be further removed by post-patterning treatment[40] or act in the substrate as surface surfactants whose dose and distribution are controllable [41]. In Figure 1.27, the Ge islands are obtained

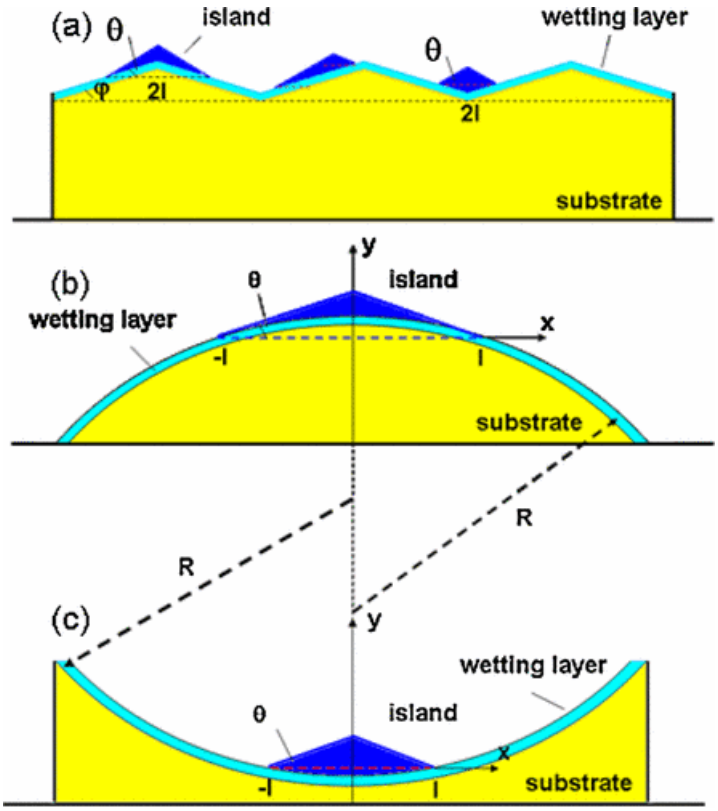

Figure 1.24: Schematic illustration of island nucleation on patterned substrates. (a) On a saw-tooth pattern; (b) on the apex of a concave surface; (c) in the valley of a convex surface.[39]

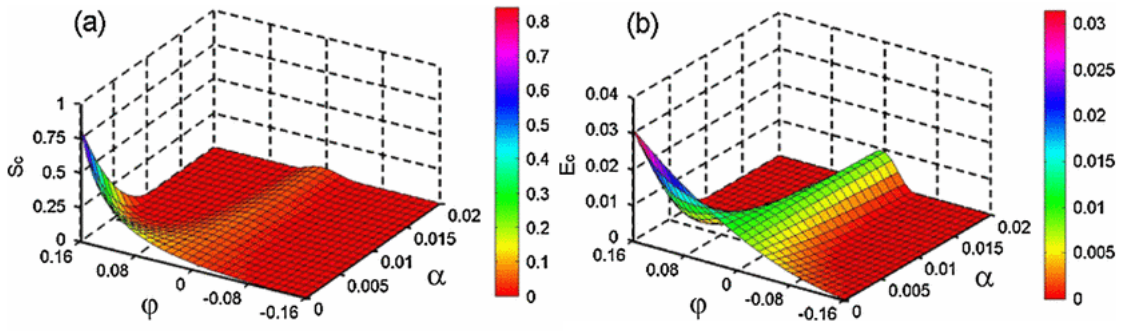

Figure 1.25: Critical size of Island nucleation (a) and energy barrier (b) as a function of α and φ . The size is in unit of $\gamma_0^2/\varepsilon_0^2$ and barrier in unit of γ_0^2/ε_0[39]

through the deposition of Ge on FIB-patterned substrate in which the implanted Ga ions are removed prior to Ge deposition via a two-step cleaning process: Annealing and subsequent HCl bath [40]. Interestingly, the nucleation sites of islands are found to be dependent upon deposition temperature. At high temperature ($T_S = 750\,°C$), the dots reside on the terraces between holes, and at low temperature ($T_S = 550\,°C$) the dots tend to nucleate in the holes, whose transient temperature is then found around ($T_S = 650\,°C$) at which some dots locate in holes and some on terraces. Kinetic Monte Carlo simulation then revealed that favourable island position is dominated by the competition between kinetic diffusion and kinetic nucleation energy. At low temper-

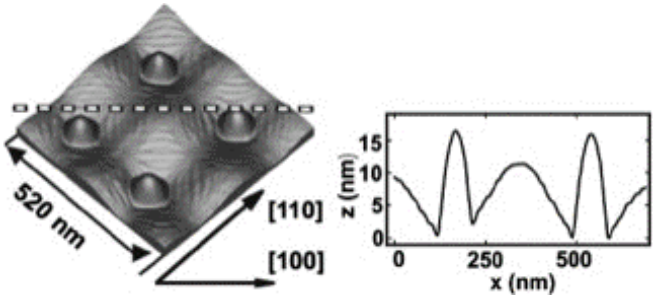

Figure 1.26: (Left)AFM image of the prepatterned Si substrate with 5 ML of Ge. (Right) Line scan in [100] direction along the dashed line in (a).

ature the diffusion of deposited Ge atoms across the hole-wall steps is blocked due to the lack of thermal kinetic energy. Ge atoms are kinetically trapped in the holes. At high temperature, the system can more easily overcome the kinetic energy barrier and reach an equilibrium state[40].

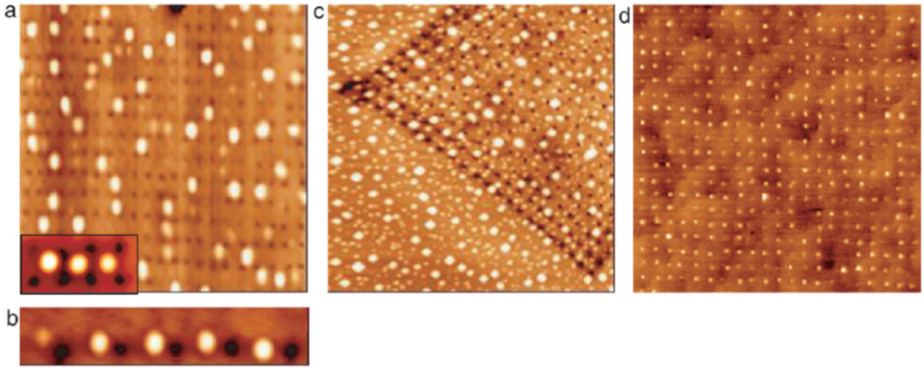

Figure 1.27: AFM images (scan size 1.5μm) of FIB patterned areas after 8 ML Ge deposition at different temperatures (T_S): (a) T_S = 750 °C In this situation the size of QD (100 nm) is in the range of the hole-hole distance (180 nm). The inset shows a higher magnification image of three Ge QD situated on the terraces between the FIB pits; (b) T_S = 750 °C . When the pitch is larger, the size of the QDs is three times smaller than the hole-hole distance (350 nm). Ge QDs are located close to FIB pits; (c) T_S = 650 °C , hole-hole distance is 180 nm. At this temperature the Ge QDs are located randomly both in the holes and out of the holes; (d)T_S = 550 °C ., Ge QDs are located only in the holes due to the diffusion barrier.[40]

Substrate pre-patterning has become a widely used process to fabricate controllable semiconductor quantum dots[42][43]. One step forward, it has been shown that it is viable to fabricate 3D SiGe quantum dot crystals by combining the two mentioned mechanisms: pre-patterning and pre-designed stressor[44]. 2D periodic hole arrays are firstly fabricated via extreme ultraviolet interference lithography(EUV-IL), ordering Ge quantum dot array can be fabricated via epitaxy of Ge in MBE after the pattern transfer to Si substrate and substrate cleaning [44]. A thin layer of Si is deposited on quantum dot array at lower temperature to suppress the intermixing, and afterwards quantum dots would be self-aligned in the vertical direction when Ge is deposited

on Si layer thanks to the mechanism explained in Section 1.4.4. This process is self-repeatable and 3D quantum dot crystal can be finally produced as shown in Figure 1.28 which demonstrates fascinating opto-electronic properties[44].

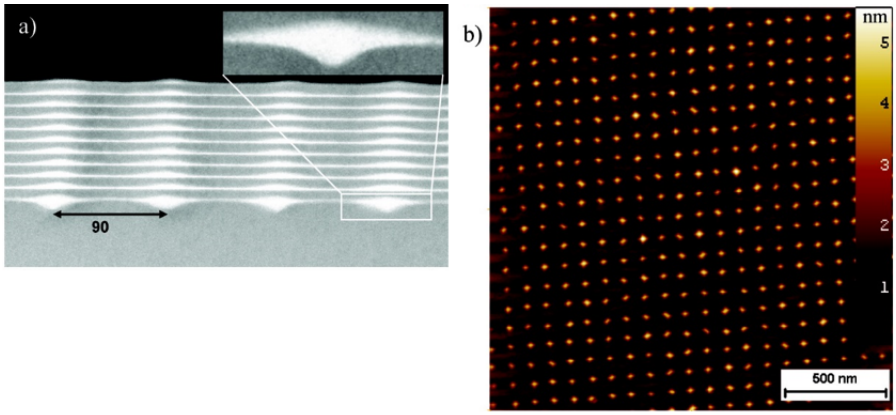

Figure 1.28: (a) TEM cross-section image of 10 period stacks of Ge islands and Si spacer layer (10 nm) deposited on a pre- patterned area, (b) AFM images of the surface of the same sample. The inset in (a) shows a closeup of a dot in the first layer. The comparison of the cross-sectional TEM micrographs and the AFM images demonstrates that the vertical and the lateral ordering is maintained after 10 periods on the pre-patterned substrate. [44]

In the regime of ATG instability growth mode, the evolution of SiGe epilayer on patterns is simulated via a continuum elasticity model in the works by X. Xu et al.[45][46][47]. Similarly the formation of islands is tailored by the capillarity and elasticity while in this case the patterns are characterized by the wavelength which can be conveniently associated to the ATG instability wavelength λ_{ATG}. Free epilayer $h(x,y,t)$ deposited on patterned substrate with pattern function $z=\eta(x,y)$ evolves with annealing time t, see Figure 1.29(a). Tuned by the capillarity and elasticity, islands form finally with different orderings and density, totally dependent on epilayer thickness $\bar{H}/H_c$ and pattern wavelength λ_η with respect to λ_{ATG}, which is written as:$\lambda_\eta/\lambda_{ATG}$[47],. The different situations were clearly summarized in a diagram in Figure 1.29(e).

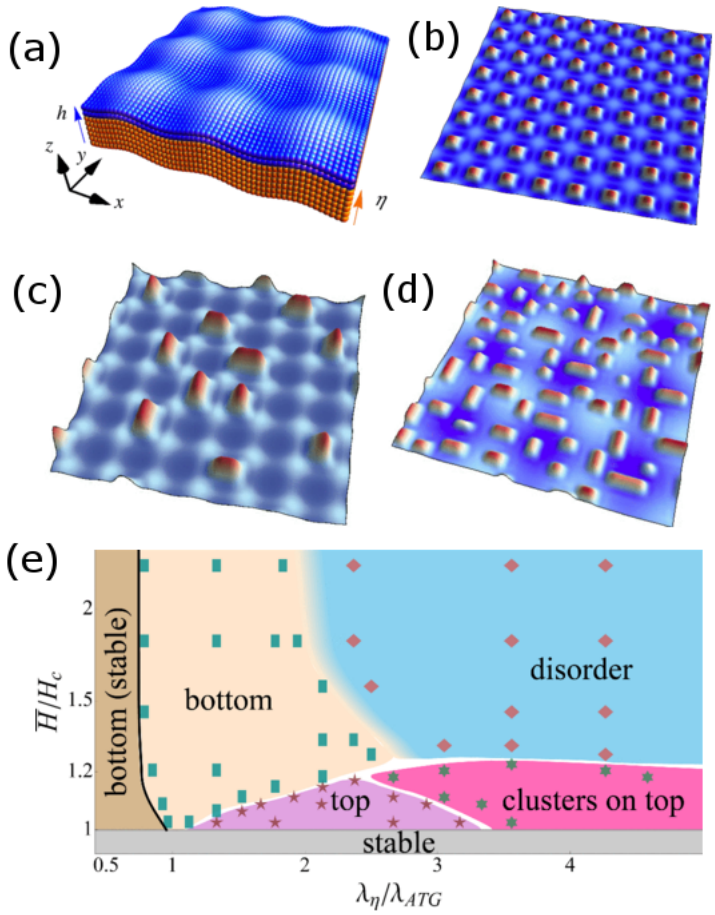

Figure 1.29: (a), Schematic figure of epilayer deposited on patterned substrate $z = \eta(x, y)$; (b), highly-ordered islands locate in the valleys of pattern in case of $\bar{H}/H_c = 1.8$ and $\lambda_\eta/\lambda_{ATG} = 1$; (c), islands undergo coarsening with less ordering in case of $\bar{H}/H_c = 1.3$ and $\lambda_\eta/\lambda_{ATG} = 1$; (d), disordered islands with $\bar{H}/H_c = 1.8$ and $\lambda_\eta/\lambda_{ATG} = 6$; (e), the phase diagram to summarize the island ordering as a function of $\bar{H}/H_c$ and $\lambda_\eta/\lambda_{ATG}$.[47]

1.5 Summary

As a summary of this chapter, we gave out a brief introduction to the epitaxial growth of semiconductors and highlighted the importance of Si Ge epitaxy. Furthermore, the fabrication of SiGe quantum dots via SiGe epitaxy is reviewed in details from the experiments to modeling. Several methods and studies dedicated to controllable growth of SiGe quantum dots have been briefly summarized to give a comprehensive background necessary to understand the major issues that have been addressed in this thesis.

Chapter 2

Growth pathways: from Nucleation to ATG Instability

Contents

In this chapter, we propose a thermodynamic model to investigate the nucleation of $Si_{1-x}Ge_x$ islands on Si(001) substrate and to particularly study the influence of composition x to the nucleation kinetics. Combining with Classic Nucleation Theory, we quantitatively elucidate the transition of growth mode from nucleation in high strain regime to nucleationless in low strain regime and estimate the critical composition x_c via comparing nucleation time scale and characteristic time of ATG instability. The main results are evidenced in experiments aiming at highlighting growth mode via observing the very onset of 3D evolution.

2.1 Background

As shown in Chapter.1, depending on the amount of strain, the 3D evolution of $Si_{1-x}Ge_x$ epilayer behaves as two different modes: nucleation/ATG instability at high/ low strain regime. Previously these two growth modes have been studied separately. Their formation mechanisms are described by different theories. The island formation at high-strain regime is described by the classical nucleation theory while continuous morphological undulation via surface diffusion, driven by elasticity, is believed to govern the low-strain regime. However, a quantitative description to these two evolution modes is still in demand and the transition of evolution modes still remains as an issue of confusion and controversy.

In Figure 2.1 we demonstrate two clear examples of strained thin films: the long-range order is clear for $Si_{0.7}Ge_{0.3}$ layer in (a) and discrete islands formed on the surface for the Ge layer in (b). On the top are schematic figures and planview TEM images at the bottom. The cross-over composition x_c, refers to the critical composition separating these two growth pathways.

2.2 Energetics of island nucleation

In order to investigate the energetics of island formation, we consider a square-base pyramidal island with (105) facets that emerge from a flat strained film, shown in Figure 2.2. The (105)-faceted pyramid is ubiquitously found in experiments on SiGe and disclosed to be a partially stabilized state. First-principle calculations furthermore revealed that the (105) facet is stabilized by the epitaxial strain [23][48]. For simplicity, in this model the pyramid is taken as the nucleation island directly without missing the generality [23][48], see below for a discussion for pre-pyramid.

In Figure 2.2, a strained flat epilayer with thickness h_0 is taken as the reference state. The energy variation between this reference state and a pyramid can be decomposed as:

$$\Delta E = \Delta E^{surf} + \Delta E^{ed} + \Delta E^{el} \tag{2.1}$$

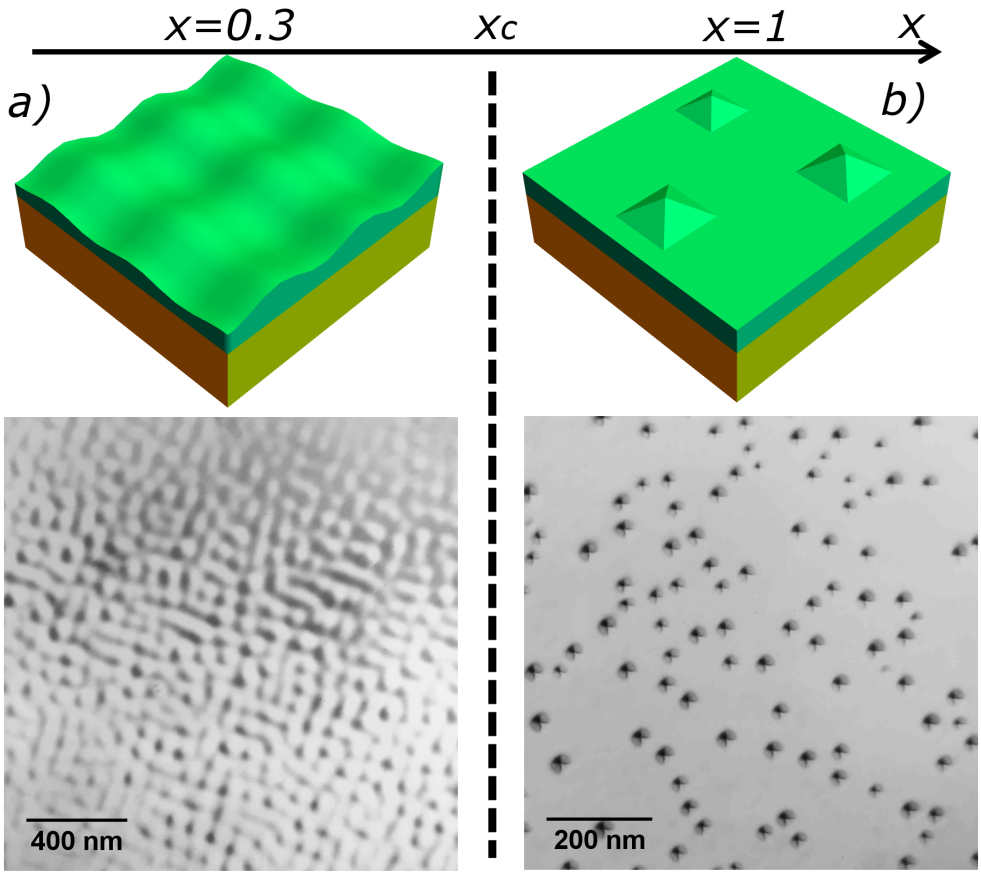

Figure 2.1: Growth pathways of $Si_{1-x}Ge_x$ strained layers depending on x: (a), schematic figure of ATG instability and plan-view TEM image of $Si_{0.7}Ge_{0.3}$ layer ; (b), schematic figure of nucleation and plan-view TEM image of Ge layer.

where ΔE^{surf}, ΔE^{ed}, ΔE^{el} are respectively the variation of surface energy, edge energy and elastic energy.

2.2.1 Capillarity

Due to the wetting effect, surface energy is a function of the epilayer thickness [48]. The quantitative relation between surface energy and thickness was firstly proposed by Lu. et al.[48] to be exponential while for a Ge epilayer on Si(001), the exponential decay $\gamma_0 + \gamma_w e^{-h/\delta_0}$ was shown to be consistent with first-principle calculations [49][28]. Mass conservation enforces the balance $h_w = h_0 - \rho V/a$ in Figure 2.2.

On the other hand, the surface energy of $Si_{1-x}Ge_x$ also depends upon the composition x. The real composition of $Si_{1-x}Ge_x$ epilayer has been an issue of controversy , the complexity of which is increased owing to mechanisms of surface segregation of Ge and SiGe intermixing. Here for simplicity, we consider an epilayer surface which is fully enriched Ge as evidenced by experiments[50] so that the surface energy of $Si_{1-x}Ge_x$ is simplified to be independent of x. (At the end of this chapter, we will demonstrate that this simplification does not change our main results). Considering surface energy

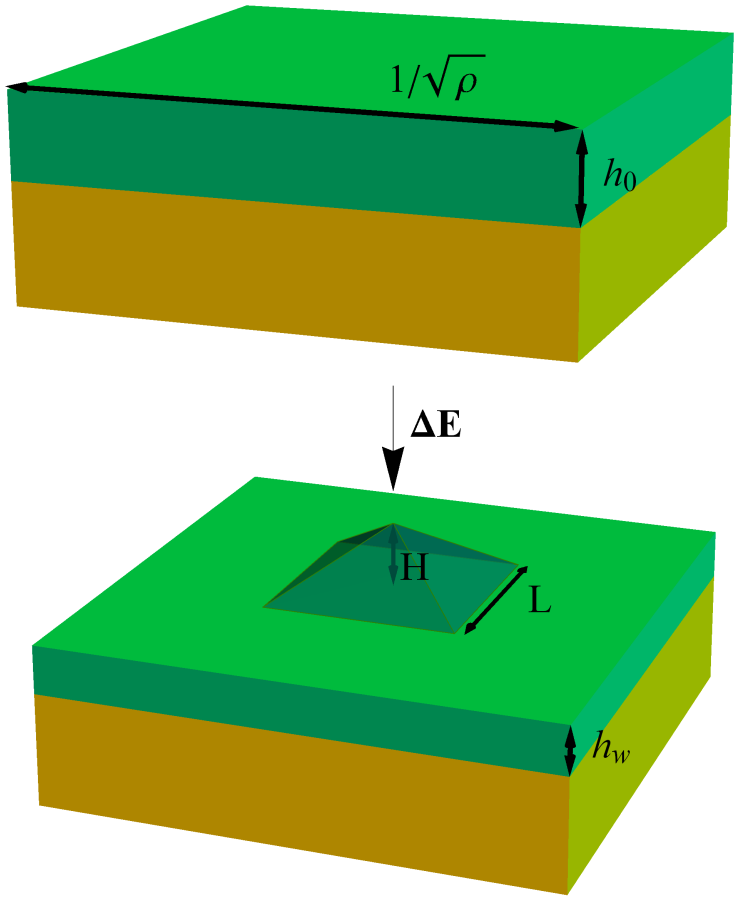

Figure 2.2: A pyramidal island emerges from a flat strained film

anisotropy, the surface energy variation ΔE^{surf} can be written as:

$$\Delta E^{surf} = \frac{\gamma_{Ge}^{105} L^2}{\cos\theta} - \gamma_{Ge}^{001} L^2 \quad \textbf{(2.2)}$$

$$= \gamma_{Ge}^{001} \eta L^2 \quad \textbf{(2.3)}$$

where η describes the anisotropy:

$$\eta = \frac{\gamma_{Ge}^{105}}{\gamma_{Ge}^{001}} \frac{1}{\cos\theta} - 1 \quad \textbf{(2.4)}$$

where L is the base length of the pyramid and θ is the contact angle with $\tan\theta = 0.2$ corresponding to (105) facet on (001) substrate. Thence the volume of pyramidal island is $V = L^3/6\tan\theta$.

It costs some energy to create the facet edges including (001)-(105) edges and (105)-(105) edges. On average, the edge energy is taken as proportional to the total edge length and the edge energy density σ^{ed} is estimated via atomic calculations to be 10 $meV/$Å. According to works dedicated to the calculation of the edge energy of Ge pyramid[51][52][53], we choose its magnitude of 10 $meV/$Å which leads to a reasonable nucleation energy

barrier. 270/3 $meV\text{Å}^2$ is another value found to fit experimental results. It results in enormous energy barrier in the following calculations, which is consequently discarded. At the end, the edge energy ΔE^{ed} is:

$$\Delta E^{ed} = \frac{4H}{\tan\theta}(2+2\sqrt{2+\tan^2\theta})\sigma^{ed} \tag{2.5}$$

where H is the height of pyramid, $V = \frac{4H^3}{3}\tan^2\theta$.

2.2.2 Elasticity

Elastic interactions may be computed within the small-slope approximations, described in the Appendix A. The driving force for island formation is the elastic relaxation. Here we focus on the elastic relaxation of a pyramid compared to a flat epilayer. Within the small-slope approximation, a given epilayer $h(\boldsymbol{r})$ with a free surface on a semi-infinite substrate, the elastic energy E^{el} is[49]:

$$E^{el} = \varepsilon_0 \int d\boldsymbol{r}\left\{h(\boldsymbol{r}) - \zeta h(\boldsymbol{r})\mathscr{H}_{ii}[h(\boldsymbol{r})]\right\} \tag{2.6}$$

where $\varepsilon_0 = \frac{Y_f\delta^2}{1-\nu^f}$ is the elastic energy density, computable via small-slope approximation, see Appendix A, $\zeta = Y_f(1-\nu_s^2)/Y_s(1-\nu_f)$ with Y_f, Y_s referring to Young's modulus of film and substrate, ν_f,ν_f referring to their Poisson's ratios (as regards elastic constants of Si and Ge, see Appendix D) and $\mathscr{H}$ denotes the Hilbert operator given as:

$$\mathscr{H}_{ij} = \mathscr{F}^{-1}[(k_i k_j/|\boldsymbol{k}|)\hat{h}(\boldsymbol{k})] \tag{2.7}$$

with $\mathscr{F}^{-1}$ denoting the Inverse Fourier Transform (IFT)[49].

The first term $\varepsilon_0\int d\boldsymbol{r}\,h(\boldsymbol{r})$ is the elastic energy of flat film with the same volume of materials and the second term

$$\Delta E^{el} = \varepsilon_0 \int d\boldsymbol{r}\left\{-\zeta h(\boldsymbol{r})\mathscr{H}_{ii}[h(\boldsymbol{r})]\right\} \tag{2.8}$$

represents the elastic relaxation enforced by the surface undulation. By numerical calculation, we compute $\Delta E^{el}(V)$ and indeed find a linear dependence with the volume V:

$$\Delta E^{el} = -\zeta p\varepsilon_0 V \tag{2.9}$$

with the coefficient $p \simeq 0.198$. The elastic relaxation of coherent pyramid island was also calculated thanks to Green's function as[54].

$$p = 4(\sqrt{2}-1)[1+\ln(1+\sqrt{2})]\tan\theta/\pi \tag{2.10}$$

which turns to be around 0.198 when $\tan\theta = 0.2$ corresponding to (105)-faceted pyramid.

2.2.3 Nucleation Energy Barrier

When h_0 is small, the wetting effect enforces that the materials spread on the substrate and island formation is energetically hindered; when h_0 is larger than a critical value h_c, nucleation may occur since the wetting effect decreases exponentially. As a result, for a given composition x, one can estimate the corresponding $h_c(x)$ if we simply consider a criterion that the formation energy decreases for large enough volume. We take $x = 1$ as example and plot ΔE as a function of the volume V while varying the wetting layer thickness h, see 2.3 ΔE diverges while increasing V if $h_0 < h_c$; in case of $h_0 > h_c$ ΔE overcomes energy barrier and begins to decrease with V. The calculation of the wetting layer thickness is of great significance as well, and we will investigate it below.

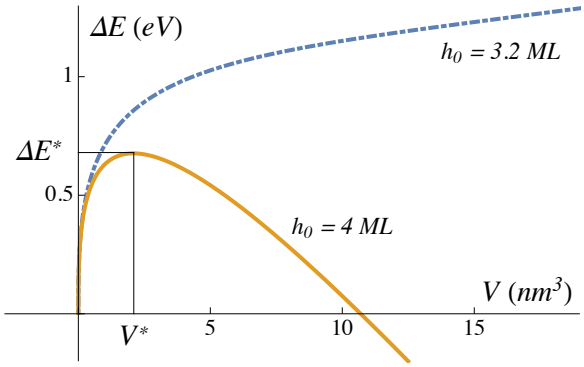

Figure 2.3: Formation energy ΔE as a function of volume V while varying h_0 fixing $x = 1$.

In order to simplify the issue and disclose the main effect of composition x, here we consider in the following a thick enough wetting layer to eliminate the wetting effect.

With Equation 2.3, 2.5 and 2.9, we finally write the island formation energy ΔE as a function of volume V:

$$\Delta E = \tilde{\sigma} V^{1/3} + \tilde{\gamma} V^{2/3} - \tilde{p} V. \tag{2.11}$$

with

$$\tilde{\sigma} = 46^{1/3}(1+\sqrt{2+\tan^2\theta})\tan^{5/3}\theta\sigma^{ed}$$
$$\tilde{\gamma} = (6\tan\theta)^{2/3}\gamma_{Ge}^{001}\eta$$
$$\tilde{p} = \xi p\epsilon_0$$

One can then find the maximum value, which is the nucleation energy barrier:

$$\Delta E^* = \frac{1}{27\tilde{p}^2}[\tilde{\gamma}(2\tilde{\gamma}+9\tilde{p}\tilde{\sigma}) + 2(\tilde{\gamma}^2+\tilde{p}\tilde{\sigma})^{3/2}] \tag{2.12}$$

and critical volume

$$V^* = \left[\frac{\tilde{\gamma}+\sqrt{\tilde{\gamma}^2+3\tilde{\sigma}\tilde{p}^2}}{3\tilde{p}}\right]^{1/3} \tag{2.13}$$

as typically shown in Figure 1.7.

2.3 Master equation of nucleation: Nucleation Time Scale

2.3.1 master equation

In the classic nucleation theory (CNT), the stationary nucleation rate J is related to the nucleation energy barrier $\Delta E*$. Here we try to estimate a typical nucleation time scale τ in order to evaluate its competition with the ATG instability time scale.

The concentration of nuclei C_n consisting of n atoms (n-mer) is ruled by the Maxwell-Boltzmann distribution as:

$$C_n = C_1 e^{-\Delta E_n / k_B T} \tag{2.14}$$

where C_1 and C_n are respectively the density of monomers and n-mers on the surface.

The evolution of C_n is described by the master equation[55]

$$\frac{\partial C_n}{\partial t} = \sum_m [f_{m,n} C_m - f_{n,m} C_n] \tag{2.15}$$

where $f_{m,n}C_m$ stands for the transition frequencies that m-mers transit to n- mers. The equation can be conveniently represented as Figure 2.4, in which $\sum_m f_{m,n}C_m$ and $\sum_m f_{n,m}C_n$ are respectively the inward flux and outward flux for the density of n-mers.

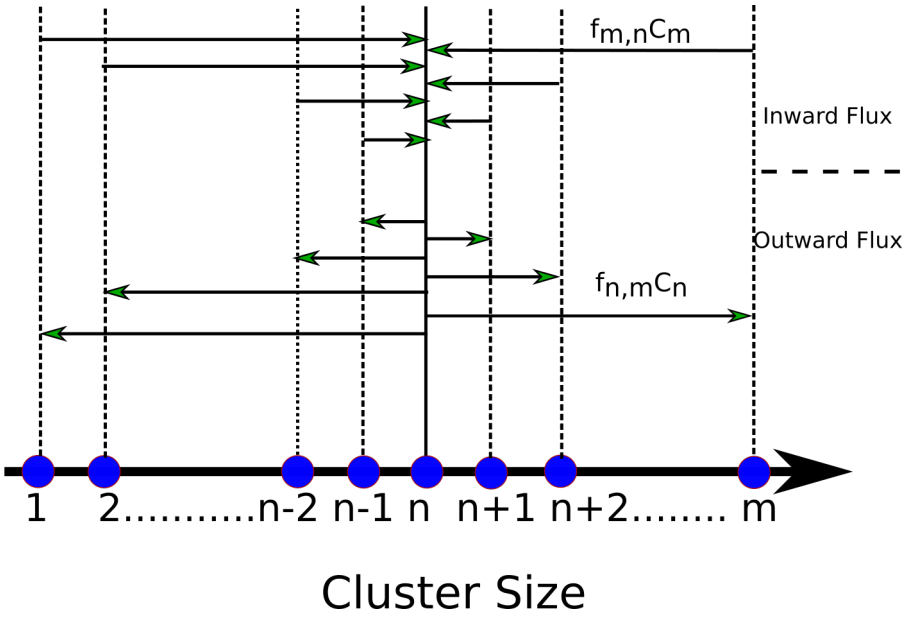

Figure 2.4: Schematic presentation of the possible changes in the size of a cluster of n molecules. The concentration of n-sized clusters diminishes because of $n \rightarrow m$ transitions (the arrows leaving size n) and increases thanks to $m \rightarrow n$ transitions (the arrows ending at the size n).

In practice, the attachment/detachment proceed mainly via the transfer of monomers so that the master equation Equation 2.15 turns to:

$$\frac{\partial C_n}{\partial t} = f_n C_n - g_n C_n \tag{2.16}$$

in which $f_n = f_{n-1,n}$ and $g_n = f_{n,n-1}$ are actually the monomer attachment and detachment frequency respectively. The CNT exhibits a stationary regime where nucleation occurs with a rate[55, 56]

$$J^{st} = Z f_{n^*} C_{n^*} \tag{2.17}$$

where Z is called the Zeldovich factor, f_{n^*} is growth frequency of cluster of critical size n^* and C_{n^*} is the density of cluster with a critical size given by Equation 2.14. Z is found to be :

$$Z = \beta/\pi^{1/2} = [(-\partial^2 \Delta E/\partial n^2)_{n=n^*}/2\pi k_B T]^{1/2} \tag{2.18}$$

where $\beta = (-\partial^2 \Delta E/\partial n^2)_{n=n^*}/2k_B T$, the curvature of the $\Delta E(n)$ curve at $n = n^*$. Combining with Equation 2.11, we get:

$$Z = \frac{2a^3\sqrt{k_B T}}{\tan\theta\sqrt{\pi\tilde{\sigma}^2}}(\tilde{\gamma} - \sqrt{\tilde{\gamma}^2 + 3\tilde{\sigma}\tilde{p}})(\tilde{\gamma}^2 + 3\tilde{\sigma}\tilde{p})^{1/4} \tag{2.19}$$

Growth frequency f_{n^*} is the last factor to be estimated.

2.3.2 Growth frequency in surface diffusion process

As regards the epitaxial growth of semiconductors, only the attachment and detachment of monomers is supposed to be important in atomic process. By introducing the capture number, the attachment frequency f_n may be approximately estimated as[55]

$$f_n = r_n \alpha D_s C_1 \tag{2.20}$$

where r_n is sticking/attachment coefficient, roughly varying from 0 to 1, α is the capture number between 1 and 5; C_1 is the monomer/adatom concentration on the surface, given by $\frac{1}{a^2} e^{-E_1/k_B T}$ knowing the attachment energy $E_1 \simeq 0.3eV$ for Si and D_s is surface diffusion coefficient which is calculated as $D_s = a^2 \nu_0 e^{-E_{diff}/k_B T}$ in which $E_{diff} \simeq 0.83eV$ [57] on Si surface, a is the lattice constant, ν_0 is atomic vibration frequency in magnitude of $\nu_0 \simeq 10^{13} s^{-1}$.

Note that even though quite a few parameters are necessary to quantitatively describe the nucleation kinetics as shown above, at the end, our main results are insensitive to these parameters. The main goal here is to give out the reasonable parameters, paving the way to further analysis. In addition, detachment is supposed to be negligible or can be treated as being equivalent to a modification coefficient.

2.3.3 Nucleation time scale

With stationary flux equation Equation 2.17, one can estimate the typical time $\boldsymbol{\tau}^{nuc}$ required to find one nucleation event on a surface of a typical area $(1/\rho)$, which is taken as the typical island surface with the island density $\rho = 10^{13} m^{-2}$ as:

$$\boldsymbol{\tau}^{nuc} = \frac{1}{J^{st} S^{nuc}} = \frac{\rho}{J^{st}} = \frac{\rho}{Z f_{n^*} C_{n^*}} \tag{2.21}$$

A brief qualitative analysis is given here. For a given temperature T, ρ and f_{n^*} are both supposed to be constant while Z is given by Equation 2.19. $\tilde{\sigma}$ and $\tilde{\gamma}$ are both constant, and $\tilde{p}$ is proportional to x^2, which slightly changes with x. A much stronger dependence of $\boldsymbol{\tau}^{nuc}$ on x comes from the term C_{n^*} due to its exponential form.

2.4 Characteristic time of the ATG instability

As already analysed in Equation 1.9 [49], length scale of the ATG instability can be deduced from the diffusion equation resulting from the competition between elasticity and capillarity. The instability length scale is [49]:

$$l_0 = \frac{\gamma}{2\zeta\varepsilon_0} \tag{2.22}$$

while the associated time scale can be written as:

$$t_0 = \frac{l_0^4}{\gamma D_s} \tag{2.23}$$

where D_s is the surface diffusion coefficient as mentioned above. The characteristic time of the ATG instability describes the time scale of the kinetic morphological evolution, typically indicating the time required for morphological roughening. While looking for a quantitative relation between ATG instability time scale, one would easily find $t_0 \propto x^{-8}$ since l_0 is proportional to x^{-2}.

2.5 Growth mode competition

With all the parameters and the model proposed above, one can estimate the time scale for nucleation and ATG instability respectively. While taking the growth temperature $T = 550\,°C$ as in our experiments shown later on, and we choose the reasonable value of the surface energy anisotropy $\eta = 0.003$ and edge energy density $\sigma^{ed} = 3.3 meV/Å$, which is in the same magnitude of $\sigma^{ed} = 10 meV/Å$ in order to fit our experimental results. Within these parameters the nucleation time scale and characteristic time of the ATG instability are plotted in Figure 2.5, with a cross-over composition $x_c = 0.55$.

We see that the nucleation time scale τ^{nuc} is much shorter than the characteristic time t^{ATG} in high strain regime and nucleation occurs quickly before the instability mode. However, when the composition x decreases, τ^{nuc} exponentially shoots up and turns to be a more time-consuming pathway since t^{ATG} simply varies as x^{-8}. In order to figure out clearly the quantitative relation of τ^{nuc} with x, an approximate formula can be given as:

$$\tau_{app}^{nuc} \approx \tau_0^{nuc} e^{(b\frac{\gamma^3}{x^4} + c\frac{\gamma\sigma^{ed}}{x2})} \tag{2.24}$$

where τ_0^{nuc}, b and c are all constants. This formula shows similar trend as τ^{nuc}, shown in Figure 2.5.

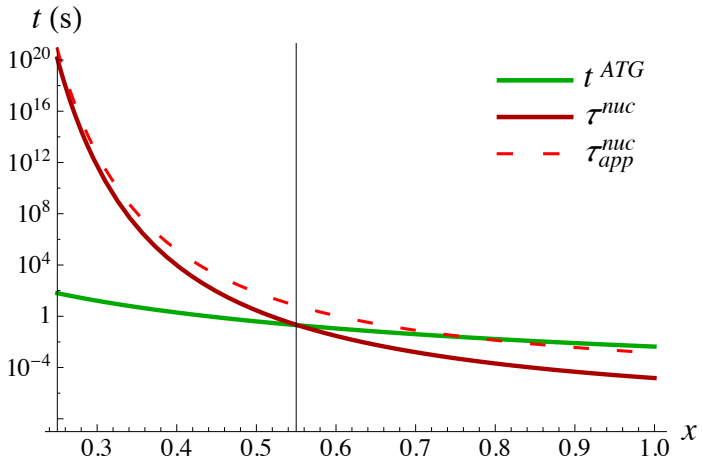

Figure 2.5: As a function of composition x, the nucleation time scale is plotted in red solid curve, characteristic time of ATG instability in green curve and the red dashed curve represents the nucleation time scale which is approximated as in Equation 2.24, and the vertical line marks the crossover composition.

2.6 Experiments

The experiments to identify the two different evolution pathways are performed in a Riber MBE (Molecule-beam epitaxy) system with pressure down to $10^{-11} torr$, in which Si deposition flux is produced by electron-beam evaporator while the Ge flux comes from an effusion cell. The deposition rates are both precisely calibrated by RHEED (Reflection high-energy electron diffraction). Si(001) substrate is firstly cleaned by chemical method and then transferred into MBE growth chamber. After flashing the substrate at 1000 °C for 3min, a buffer layer with thickness of 40nm is deposited to make a reproducible clean surface at 750 °C . Then the substrate temperature is decreased to 550 °C , Si and Ge are co-deposited with SiGe rate of 0.04-0.05 nm/s. The sample holder is always kept rotating during the deposition. As the deposition stops, the samples are cooled down to room temperature immediately and subsequently taken out for morphological characterization using AFM (Atomic Force Microscopy) in non-contact mode. The images are shown in Figure 2.6. We precisely control the epilayer thickness to catch the onset of surface roughening and finally find that the evolution pathways are clearly distinguishable with thickness of 2.0 nm for $Si_{0.5}Ge_{0.5}$ and with 1.3 nm for $Si_{0.4}Ge_{0.6}$.

In Figure 2.6 a, the morphology roughens on the whole surface with a similar scenario of ATG instability[26, 25], the wavelength of which can be conveniently extracted from a ring-like Fourier Transform image to be 80 nm. The continuous roughening is more clearly highlighted in the line profile in Figure 2.6 c and d. On the contrary, for $Si_{0.4}Ge_{0.6}$ in Figure 2.6 b, islands nucleate discretely on the surface while the substrate remains flat which is evidenced by the profile in Figure 2.6(b) where we see isolated islands and the background roughness is around 0.3 nm, merely in the magnitude of

AFM noise. Its Fourier Transform image is a full disk, showing no long-range ordering. All of them characterizes the nucleation pathway as for Ge/Si(001). At 550°C , we evidence that the cross-over composition lies between 0.5 and 0.6.

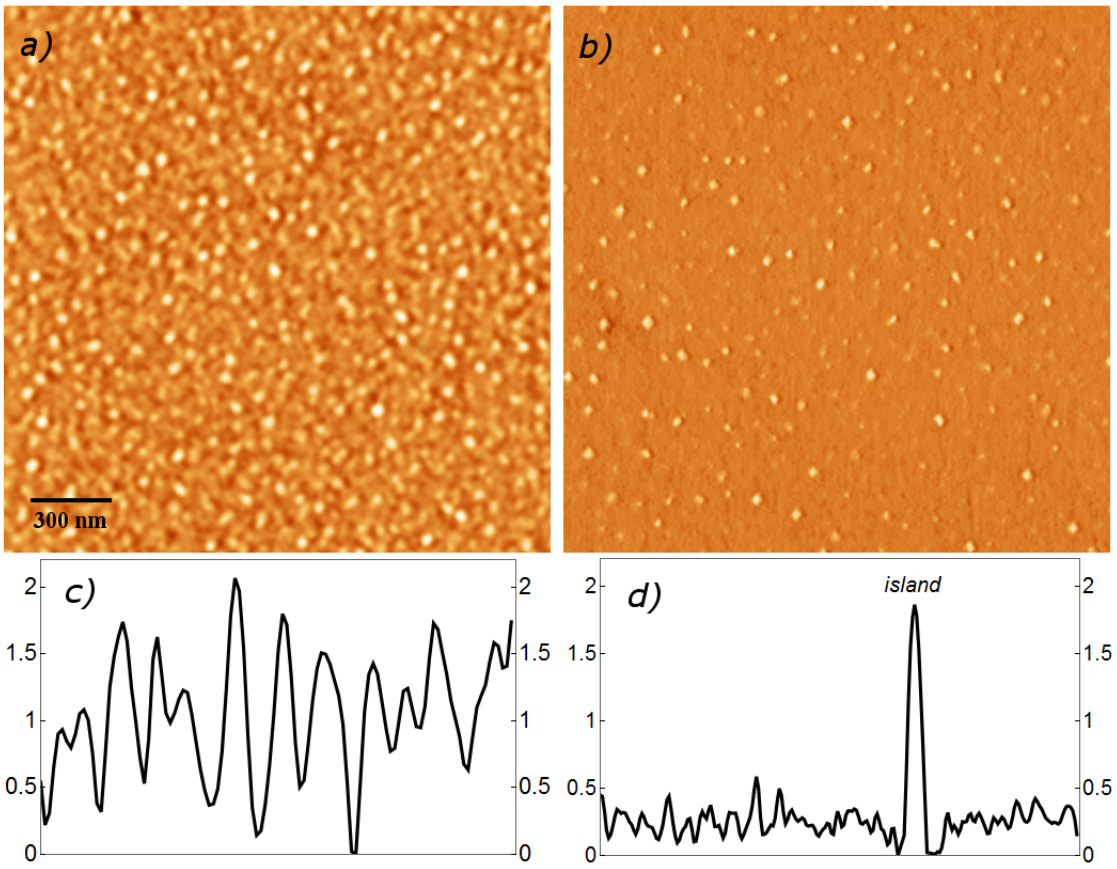

Figure 2.6: Experiments to identify cross-over composition x_c. AFM images of (a) 2 nm $Si_{0.5}Ge_{0.5}$ and (b) 1.3 nm $Si_{0.4}Ge_{0.6}$ deposited at 550°C . (c) and (d) are typical profiles taken respectively from (a) and (b).

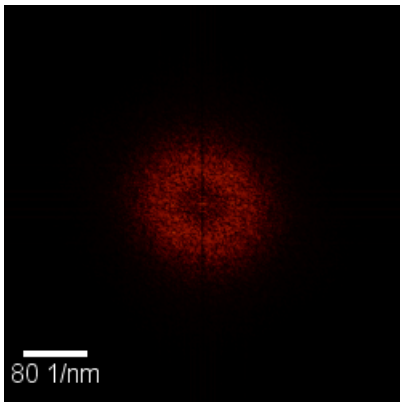

Figure 2.7: The FFT image of figure Figure 2.6(a). The corresponding wavelength is found to be around $80nm$

2.7 Discussions

In the proposed model, some assumptions are made to simplify the problem. We firstly assume that the surface energy of the $Si_{1-x}Ge_x$ epilayer is always taken as the surface energy of Ge. A second assumption is that the pathway of nucleation follows a growing pyramid, meaning that the island is always a pyramid at any state of nucleation. We discuss below these assumptions.

2.7.1 Nucleation pathways

The nucleation pathway of pyramidal islands has been found to be a complex issue. In-situ STM unveiled that ad-atoms firstly form pre-pyramids which subsequently turn to truncated pyramids and pyramids. Here we test the pathway going through truncated pyramids for comparison with that via full pyramids.

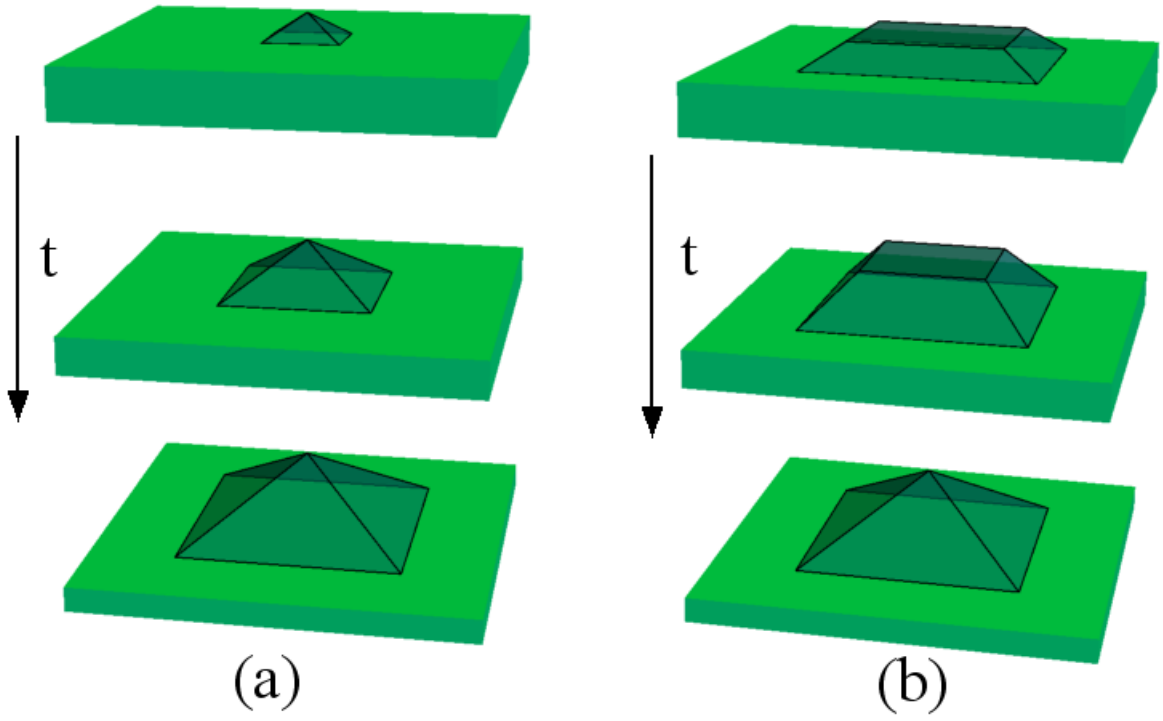

Figure 2.8: Two different pathways of pyramidal island nucleation:(a) full pyramid pathway, the island is always (105)-faceted (b) truncated pyramid pathway, the base length is obtained by computing the V^* of pathway (a) and island grows by stacking materials with (105) facets on sides.

By pathway(a), we calculate the nucleation energy barrier ΔE^* and critical volume V^* and its base length L^*. For comparison, we fix the base length of truncated pyramid as L_c, and the island forms by growing materials on the top of truncated pyramid which bounded by (105) facet on side and (001) on top. We compute the shift of energy barrier

and substitute it τ^{nuc}. As a result, the nucleation time scale of the truncated pyramid pathway τ^{nuc}_{trunc} can be calculated.

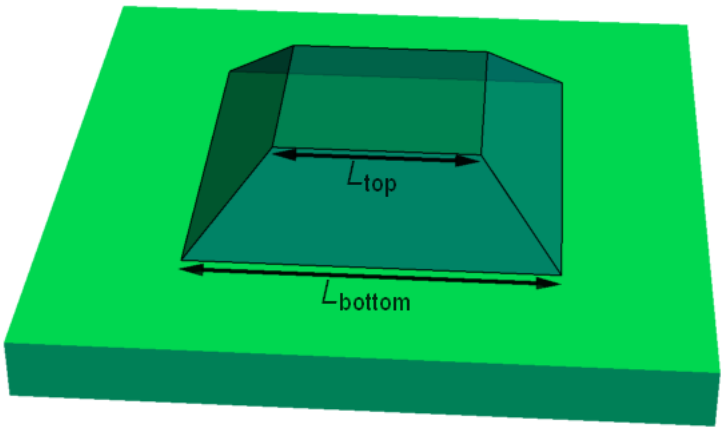

Figure 2.9: Schematic figure of a coherent truncated pyramid

The elasticity of coherent truncated pyramid has been dealt with the half-plane Green function in the small-slope approximation [54]. We introduce a parameter $\kappa = L^{top}/L^{bottom}$ for the definition of truncated pyramid shape, see Figure 2.9. The elastic energy is then given by:

$$\Delta E^{el}_{trunc} = -\zeta g(\kappa)\varepsilon_0 V \tag{2.25}$$

where $g(\kappa)$ corresponds to the truncated shape, which is[54]

$$g(\kappa) = \frac{1}{1-\kappa^3}\{\frac{1}{3}[\sqrt{2}-\ln(\sqrt{2}+1)](2+\kappa)(1-\kappa)^2+\frac{2}{3}[\sqrt{2}\ln(1+\sqrt{2})-1](1+\kappa^3)-\Xi(\kappa)\} \tag{2.26}$$

with

$$\begin{aligned}\Xi(\kappa) = &-\frac{2\kappa}{3}\sqrt{2+2\kappa^2}+\frac{2\kappa^3\sqrt{2}}{3}\ln\frac{1+\sqrt{1+\kappa^2}}{\kappa}+\frac{2\sqrt{2}}{3}\ln(\kappa+\sqrt{1+\kappa^2})\\ &-\frac{1-\kappa-\kappa^2+\kappa^3}{2}\ln\frac{1+\kappa+\sqrt{2(1+\kappa^2)}}{1-\kappa}+\frac{1+\kappa-\kappa^2-\kappa^3}{2}\ln\frac{1-\kappa+\sqrt{2(1+\kappa^2)}}{1+\kappa}\end{aligned} \tag{2.27}$$

As regards the surface energy variation, it is given in the geometry under study by:

$$\Delta E^{surf}_{trunc} = [\frac{6}{\tan\theta(1-\kappa^3)}]^{2/3}(1-\kappa^2)(\frac{\gamma^{105}}{\cos\theta}-\gamma^{001})V^{2/3} \tag{2.28}$$

Finally, the whole geometrical shape is still bounded by facet (001) and (105)and all the crystal edges are regarded with the same edge energy density σ^{ed}. As a result, the edge energy reads:

$$\Delta E^{ed}_{trunc} = 4(\frac{6(1-\kappa^3)}{\tan\theta})^{1/3}[1+\sqrt{\frac{1}{2}+\frac{\tan^2\theta}{4}}+\kappa(1-\sqrt{\frac{1}{2}+\frac{\tan^2\theta}{4}})]\sigma^{ed}V^{1/3} \tag{2.29}$$

We calculate the energy barrier of truncated pyramid and plot it together with that of pyramid pathway, see Figure 2.10, where $x = 0.5$ as an example. We find that the change of pathway only leads to an increase in the energy barrier of about $0.1eV$, see Figure 2.10. The increase shifts the crossover composition x_c of about 0.55 to $x_c \simeq 0.60$, see Figure 2.11.

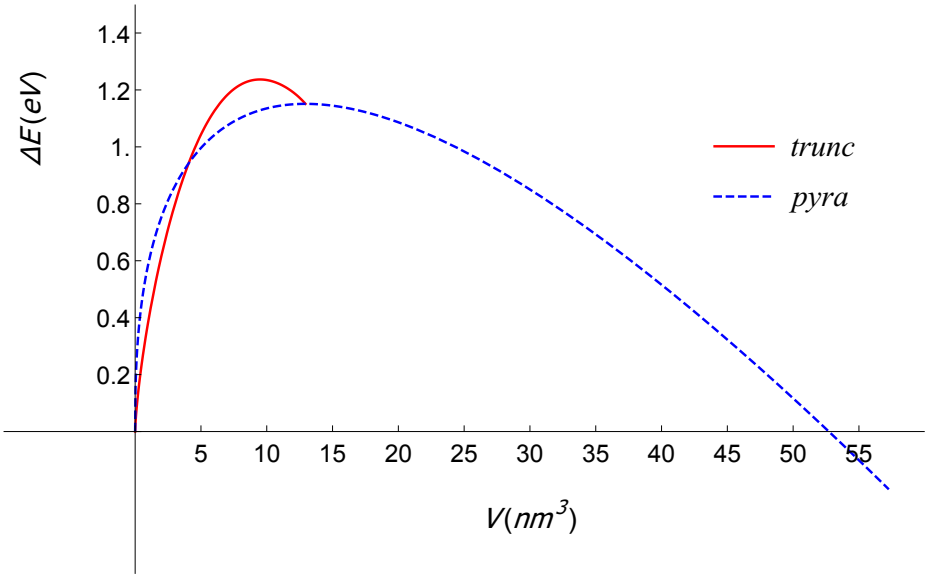

Figure 2.10: The energy barrier variation of truncated pyramid pathway and pyramid pathway.

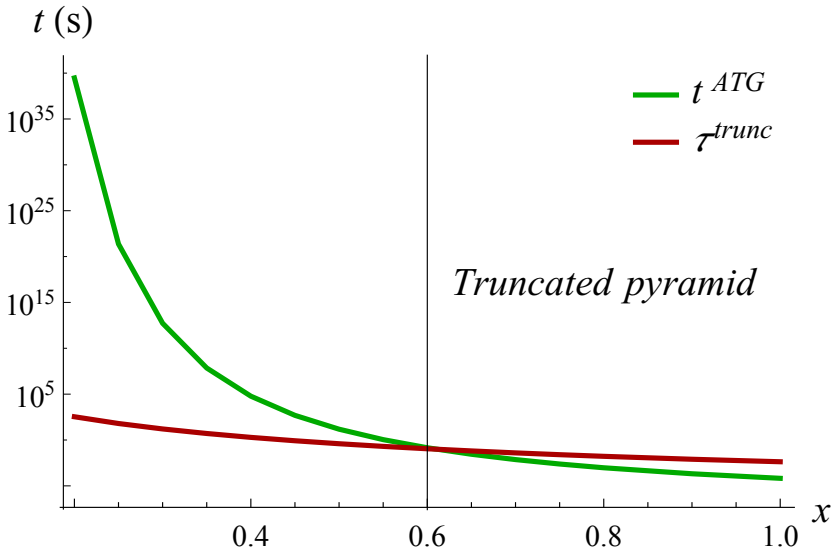

Figure 2.11: The crossover composition x_c shifts from 0.55 to around 0.6 when the truncated pyramid pathway proceeds.

2.7.2 Surface energy anisotropy

One assumption we made in our calculation is that pure Ge fully segregates on the surface so that the surface energy is approximated to be the surface energy of Ge.

What really matters in our calculation is the surface energy variation from facet (001) to (105),which is mesured by one parameter η, defined in Equation 2.4. In fact, this parameter is not a constant while we change composition x for a non segregated surface. The surface energy density of strained film is found to be a function of its surface strain. Their dependence on strain can be evidenced from first-principle calculations at $0K$[22, 23, 13], in which we see that γ^{105} is smaller than γ^{001} while $\gamma^{105} > \gamma^{001}$ when the strain is relaxed. As an example, the surface energy variation for a layer with strain 3% (roughly correspongding to $Si_{0.3}Ge_{0.7}$) is marked by a two-head arrow in Figure 2.12, which is smaller than that with strain 4.2%. By the way, this result actually gives an explanation to the stability of (105) facet.

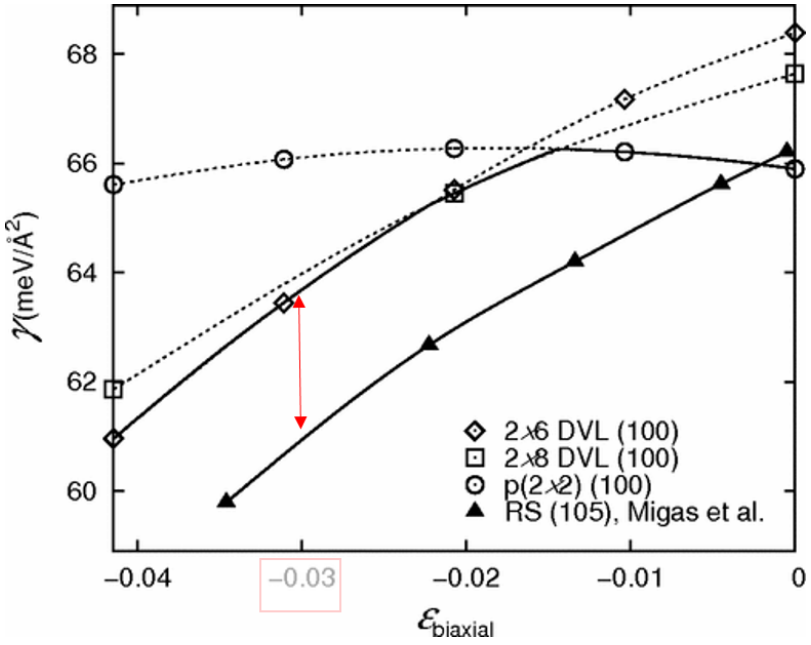

Figure 2.12: Surface energy as a function of strain, respectively for facet (001) and (105). Two-headed red arrow marks the surface energy variation for 0.3% strained layer.[23]

Now we take this effect into account by assuming now that the surface is not segeregatetd and assuming the Vegard's law for the surface energy. Consequently η is a parameter depending on the composition x and their quantitative relation $\eta(x)$ can be obtained by fitting the first-principle results in [23]. For convenience to compare the result, we shift slightly the curve so that $\eta(0.55) = 0.003$ which will lead to a crossover of full pyramid pathway at $x = 0.55$ when it is taken as constant. Then the formula of $\eta(x)$ is obtained as:

$$\eta(x) = 0.02132 - 0.0270x - 0.0114x^2 \tag{2.30}$$

With this second set of hypothesis, we plot the corresponding nucleation time scale with respect to ATG instability time scale in Figure 2.13. We find that the strain-dependent surface energy anisotropy makes the cross-over more robust in terms of x. In the high-strain regime, nucleation occurs more rapidly for a smaller η, which actually decreases

the energy barrier. In the low-strain regime, anisotropy becomes a stronger resistance and the energy barrier increases, resulting in a larger nucleation time.

The sharper cross-over implies that it is less sensitive to other uncertainties including alloying effect, temperature effect and so on.

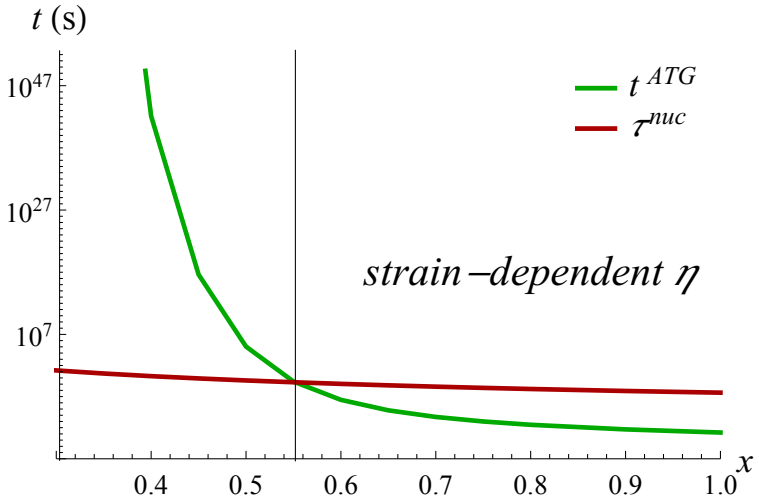

Figure 2.13: The surface energy anisotropy is regarded as a strain-dependent factor according to first-principle calculation, it actually results in a sharper cross-over at $x = 0.55$.

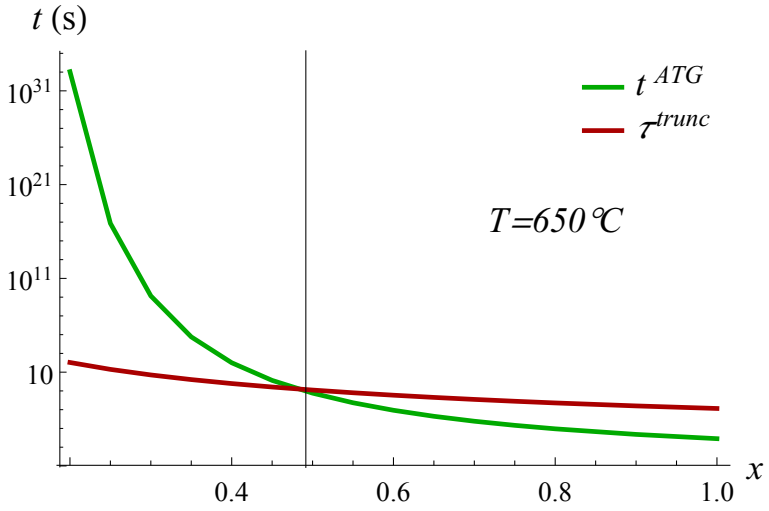

Figure 2.14: The growth temperature is changed to 650 °C and one can find that the crossover composition shifts to around $x = 0.5$.

2.7.3 Growth temperature

The growth temperature rules not only the kinetics of adatoms, but also the nucleus distribution. In Equation 2.14, thermal fluctuation energy $k_B T$ as well as the surface diffusion coefficient in Equation 2.20 and Equation 2.23 are related with temperature T. In our previous discussion, experimental temperature 550 °C is taken as an example.

Here we try to figure out if the crossover composition x_c is sensitive to the growth temperature. The cross-over composition x_c moves toward low-strain regime to around 0.5 when the growth temperature is set to be 650 °C . Higher temperature results in a higher thermal fluctuation energy $k_B T$ that reduces the nucleation time scale due to the Boltzmann factor in the nucleation theory. However the shift due to temperature does not lead to a significant change of x_c, which supports the validity of our results.

2.8 Conclusion

In this chapter, we proposed a model aimed to clarify the two morphological evolution pathways of strained epilayer, depending on the amount of strain. Firstly, we calculated the formation energy of a pyramidal island on a strained epilayer as a function of island volume, taking surface energy, elastic energy and edge energy into account. The nucleation energy barrier increases while decreasing the amount of strain. Using the master equation that governs the system kinetics, we calculated the nucleation time scale. With respect to composition x or amount of strain, the nucleation time scale is found to shoot up while decreasing x, quantitatively as $\tau_0^{nuc} e^{(b\frac{\gamma^3}{x^4}+c\frac{\gamma\sigma^{ed}}{x^2})}$. On the contrary, the time scale of the ATG instability evolves merely as $1/x^8$. At high strain, the nucleation time scale is shorter and nucleation dominates. However it rises rapidly when x decreases and exceeds the time scale of ATG instability at a medium composition about $x = 0.55$ at growth temperature 550 °C . This result is consistent with the experimental results

Some issues and parameters were discussed in order to offer a solid ground to our results. Firstly, the pathway of pyramid nucleation still remains as a controversial problem. We considered the truncated pyramid pathway and found that the cross-over composition moves slightly. Secondly, the amount of surface energy anisotropy is supposed to be a strain-dependent following the first-principle calculations at $0K$, which leads to sharper cross-over at a composition around $x = 0.55$; at the end, we discussed the effect of the growth temperature and found it shifts slightly the cross-over composition toward lower strain. As a whole, we performed a joint work in theory and experiments to figure out the two different pathways of 3D island formation from strained 2D epilayer, shedding some more light to this fundamental issue. We argue that our model can be applicable to other epitaxial systems.

Chapter 3

Role of Strain-dependent Surface Energy in Islands Interaction

Contents

The interaction between coherent islands plays a crucial role in terms of fabricating dense, homogeneous islands. The coherent islands which interacts via the long-range elastic field shows plenty of complexities. It still remains as an issue of controversy both from the experimental and theoretical point of view. A priori elastic interactions between two islands are repulsive. In this chapter, we demonstrate evident attraction between islands. Theoretically, we find that a strain-dependent surface energy indeed induces and effective attractive interaction that can compensate for the repulsion caused by elastic interaction, driving the islands to form adjacently. Based on the nucleation theory, we estimate the effect of inhomogenous elastic field around an existing coherent island.

3.1 Background

The interaction between coherent islands is a significant issue to get a controllable self-organization of QDs. Generally speaking, the elastic relaxation on islands induces repulsive dipoles[58].

However one also knows the surface energy of coherent islands is significantly dependent on surface strain. This effect has been overlooked previously in the analysis of AD nucleation. Employing first-principle calculations, O.E. Shklyaev et al.[13, 23] computed the quantitative relation between the biaxial strain and surface energy.

3.2 Experiments and Island Distribution Analysis

3.2.1 Experiments to study island distribution

We clean the Si substrate and prepare the substrate using standard Shiraki method. In the experiment under investigation, 1nm of Ge is deposited at 550°C onto a 4-inch nominal Si(001) wafer and islands on the surface are observed by plan-view TEM (Transmission Electron Microscopy). A quick inspection reveals that the islands seem to nucleate in groups. We now try to quantify this effect.

3.2.2 Quantifying island distribution via correlation function

In order to quantitatively investigate the correlation between islands, we use the correlation function of their mass centers. For an assembly of M islands, their projection on the plane is considered, and especially their center positions $\boldsymbol{r}_i, i = 1,2...M$. The single particle and pair densities can be defined as usual as $n(\boldsymbol{r}) = \sum_{(i=1)}^{M} \delta(\boldsymbol{r} - \boldsymbol{R}_i)$, and

$$\rho^2(\boldsymbol{r}, \boldsymbol{r}') = \langle n(\boldsymbol{r}) n(\boldsymbol{r}') \rangle - \langle n(\boldsymbol{r}) \rangle \delta(\boldsymbol{r} - \boldsymbol{r}') \tag{3.1}$$

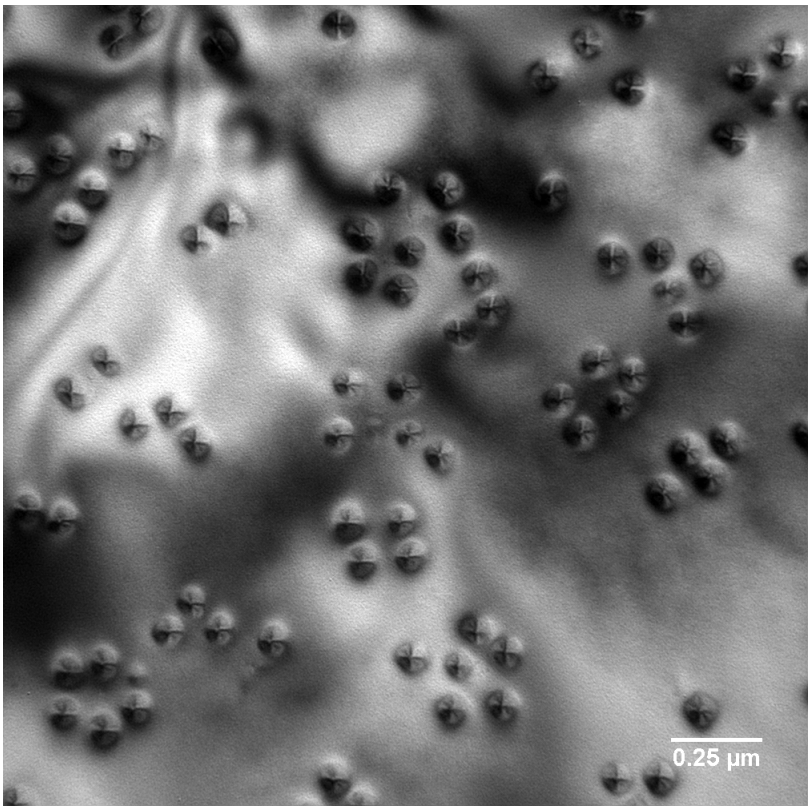

Figure 3.1: Plan-view TEM image of Ge/Si(001) islands

In an homogeneous and isotropic system with an island density ρ, correlations between islands can be characterized by the distribution function:

$$g(r) = 1/(M\sigma) \int d\boldsymbol{r}' \rho^2(\boldsymbol{r}+\boldsymbol{r}', \boldsymbol{r}') \tag{3.2}$$

We plot in Figure 3.3 the distribution function $g(r)$ corresponding to the experimental results of Figure 3.1. We see clearly that at a distance slightly larger than the cut-off, of the order of the mean island diameter σ, a peak of $g(\boldsymbol{r})$ appears with a maximum value $g_{max} \simeq 2.5$.

In order to quantify the interactions between islands, we compare the experimental distribution function with the theoretical one associated with the equilibrium property of a hard-disk fluid with a diameter σ. The contact value of this distribution is indeed simply related to the 2D pressure, $P/\rho k_B T = 1 + B_2 \rho g(1)$ with $B_2 = \frac{1}{2}\pi\sigma^2$. Hence $g(\sigma)$ appears as a peak due to the correlation introduced by the hard-disk effect. The value of $g(\sigma)$ at equilibrium can be estimated via some well-known approximation at low density, which is the case in our experiments.

From the Padé approximant of Born-Green-Yvon (BGY) approximation, one can estimate the value of $g(\sigma)$ for a given particle density. Here we consider $\rho\sigma^2 = 13\%$, of the experimental of Figure 3.1, and get $g(\sigma) = 1.19$. Similarly , the Padé approximation of Monte-Carlo simulations leads to the value of $g(r) = 1.20$. As a consequence, the maximum value $g(r)_{max} \simeq 2.5$ in our experiments clearly indicates that the correlation between islands is beyond the hard-core effects.

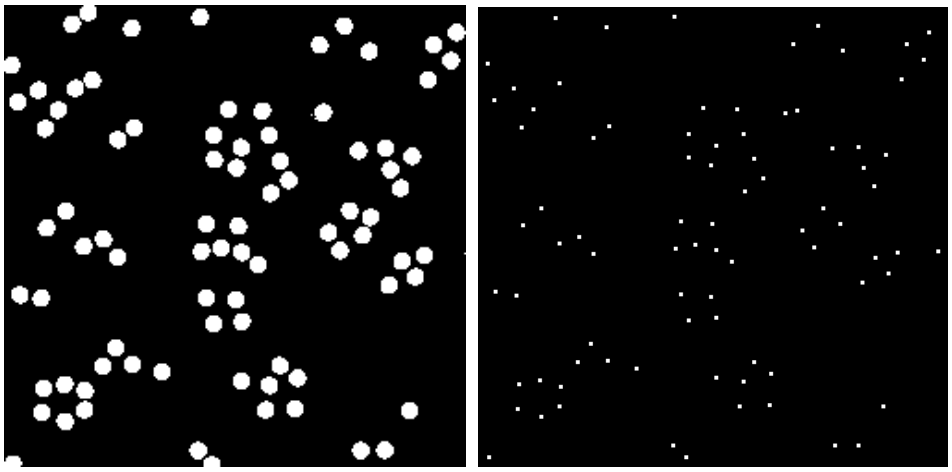

(a) (b)

Figure 3.2: (a) The projections of islands in experiments (b) the mass centers of islands, which also gives the island coordinates $\boldsymbol{r}_i$

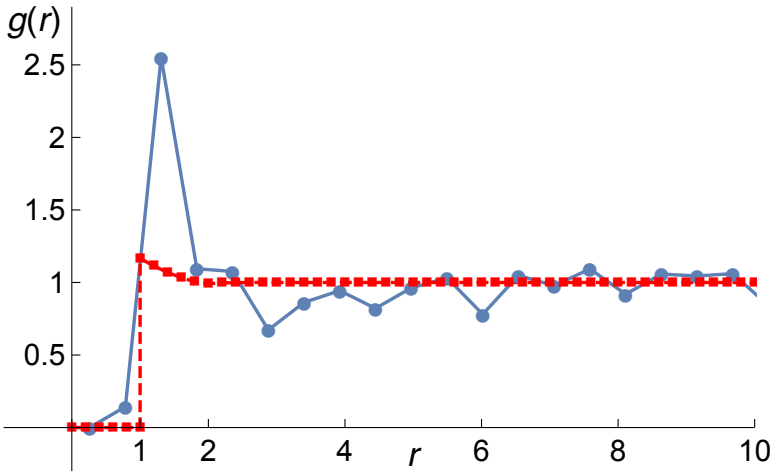

Figure 3.3: Distribution function $g(r)$ (solid blue line) of the islands found experimentally as a function of their distance r in unit of the mean island diameter σ. The red dashed curve corresponds to the theoretical distribution function of hard-core disks with the same island density (that is $\phi = 13\%$) in the Born-Green-Yvon approximation

3.3 Interactions between coherent islands via elasticity

In this section, we investigate the island-island interaction based on the elasticity theory of coherent islands. As mentioned, island interaction is related to the elasticity that is a long-range effect. Apart from the elastic term induced by the direct elastic interactions, the strain-dependent surface energy is also taken into account. First, we compute the energy of a two-island system; then, we consider the kinetics of nucleation of an island as a function of distance from which it nucleates away to an existing island.

In our calculations, the flat epilayer is regarded as a reference state, with respect

to which energetic variation including elastic energy ΔE^{el}, surface energy ΔE^{surf}, and edge energy ΔE^{edge} are calculated. The total energy variation ΔE^{total} is simply:

$$\Delta E^{total} = \Delta E^{el} + \Delta E^{surf} + \Delta E^{edge} \tag{3.3}$$

where the only difference compared to Chapter 2 is the existence of two pyramids.

3.3.1 Elasticity

(a)Elastic energy

Elasticity of the two-island model is handled within the small-slope approximation. The total elastic energy E^{el} can be directly related to the morphological function $h(\boldsymbol{r})$, see Equation 2.6.

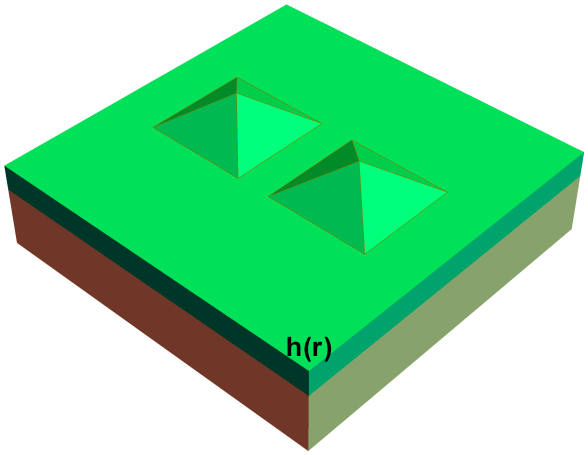

Figure 3.4: Geometry of two-island model: two islands with given distance, the computation box size is set large enough to avoid the interaction with adjacent computation box.

(b)Strain-dependent surface energy

The second term associated with long-range effect is the strain-dependent surface energy $\gamma(\bar{\bar{\epsilon}})$. The quantitative relation between biaxial strain on the $\bar{\bar{\epsilon}}$ and the surface energy $\gamma(\bar{\bar{\epsilon}})$ is an issue of great importance to understand the formation of (105)-faceted pyramid. Employing first-principle calculations, a couple of groups calculated the stability of facet (105) and (001) at different surface reconstructions while surface strain applied. The estimate of $\gamma^{105}(\bar{\bar{\epsilon}})$ and $\gamma^{001}(\bar{\bar{\epsilon}})$ respectively for (105) and (001), are available from these published results[23],[13].
The absolute values of the surface energy from these groups are not fully consistent. However, the variation of surface energies as a function of $\bar{\bar{\epsilon}}$ are rather in good agreement, which will be the major factor at work in terms of island-island interaction induced by strain-dependent surface energy. We consider the result by O.E. Shklyaev et

al.[23], and consider the reconstruction (2×8) into account as it is expected to be the relevant surface reconstruction of the wetting layer. Finally we get:

$$\gamma^{(001)}(\epsilon) = 67.2 + 156.3\epsilon \tag{3.4}$$

$$\gamma^{(105)}(\epsilon) = 60.0 + \delta_\gamma + 103.6\epsilon - 1577.8\epsilon^2 \tag{3.5}$$

where the unit of surface energy is $meV/\text{Å}^2$ and we introduced a parameter δ_γ to avoid the (105) facet to be always energetically favorable due to a too low value compared with (001). This issue can be quantified by Equation 2.4, which is rewritten again here for convenience:

$$\eta = \frac{\gamma_{Ge}^{105}}{\gamma_{Ge}^{001}} \frac{1}{\cos\theta} - 1$$

It describes the role of surface energy variation in the process of pyramidal island formation. When $\eta > 0$, the surface energy variation is positive, meaning it plays as a resistance. Conversely when $\eta < 0$, the surface energy turns to be a driving force and leads to a permanent stability of (105) facet with respect to (001). The sign of η has been an issue of debate according to different experimental groups. First, no (105) faceting has been found when the thickness of Ge is below the critical thickness h_c, which gives a hint of $\eta > 0$; on the other hand, the elongation of island (hut islands, 2D elongated nanowires) is theoretically rationalized based on the assumption of $\eta < 0$ but with quite high edge energy.
Here we set $\delta_\gamma = 0.8 meV/\text{Å}^2$ so that $\eta = 0.003$, . We note that this parameters allow to rationalize the existence of nucleation behavior and it has no effect to our result associated with the island-island interaction as it merely depends on the surface energy variation as a function of ϵ, not on the absolute value of γ. We plot the $\gamma^{(001)}(\epsilon)$ and $\gamma^{(001)}(\epsilon)$ in Equation 3.5.

Within this framework, one finds:

$$\epsilon(\boldsymbol{r}) = -\delta + \zeta \mathscr{H}_{ii}[h(\boldsymbol{r})] \tag{3.6}$$

where δ , ζ and $\mathscr{H}_{ii}$ have the same definition as in Equation 2.6. To confirm, we calculate the distribution of $\epsilon(\boldsymbol{r})$ in case of one single pyramid to compare with the result obtained by Finite element method (FEM)[23], and indeed find a very good agreement.

Eventually the surface energy variation ΔE^{surf} with the strain-dependent surface energy is the integral of $\gamma(\epsilon)$ within the whole computation box:

$$\Delta E^{surf} = \int_\Delta d\boldsymbol{r}\, \gamma_{Ge}^{(105)}[h(\boldsymbol{r}), \epsilon(\boldsymbol{r})]/\cos\theta + \int_{\overline{\Delta}} d\boldsymbol{r}\, \gamma_{Ge}^{(001)}[h_w, \epsilon(\boldsymbol{r})] - \gamma_{Ge}^{(001)}[h_0, \epsilon_0]/\rho \tag{3.7}$$

where Δ and $\overline{\Delta}$ respectively denote the area of the facets (105) and (001), h_0 and h_w are the initial epilayer thickness and the thickness of wetting layer beneath the islands.

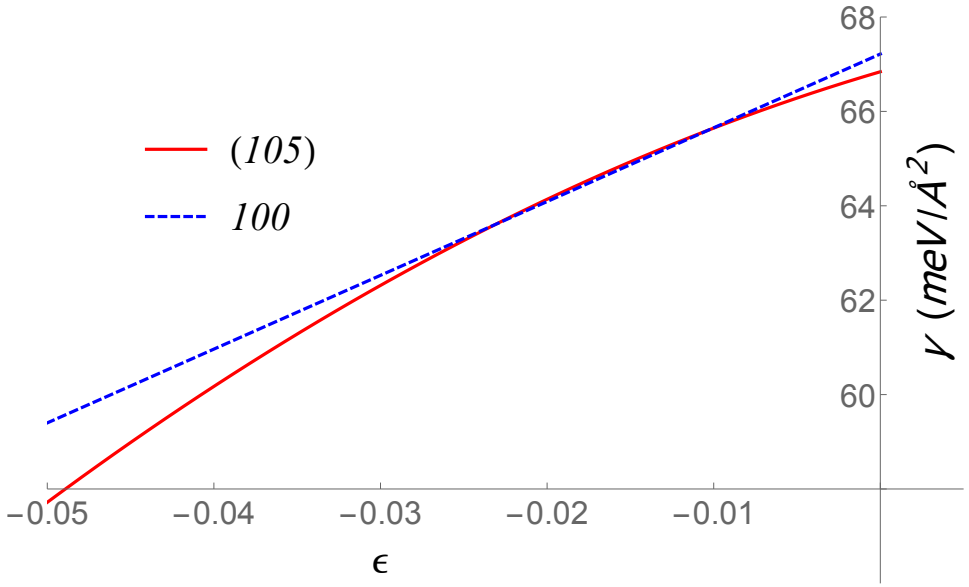

Figure 3.5: The strain-dependent surface energy as a function of ϵ for facet(001) and (105) respectively. Note that only reconstruction (2) of facet (001) is considered as the reconstruction transition occurs at low-strain regime, not associated to the strain regime in calculation

3.4 Two-island interaction in equilibrium state

We study here the energetic equilibrium state of a two-island system. The composition x is firstly set to be 1, and the heights of pyramid are 0.5 nm, indicating that the volume is more than 4 nm^3. We argue that this volume is a priori larger than the critical volume V^*, which is still difficult to determine from experiments. From experiments, pyramid height down to around 1 nm, has been observed by in-situ STM [18], which means the critical volume of pyramids lies still in smaller regime. Based on the model we proposed in Chapter 2, the critical volume for Ge/Si(001) is calculated to be around 4 nm^3. We take this value firstly and at the end of this chapter, the effect of geometry will be discussed.

The island heights (volume) are set to be invariable, while by varying the distance between two islands, the total energy will vary as well.

3.4.1 Biaxial strain in two-island model

The part of great interest in this model is the effect of strain-dependent surface energy which is related to island-island distance via the long-range biaxial strain $\epsilon(\boldsymbol{r})$. To start, we plot the distribution of $\epsilon(\boldsymbol{r})$ when the distance $d = 0$, where we define the distance d as the base-to-base distance as $d = 0$ for two touching islands. The mean strain in this case is -0.042. It is clearly demonstrated that on the facets strain is partially relaxed, while at the area at the foot of pyramids it is dramatically enhanced with $\epsilon = -0.068$ between the islands. In the area far away from islands remains the average strain -0.042, immune of islands.

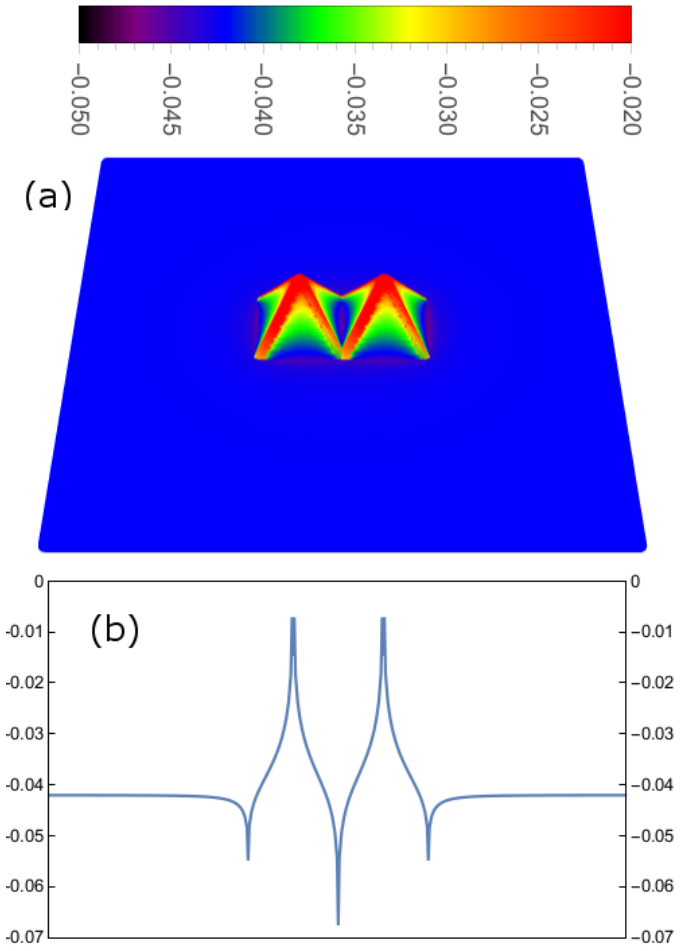

Figure 3.6: (a), The distribution of biaxial strain $\epsilon(\boldsymbol{r})$ is plotted in case of two touching pyramids ($d = 0$), the value of $\epsilon(\boldsymbol{r})$ is represented using colors with scale bar atop; (b), the profile of $\epsilon(\boldsymbol{r})$ along the two vertexes of pyramid, clearly showing the relaxation on pyramids and strain enrichment around the base of pyramids.

We now investigate the distribution of $\epsilon(\boldsymbol{r})$ while changing the island-island distance d. We separate the pyramids with distance $d = 2$ and 4 nm respectively and plot again the distribution of $\epsilon(\boldsymbol{r})$ in Figure 3.7. When the pyramids are separated, $\epsilon(\boldsymbol{r})$ between shows particular variations, which can lead to interaction caused by strain-dependent surface energy. We subsequently investigate the total energy as a function of islands distance.

3.4.2 Energies variation with distance

The equilibrium state of a system is governed by the minimization of its total energy. In a two- island model, ΔE^{el}, ΔE^{surf} are calculated respectively as a function of d, while ΔE^{edge} is independent of the distance. We normalize the energies at $d = 0$ to be 0, and plot them in Figure 3.8. First, the elastic energy ΔE^{el} decreases with d, confirming

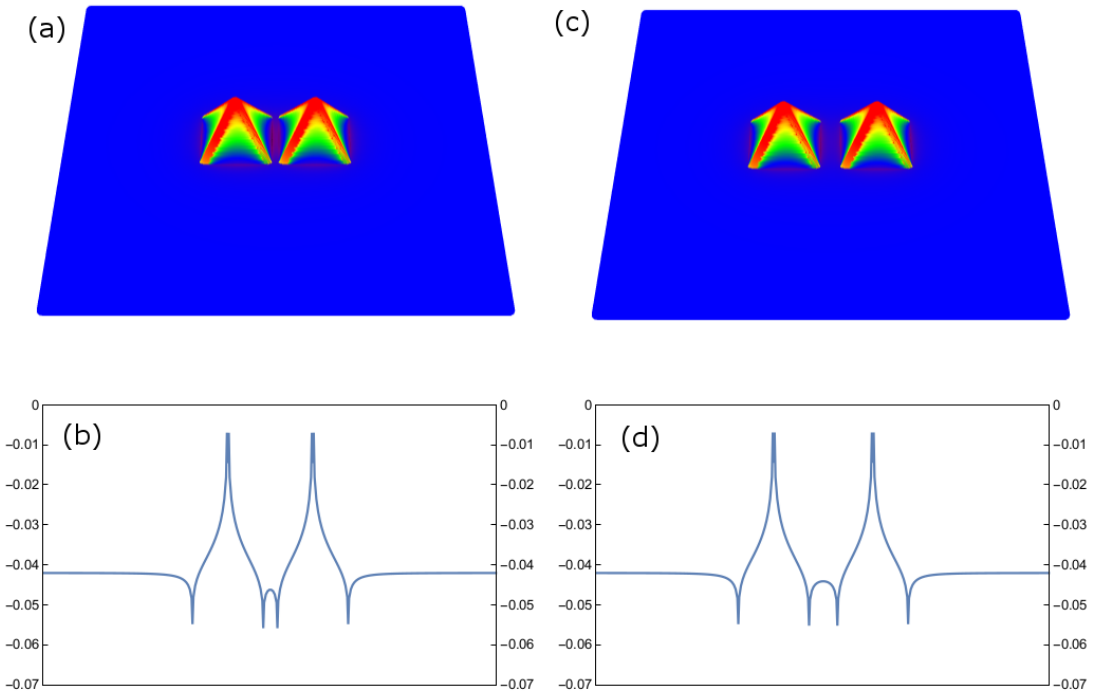

Figure 3.7: (a) and (c), The distribution of biaxial strain $\epsilon(\boldsymbol{r})$ is plotted for $d = 2$ nm and $d = 4$ nm respectively, with the same color scale bar as in Figure 3.6 ; (b) and (d), are the profiles of $\epsilon(\boldsymbol{r})$ along two vertexes of pyramid.

that it describes a repulsive effect between islands, which has been demonstrated in references[51]. However, the surface energy conversely ΔE^{surf} clearly increases significantly with d,revealing an effective attractive interaction between islands, stemming from the strain-dependence of surface energy. Furthermore, in this case, this attraction is strong enough to compensate the repulsion caused by direct elastic interactions, which is clarified by total energy ΔE^{total} in Figure 3.8.

Quantitatively, the amount of attraction of $\gamma(\epsilon)$ can be estimated to be about 0.22 eV while repulsion of elastic effect is 0.14 eV, offering an energy of attraction 0.08 eV, as shown in plot of ΔE^{total}. This attraction is in fact in the magnitude of the thermal fluctuation energy $k_B T$, equal to 0.07 eV at $T = 550\,°\text{C}$. According to the classic nucleation theory (CNT), such an energy difference may lead to a significant change during the nucleation process. Thence it worth deriving a kinetic study using CNT, as done below.

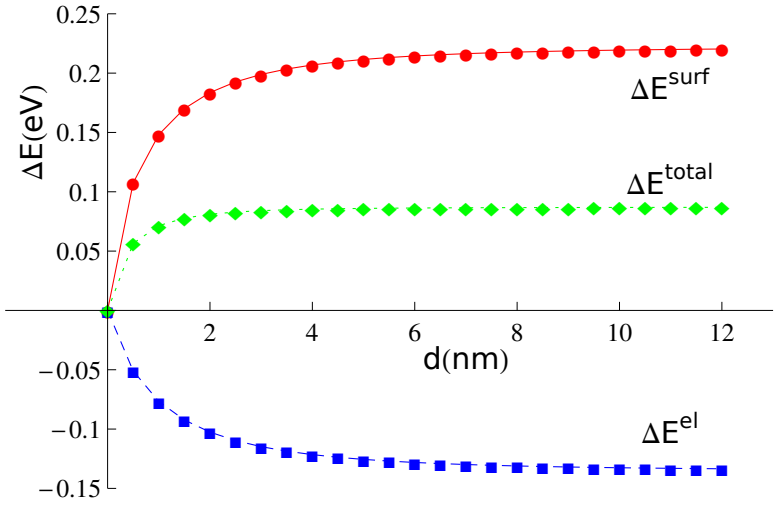

Figure 3.8: The energies ΔE^{el},ΔE^{surf} and ΔE^{total} as a function of d, respectively marked in blue, red and green. The points are obtained from numerical calculations and the lines are here for eye-guide.

3.5 Two-island interaction in nucleation kinetics

In this section, we suppose that one pyramid (PA) has a volume slightly larger than V^* and another pyramid(PB) nucleates adjacently, even though it still remains as a fuzzy issue about whether clustering islands nucleate following a one-by-one process or simultaneously.

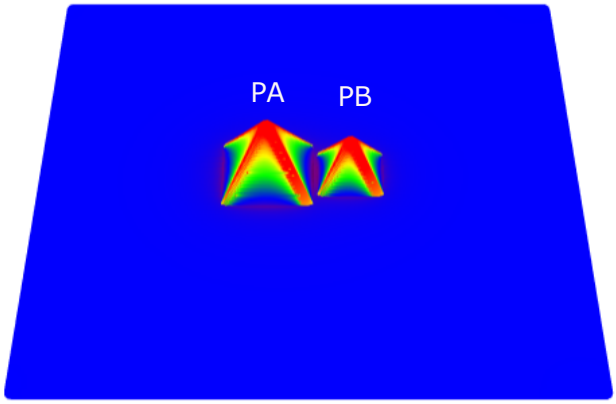

Figure 3.9: PB grows adjacently to PA, with ϵ represented in colors as Figure 3.6

PA firstly forms from a wetting layer h_0, and locates in the center of the computation box. The size of PA is chosen similarly as above according to the calculation of nucleation. The nucleation energy barrier of PB is studied while varying its distance away from PA. During the whole process, mass conservation is always ensured. For

$d = 0$, we plot it in Figure 3.9 as an example.

We then calculate the energy barrier as a function of distance d that is merely varied discretely as 0, 0.5, 2, 8 nm respectively, the nucleation energy barriers of PB are plotted inFigure 3.10. The minimum energy barrier of PB is found when it locates close to PA, due to the inhomogeneity of elastic field induced by PA. This effect may lower the energy barrier about 0.1 eV, making the adjacent area the energetic favourable sites of nucleation.

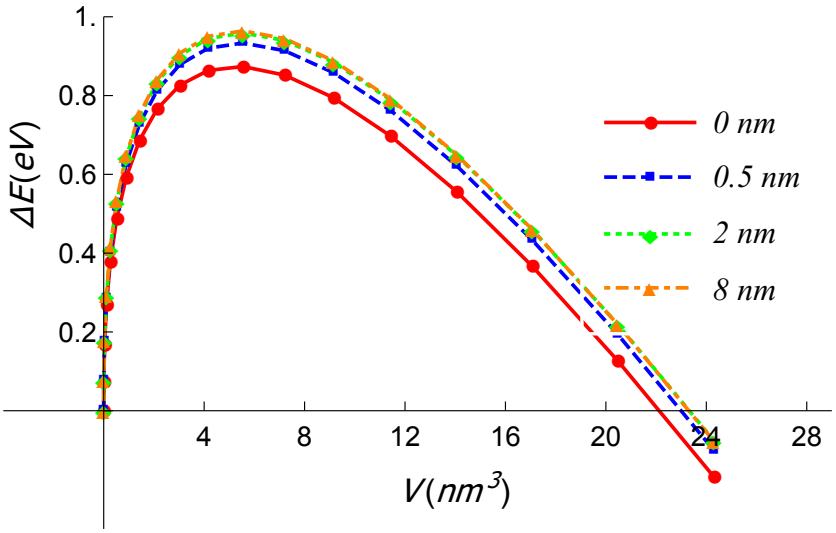

Figure 3.10: The energy variation ΔE^{total} as a function of V of PB while varying the distance d from PA, marked as different colors, red, green, blue and yellow respectively for $d = 0$ nm, $d = 0.5$ nm, $d = 2$ nm and $d = 8$ nm.

3.6 Uncertainty of Strain-dependent surface energy

A couple of studies have been dedicated to the calculation of the strain-dependence of the surface energy via first-principle calculations[23][13]. Their results show that at low strain, $\gamma^{(001)} < \gamma^{(105)}$; at high strain, $\gamma^{(001)} > \gamma^{(105)}$ so that (105) shows as a more stable facet.

Since there exists the transition of reconstruction for facet (001) while various amount of strain is applied, the practical quantitative formula $\gamma^{(001)}(\epsilon)$ is difficult to get because the inhomogeneous strain induces different kinds of reconstruction which shows different strain dependence. We know that at $\epsilon = 0$, $\gamma^{(001)}(\epsilon)$ is lower than $\gamma^{(105)}(\epsilon)$ while first-principle calculations reveals that $\gamma^{(105)}(\epsilon)$ decreases more rapidly than $\gamma^{(100)}(\epsilon)$ and show lower surface energy at $\epsilon = -0.042$. Consequently we can argue that the two curves of $\gamma^{(001)}(\epsilon)$ and $\gamma^{(105)}(\epsilon)$ should intersect within the strain regime from -0.042 to 0. We already mentioned that the interaction caused by the strain-dependent surface energy is related to the slope difference between these two curves. To test this effect, we try to vary the slopes of $\gamma^{(001)}(\epsilon)$ but keeping it in the regime of uncertainties of the

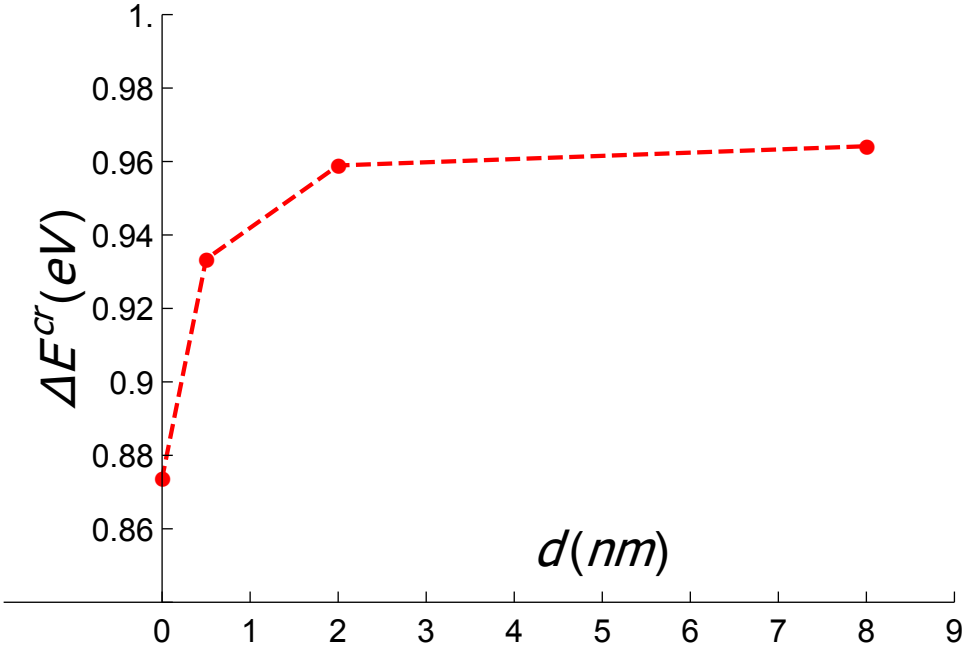

Figure 3.11: The nucleation energy barrier of forming a pyramid as a function of its distance away from an existing pyramid.

first-principle calculations. The two strain-dependent curves are modified and plotted in Figure 3.12.

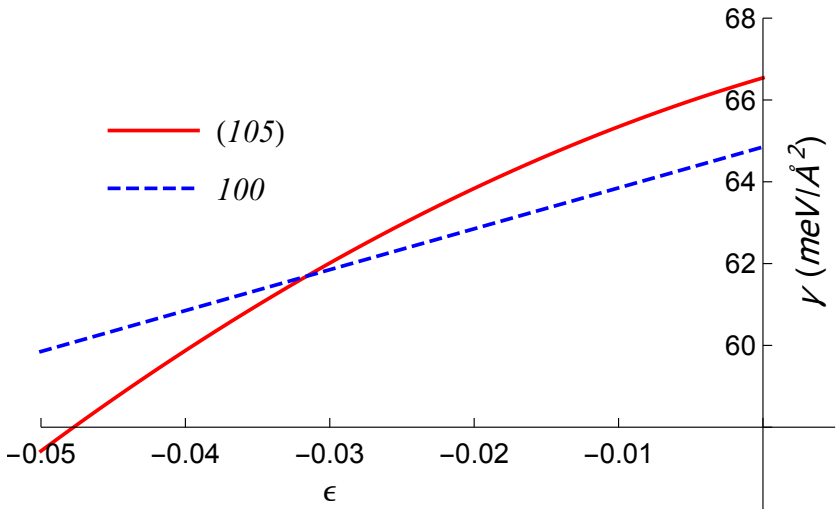

Figure 3.12: The slope of $\gamma^{(001)}(\epsilon)$ is modified in order to check the uncertainty about the first-principle results in references.

With the modified surface energy, we plot the energy of PB and nucleation barrier as a function of distance respectively of two-island model in Figure 3.13 and Figure 3.14. The energy barrier difference increases to 0.2 eV, or about 1 meV/atom if we divide it by the atomic number in a nuclei with critical volume. We see that at larger distance, the critical volume of nucleation increases, which can be another point that make the island favorable at closer position.

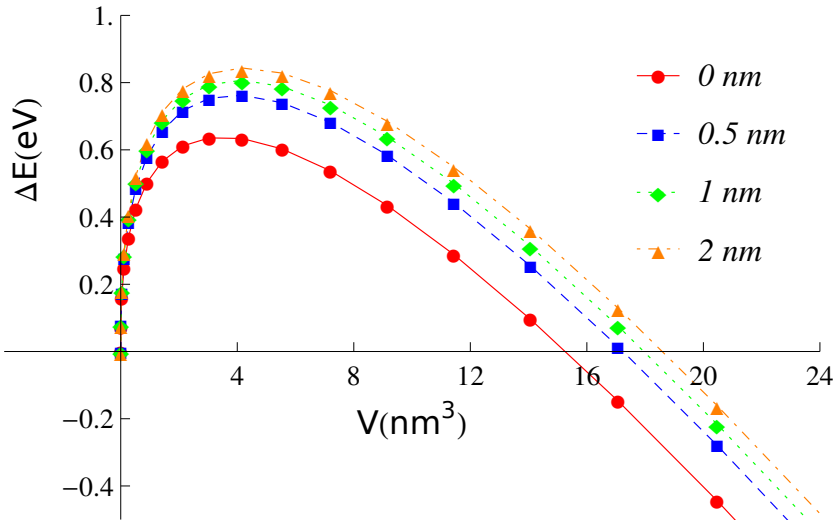

Figure 3.13: In case that the strain-dependent surface energy curve is modified, the energy variation ΔE^{total} as a function of V of PB while varying the distance d from PA, marked as different colors, red, green, blue and yellow respectively for $d = 0$ nm, $d = 0.5$ nm, $d = 2$ nm and $d = 8$ nm.

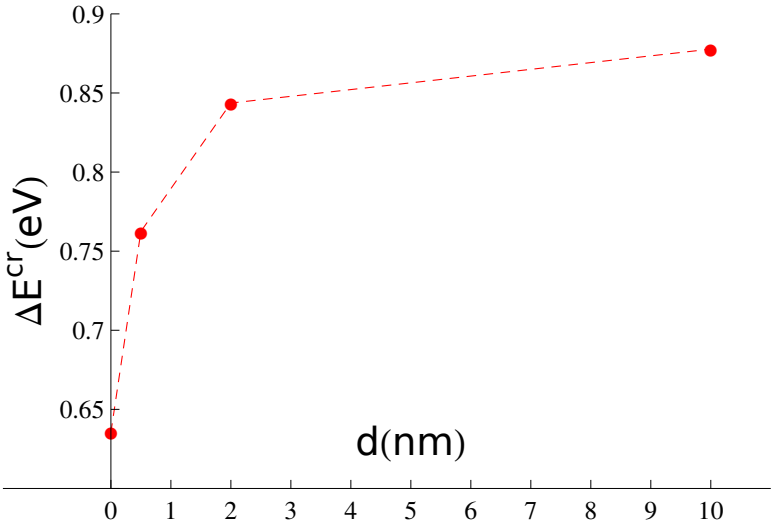

Figure 3.14: In case that the strain-dependent surface energy curve is modified, the nucleation energy barrier of forming pyramid as a function of its distance away from an existing pyramid.

We now investigate another issue concerning elongated islands. The Ge/Si(001) islands are sometimes found to elongate and to form the hut islands or nanowires[59, 43]. These hut islands and nanowires also form adjacently to each other, especially for the clustering nanowires which particularly locate parallel[43]. If the strain-dependent surface energy matters, the parallel huts or nanowires can be more strongly affected as they have a larger areas correlated.

Similarly as above, we consider two parallel hut islands and their elastic energy. We choose the height of hut islands to be 0.5 nm and a width of 5 nm. The length is set to be three times the width, i.e. 15 nm. Biaxial strain distributions with various distances

of 0 nm, 2 nm and 4 nm are shown in Figure 3.15. The energies with long-range effect are plotted as a function of distance in Figure 3.16.

We see that the surface energy increases while the elastic energy decreases with the distance. And as a whole, the energy of the system first increases with distance and then becomes almost constant at distance larger than 2 nm. The position of minimum energy locates at the 0 distance, which indicates that the two hut islands perform attractive interaction. More interestingly, the energy of attraction at the closest distance is about 0.2 eV, which is also larger than that in the case of two pyramids.

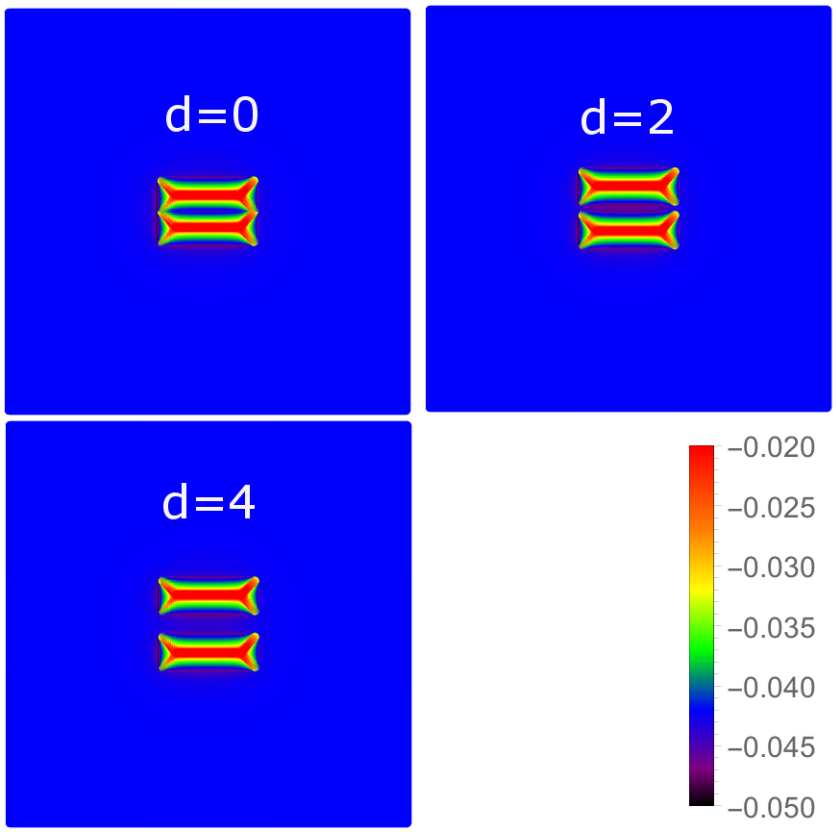

Figure 3.15: Biaxial strain distribution of two-hut system with different distance.

It is of great interest that the strain-dependence of surface energy may be applied to explain the clustering nanowires, which is recently found by Zhang[43].

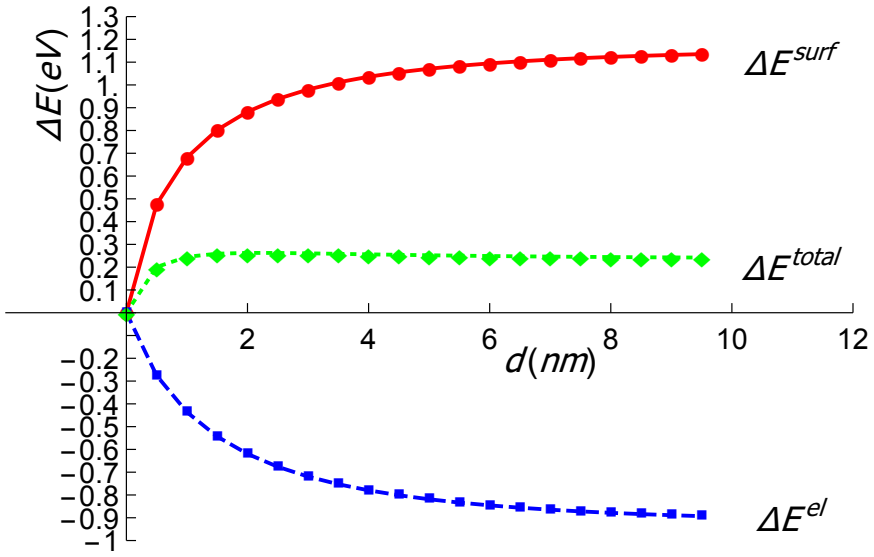

Figure 3.16: Surface energy (red), elastic energy (blue), and total energy (green) of two-hut system as a function of distance between them, which are all calibrated to 0 and 0 distance.

3.7 Discussions and conclusions

We start from the experimental observation of Ge/Si(001) sample to find the clustering of coherent islands. Then we take into account the strain-dependent surface energy, which has been ignored in the previous studies of island-island interaction. We found that when the islands are relatively small but larger than the theoretical critical volume of nucleation, islands can be driven to be attractive due to this strain-dependent surface energy. In practice, the clustering seems not a common phenomenon: some samples show strong clustering while some others do not. It may stem from the atomic-scale kinetics of nucleation controlled by the deposition flux and surface diffusion. From the basic energetic point of view, the strain-dependent surface energy can play an important role, ruling the distribution of islands.

Chapter 4

Self-organization of SiGe nanostructures on vicinal substrate

Contents

The formation of SiGe islands on vicinal substrate shows a completely different scenario compared to that on the nominal Si (001) substrate. The 3D islands on vicinal substrate are found to elongate perpendicularly to the miscut stpes. The spontaneous atomic steps on vicinal substrate indeed tune the elasticity of epilayer.

4.1 Background

The SiGe has been regarded as stereotype of semiconductor hetero-epitaxy. The methods of controllable growth are often tested within this system[28, 14, 60, 35, 61, 62]. The growth tuned by the steps on vicinal substrate is also widely investigated experimentally and theoretically, which has become an effective method in tailoring .

In the past decade, it was demonstrated that the use of 1D islands or nanowires could be of great interest for anisotropic electronic transport and 2D quantum confinement effects[63, 64, 65]. They are now easily integrated in 1D gate transistors and constitute an alternative way to make more efficient devices. However, one major hurdle to overcome towards their application in microelectronic devices is the presence of metallic catalysts present not only on the heads of the nanowires but also along their sides[66, 67]. For this reason several complex lithographic processes have been developed for the fabrication of planar NWs[68, 69], but their resolution is nowadays not sufficient to provide 2D quantum confinement effects as predicted by theory. Growth of self-organized homogeneous, dense and small planar 1D islands would be a simple and versatile method for the integration of nanowires into devices. A couple of studies demonstrated that the deposition of Ge on vicinal substrates could result in nanowires longer than $1\mu m$ under optimized conditions [70, 31, 52]. The periodic array of nanowires is controlled by a symmetry-breaking elasticity promoting the island elongation perpendicular to the step edges. Persichetti et al. [31] suggested that this 3D to 1D shape transformation results from anisotropic elastic interactions on vicinal substrates. A following fundamental question is how such 1D elongation proceeds and whether it is at variance with the usual ATG instability on nominal substrates.

In this chapter we examine the detailed effect of substrate misorientation on the formation of the SiGe islands resulting from the well-known ATG instability. We measure and analyze by x-ray diffraction (XRD) the strain relaxation and topography of SiGe islands on nominal Si(001) as well as vicinal substrate miscut 10ř off toward <110> direction. We compare the perpendicular strain and the planar strain state of the film deduced from Poisson dilatation , aiming to investigate the elasticity anisotropy. A significant reduction of the dilatation is found in SiGe films deposited on vicinal substrate. It is ascribed to the lateral elastic relaxation induced by the step edges. Anisotropic misfits are introduced in a continuum model to describe the strain anisotropy measured in experiments. We present here the results of the linear analysis within the continuum model. The crucial role of the strain anisotropy on the length over width

aspect ratio and on the evolution of the instability revealed by the theoretical model are in good agreement with the experimental results. In addition, we evidence the self-organization of nicely organized NWs in a high strain regime and the lateral size of NWs can be easily tuned by SiGe concentration, which agrees with the theoretical results as well.

4.2 Experiments

SiGe thin films were deposited by MBE on two different types of substrates, nominal Si(001) substrates or vicinal substrates micut 10° off Si(001) toward < 110 > direction. The substrates were chemically cleaned with the same method in chapter 2.

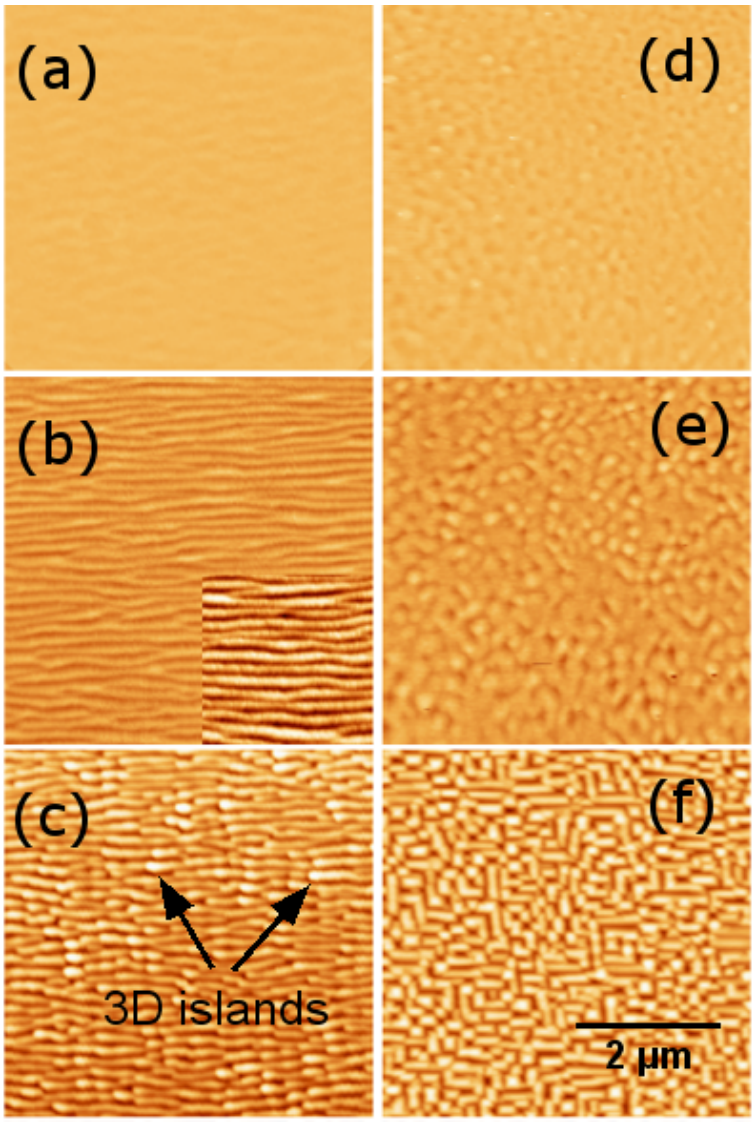

Figure 4.1: AFM images of SiGe layers with $x = 0.22$ and with thickness h_{SiGe} = (a)–(d) 5 nm, (b)-(e) 8 nm, (c)-(f) 10 nm. For clarity, the vertical scale of all the images is 20 nm.

We first deposited $Si_{0.78}Ge_{0.22}$ thin films with varied thickness from 5nm to 15nm on nominal Si(001) and vicinal 10°off substrate. Morphology of samples were observed with AFM. We followed the morphological evolution of the SiGe surface on both substrates by comparing the morphology with increasing thickness. After 5nm deposition, see Figure 4.1(a) and (d), the surfaces are flat with RMS roughness 0.1nm almost similar to those of clean Si substrates (i.e. in the range of the AFM noise). When the deposited thickness increases (h_{SiGe} = 8 nm) the instability develops and forms nice arrays of quasi 1D ripples on vicinal substrate while contrarily rectangular undulations emerge on nominal substrate. With continuing deposition to h_{SiGe} = 10 nm, 3D islands begin to emerge from the 1D nanowires, see Figure 4.1 (c), which then turn to round islands when h_{SiGe} = 15 nm, see Figure 4.4(a).

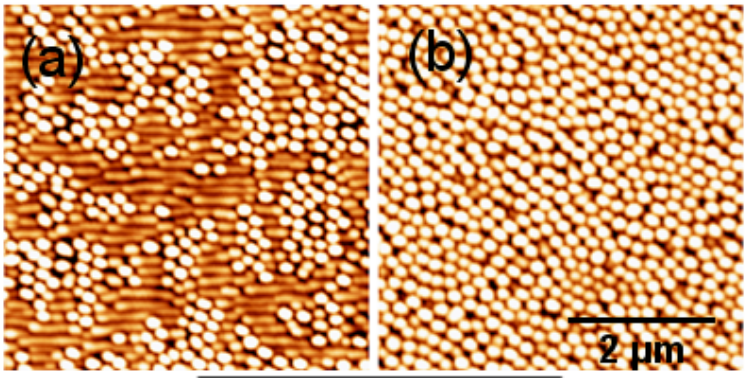

Figure 4.2: AFM images of 15 nm $Si_{0.78}Ge_{0.22}$ (a) on substrate 10° off, and on nominal (001) substrate.

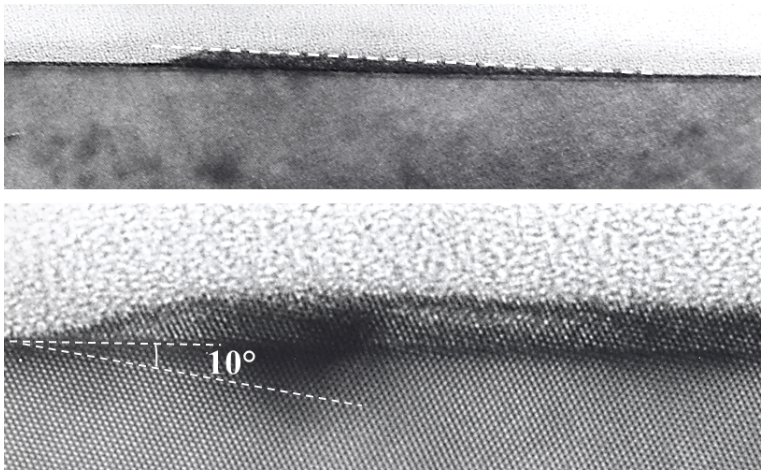

Figure 4.3: HRTEM images of cross section of elongated Ge islands on vicinal substrate

First it is important to determine the direction of elongation of the islands as compared to the step edges. We performed TEM cross-section images of the elongated islands on 10° off substrate (Figure 4.1(b)]. The images show that the islands lie over the

train of steps with their longitudinal length (called y) perpendicular to the step edges. The quasi 1D shape of the islands is also well visible on large scale TEM images, as shown in Figure 4.3.

To better understand and control the formation of 1D islands, we deposited SiGe films on substrates misoriented between 0.1° and 10°. When varying the Ge concentration, we find that on both substrates, the periodicity follows a power law evolution, independent of the misorientation. We then examine their morphological evolution with the misorientation (at constant Ge concentration). The results reported in Figure 4.4(a) show that the periodicity of the 1D array (perpendicular to the width of the nanowires) remains constant. These results are consistent with a misfit independent of the misorientation in this direction (called x) and identical to those on nominal substrate. At the opposite, in the y direction, the length of the nanowires is directly dependent on the misorientation (and consequently proportional to the density of steps). In Figure 4.5, we have reported the evolution along x and y of the correlation lengths with the misorientation. AFM images of the films for the different misorientations also clearly evidence the elongation of the islands Figure 4.4.

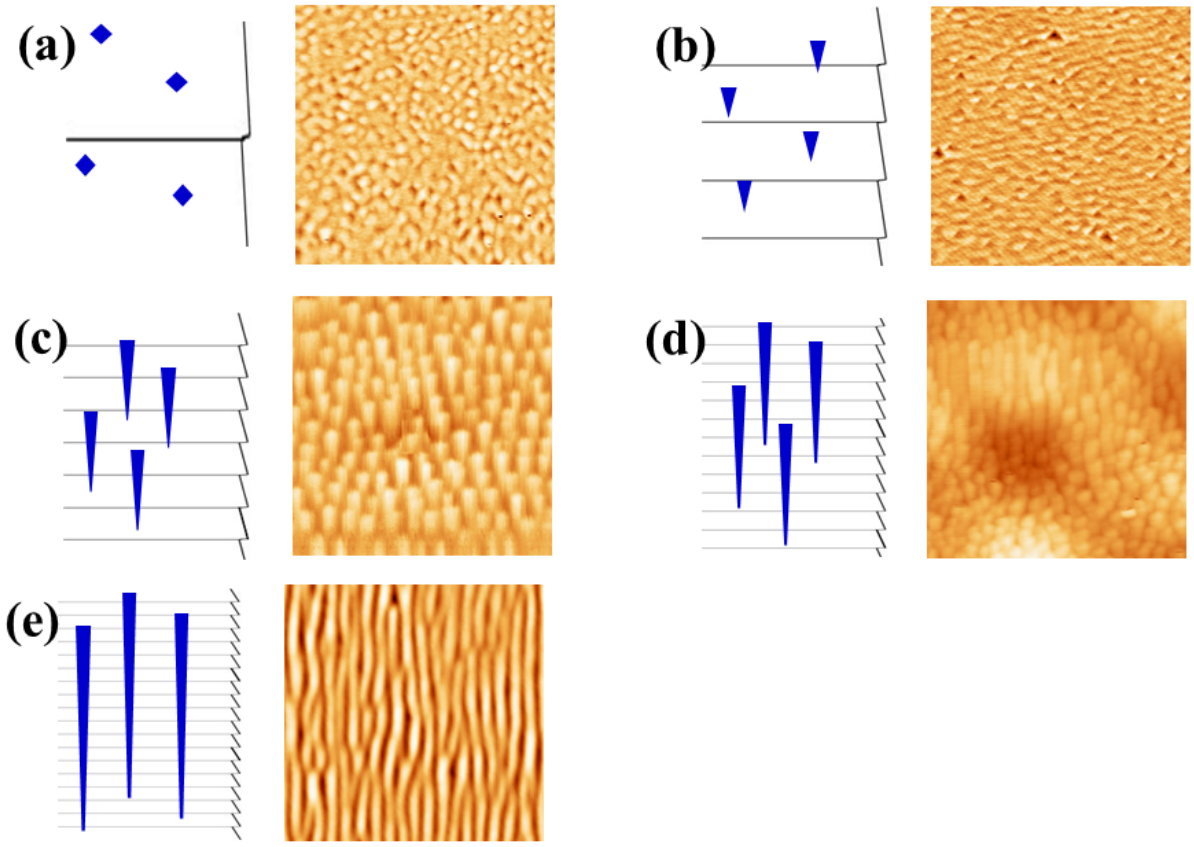

Figure 4.4: Evolutions of the correlation length in x and y directions (in the plane of the substrate) with the misorientation angle, (a) 0° (b) 4° (c) 6°(d) 8° (e) 10°, with schematic representation of substrate on the left and the corresponding AFM images on the right. The epilayer is $Si_{1-x}Ge_x$ with $x = 0.22$.

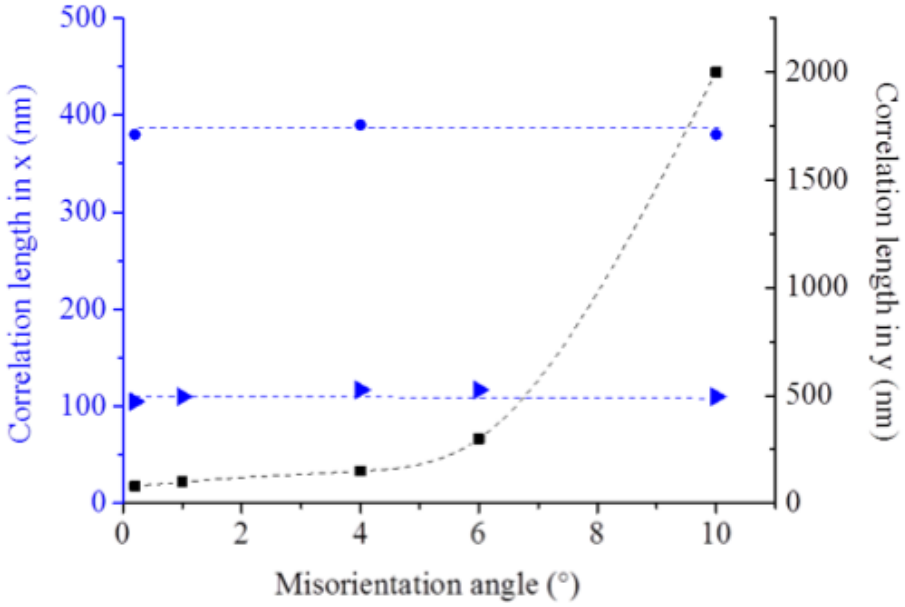

Figure 4.5: Correlation length in x direction and y direction as a function of misorientation angle, with x on the left in blue and y on the right in black.

An important feature of the SiGe films is the strain state both in the plane and perpendicular to the plane. We measured by x-ray diffraction the deformation perpendicular to the plane for the two flat layers in Figure 4.1 (a) and (d), respectively on nominal and 10° off substrates, as shown in Figure 4.6 and Figure 4.7. We focused on the flat films to rule out the effect of the morphological undulation on strain relaxation.

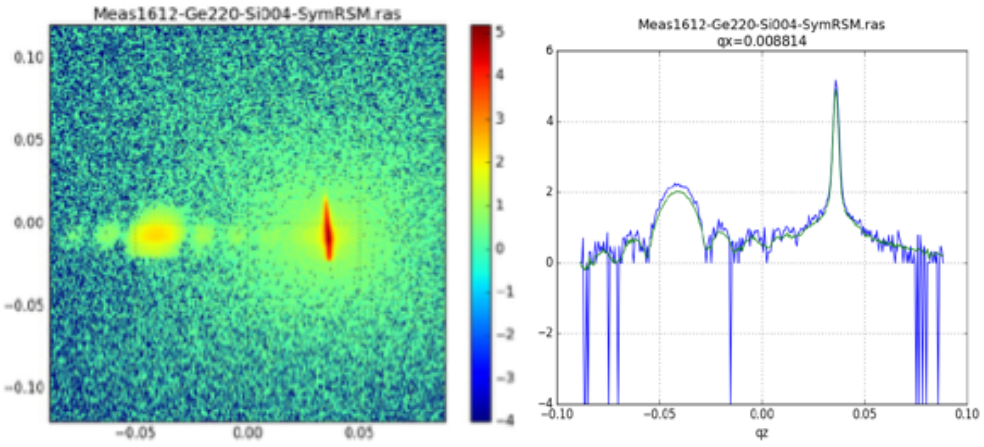

Figure 4.6: (a)Map around the (004) spot; (b) intensity profile at the maximum of intensity of the substrate.

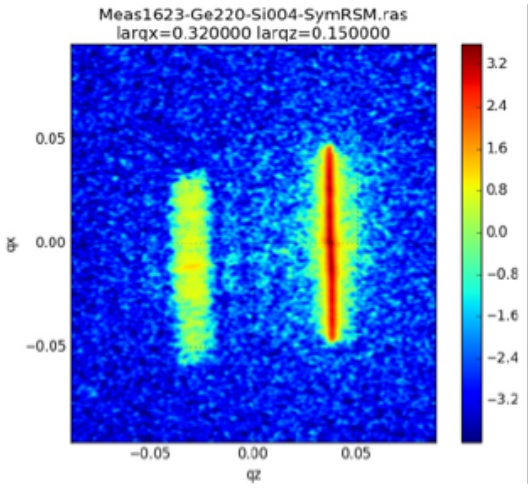

Figure 4.7: Filtered image of the (004) map on the vicinal 10ř off susbtrate.

For the nominal substrate, on the map intensity of the (004) spot, two peaks are observed, one very intense from bulk and another weaker from the layer (Figure 4.6(a)). Secondary oscillations are also observed between these two peaks in the qz direction, associated to the well-defined thickness of the layer. A cross-section profile at the maximum of intensity for the substrate averaged over 10 pixels (Figure 4.6(b)) shows that the distance between the two spots is $\delta q = 0.079\text{Å}^{-1}$ which gives a strain of $\delta q/q = 1.7\%$. From the position of the minima of the oscillations we could deduce $q_{ep} = 0.0014\text{Å}^{-1}$ which corresponds to a thickness 46 nm. This fits well with the 50nm SiGe nominal thickness deposited. The (004) map of the vicinal substrate is more noisy due to the presence of a large density of steps at the substrate/film interface, about 1 mono-atomic step every 10 Å measured on the (004) map. The distance between the two spots is $\delta q = 0.068\text{Å}^{-1}$ which gives a strain of $\delta q/q_{004} = 1.5\%$, lower than on nominal substrate. Even if the secondary oscillations are much less visible, again due to the steps. the same thickness (46nm) is measured on the filtered image. Considering the lower qz deformation on a vicinal substrate, we can deduce from Poisson dilatation, that the SiGe film is partially relaxed in the plane. Such partial relaxation can be ascribed to the train of mono-atomic steps which can relax the strain perpendicular to the step edges. We then examine theoretically an anisotropy of the lattice misfit in x and y.

4.3 ATG instability within anisotropic elasticity

The computation of the Poisson dilatation in the geometry Figure 4.8 is a straightforward generalization of its computation in symmetric films. We suppose linear isotropic elasticity where mechanical equilibrium enforce the Navier-Cauchy equations $\partial_j \sigma_{ij} = 0$ for $i, j = x, y, z$ where $\boldsymbol{\sigma}$ is the stress tensor[71]. We suppose that the film and substrate have the same Young's modulus and Poisson's ratio, that is quantitatively rea-

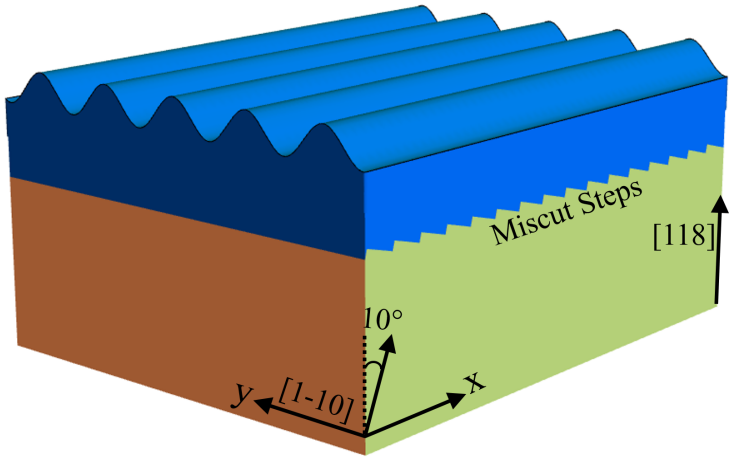

Figure 4.8: Geometry of the film/substrate system, epilayer on vicinal substrate.

sonable given the Si and Ge parameters, and that is qualitatively relevant given that differences in these parameters only renormalizes the elastic field, [72]. In coherent epitaxy where one assumes continuity of the displacement vector (and normal force) at the film/substrate interface, one has to work with a given reference state that we choose to be the substrate one in all the system. In this state,

$$e_{ij} = \frac{1}{2}(\partial_j u_i + \partial_i u_j) - \delta_{ij}(m_x\delta_{ix} + m_y\delta_{iy} + m_z\delta_{iz})\theta(z) \tag{4.1}$$

where the film lies in the $z \neq 0$ region and with the Heaviside function $\theta(z)$. Here, $m = (a_f - a_s)/a_s$ is the lattice mismatch between the film (f) and substrate (s) that depends a priori on the direction. Assuming a stress-free upper surface and a vanishing displacement deep inside the substrate, one finds the solution for a flat film

$$\boldsymbol{u}_0 = \frac{1}{1-\nu}\left[\nu\,(m_x + m_y) + (1-\nu)\,m_z\right] z\{0,0,1\}. \tag{4.2}$$

In the geometry under study, one finds the Poisson dilatation to be equivalent to a lattice parameter $a_\perp$ in the z direction given by

$$m_\perp = \frac{a_\perp - a^s}{a^s} = \frac{m + \nu\, m_x}{1-\nu}, \tag{4.3}$$

that reduces to $m_\perp^{sym} = m(1+\nu)/(1-\nu)$ when $m_x = m$. In the first experiment on a nominal substrate, one finds $m_\perp^{sym} = 0.01698$ that corresponds to a mean Ge concentration in the film $x = 0.229$ close to the expected deposited one. For this composition, the nominal misfit is $m = 0.0096$. In the second experiment, one finds $m_\perp = 0.0146$. This Poisson dilatation is related to an effective misfit in the x direction given by $m_x = 0.00345$, see Equation 4.3. Vicinality therefore introduces a strong relaxation of the equivalent misfit strain in the direction perpendicular to the steps that is about one third of the mismatch for the nominal substrate. The asymmetry in the x and y effective strain results in different relaxation of a surface corrugation in these directions.

Given the flat film solution $\boldsymbol{u}_0$, we compute the displacement field associated with a free surface $z = h(\boldsymbol{r})$ where $\boldsymbol{r} = \{x, y\}$. We solve for the Navier-Cauchy equations in Fourier space (with the convention $\hat{h}(\boldsymbol{k}) = \frac{1}{(2\pi)^2}\int d\boldsymbol{r}\, e^{i\boldsymbol{k}\cdot\boldsymbol{r}} h(\boldsymbol{r})$) assuming that the surface $h(x, y)$ displays small slope around its mean value h_0. The solution may be decomposed as $\boldsymbol{u} = \boldsymbol{u}_0 + \boldsymbol{u}_1$ with

$$\boldsymbol{u}_{1,x} = i\hat{h}_1 \frac{k_x e^{k(z-h_0)}}{k^3(1-\nu)} \times \Big\{ -kh_0 \Big[k_x^2(m_x + m_y\nu) + k_y^2(m_x\nu + m_y)\Big] + k_x^2(m_x + m_y\nu)(kz - 2\nu + 2) + k_y^2 \Big[m_x\Big(\nu kz - 2\nu^2 + 2\Big) + m_y kz\Big]\Big\}, \quad \textbf{(4.4)}$$

with a symmetric solution for $\boldsymbol{u}_{1,y}$ where x and y are interchanged, while

$$\boldsymbol{u}_{1,z} = \hat{h}_1 \frac{e^{k(z-h_0)}}{k^2(1-\nu)} \times \Big\{ kh_0 \Big[k_x^2(m_x + m_y\nu) + k_y^2(m_x\nu + m_y)\Big] - (kz + 2\nu - 1)\Big[k_x^2(m_x + m_y\nu) + k_y^2(m_x\nu + m_y)\Big]\Big\}, \quad \textbf{(4.5)}$$

with $k = \sqrt{k_x^2 + k_y^2}$. The elastic energy density on the surface, $\mu^{el} = \frac{1}{2}\sigma_{ij}e_{ij}[z = h(\boldsymbol{r})]$, associated with this solution is given at lowest order by $\mu^{el} = \mu_0^{el} + \mu_1^{el}$ with

$$\mu_0^{el} = \mathscr{E}_0\Big(\eta^2 + 2\eta\nu + 1\Big) / \big[2(1+\nu)\big] \quad \textbf{(4.6)}$$

where $\mathscr{E}_0 = Y m_y^2/(1-\nu)$ and $\eta = m_x/m_y$. At linear order in the surface slope, it reads

$$\hat{\mu}_1^{el} = -2(1+\nu)c_3\,\mathscr{E}_0\,k\,\hat{h}_1 \quad \textbf{(4.7)}$$

with

$$c_3 = \frac{1}{(1+\nu)^2 k^4}\Big[k_x^4(\eta+\nu)^2 + k_y^4(1+\eta\nu)^2 + k_x^2k_y^2(1+\nu)\Big(\eta^2 + 2\eta\nu + 1\Big)\Big]. \quad \textbf{(4.8)}$$

4.4 Evolution equation

As a first approximation, we describe the instability at work in such hetero-epitaxial systems in a full continuum framework. We thence neglect the inhomogeneity and asymmetry introduced by the steps in the diffusion process, together with attachment-detachment issues at the steps. As a consequence, we rule out the step-bunching or step-meandering instabilities [71, 73] that are known to yield nano-structures that can not rationalize the instability described above, that grows perpendicular to the steps. However, as explained above, vicinality rules the effective strain state that drives the morphological evolution. Surface diffusion is thence described within the continuum mass conservation equation $\partial h/\partial t = D\sqrt{1+|\boldsymbol{\nabla} h|^2}\boldsymbol{\Delta}_S\mu$, with some diffusion coefficient D and the surface Laplacian $\boldsymbol{\Delta}_S$. The latter equation follows from the hypothesis that surface currents are proportional to gradients of the surface chemical potential μ [74,

57]. The latter potential $\mu = \mu^s + \mu^{el}$ includes both a capillary $\mu^s = -\gamma\Delta_S h$ at linear order in the surface slope with the surface energy γ, and the elastic contribution given above. We consider the space scale $l_0 = \gamma/[2(1+\nu)\mathscr{E}_0]$ and time scale $t_0 = l_0^4/(D\gamma)$. In units of l_0 and t_0, the evolution equation reads at linear order

$$\frac{\partial \hat{h}_1}{\partial t} = \left(c_3\, k^3 - k^4\right)\hat{h}_1\,, \tag{4.9}$$

neglecting the wetting interactions that are not relevant here for thick films in the instability regime before island growth.

4.5 Numerical Results

We consider typical values for a $Si_{1-x}Ge_x$ film on Si(001), see e.g.[49]. The growth temperature is 550 °C and the composition is 0.229 as found above. The evolution runs during deposition that lasts 30 minutes. The initial surface is considered as a white noise with an amplitude of 0.3 nm. The numerical integration of Equation 4.9 up to an amplitude of the surface roughness of 1 nm is plotted in Figure 4.9.

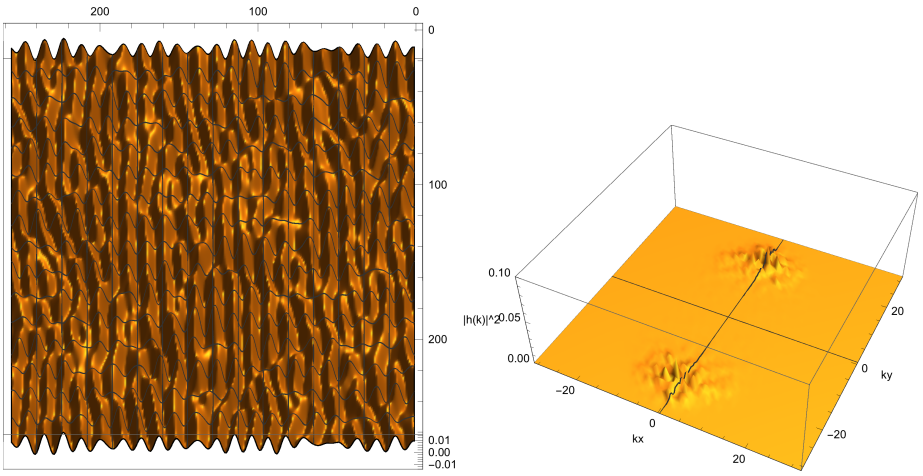

Figure 4.9: (left) Anisotropic ATG instability with an asymmetric strain in the x and y direction corresponding to the strain asymmetry found experimentally on a vicinal surface corresponding to a time when the peak to peak amplitude of instability is 1 nm; (right) Spectrum of this surface.

4.6 Dynamic Evolution with Wetting effect and Surface Anisotropy

For a thinner epilayer, its dynamic evolution can also be tuned by the wetting effect. In addition, at the end of evolution, facets will emerge and surface energy anisotropy will

also become important to enter into the dynamics. Here we perform an experiment to investigate morphological evolution of dynamics in the regime of ATG instability on vicinal substrate 10 ° off toward the [110] direction. $Si_{0.7}Ge_{0.3}$ with thickness of 5 nm is deposited on the vicinal substrate with a Si buffer layer. The as-grown sample

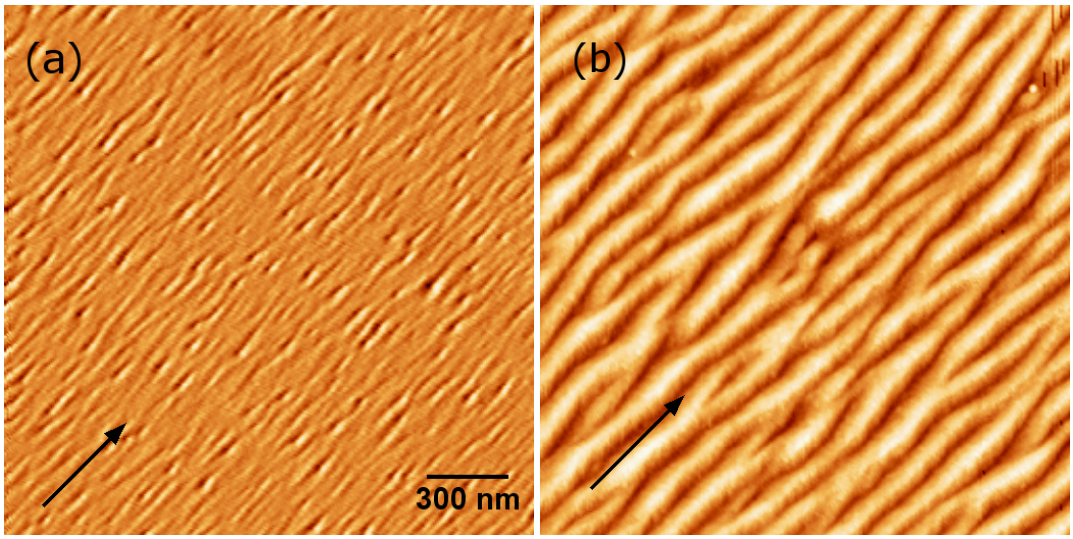

Figure 4.10: 5 nm $Si_{0.7}Ge_{0.3}$ deposited on 10° substrate at 500 °C , (left) As-grown sample and (right) after post-growth 18-hour annealing at 500 °C , [110] direction is indicated by black arrow and the images size is $2 \times 2\mu m^2$

shows some undulations with small amplitude, which shows some tendency to elongate along the [110] direction. The trend becomes more obvious during the annealing as the epilayer continues to evolve. Well-aligned nanowires along [110] direction after 18-h annealing at 550 °C , see Figure 4.10(b).

These 1D planar nanowires then begin to break up, which is evidenced from Figure 4.11(a), for which the annealing of the sample is extended to 72 h. For convenience, we increased the annealing temperature to 575 °C and found that all the nanowires break into isolated (105)-faceted 3D islands, see Figure 4.11(b).

During the long-term annealing of thin epilayer, the wetting effect and anisotropic surface energy can be an important role during the morphological evolution. These two effects can also be integrated into the continuum model as shown by Aqua et al.[49, 28], which is in the plan of future works.

Furthermore, in the regime of ATG instability, the size of 1D nanowires is indeed determined by the wavelength of ATG instability, following the relation as Equation 1.11 in chapter 1. Thence the size of nanowires can be conveniently tuned via varying the composition of $Si_{1-x}Ge_x$. We deposited 2.5 nm $Si_{0.5}Ge_{0.5}$ at 500 °C on the 10 ° off substrate and get similar planar nanowires but with much smaller size, about 30 nm. As for higher strained epilayer, the morphology evolves more rapidly, the as-grown sample already show this similar nanowires, see Figure 4.12.

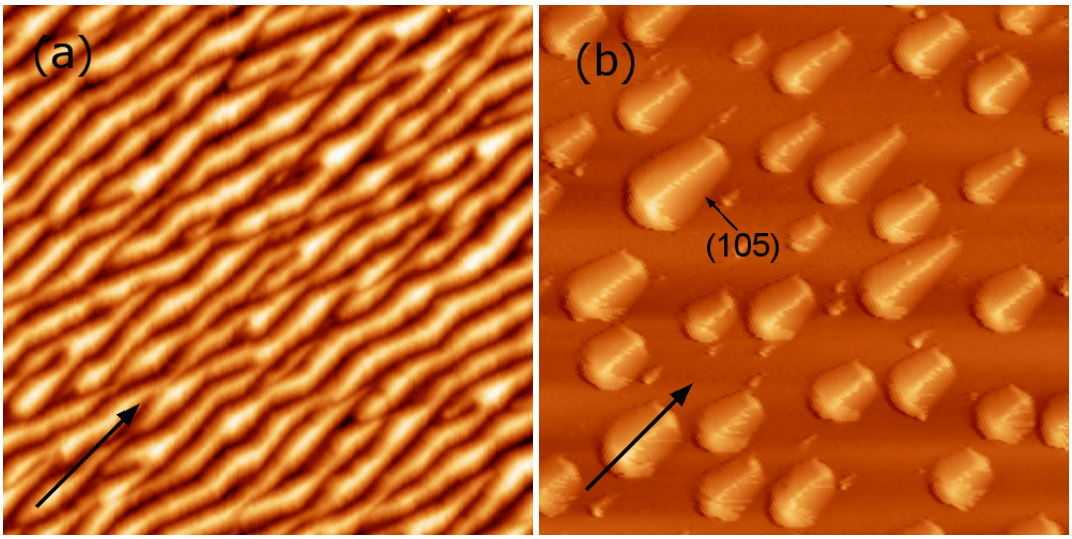

Figure 4.11: 5 nm $Si_{0.7}Ge_{0.3}$ deposited on 10° substrate at 500 °C , (a) after post-growth 72-hour annealing at 500 °C . and (b) after post-growth 72-hour annealing at 575 °C ,[110] direction is indicated by black arrow.

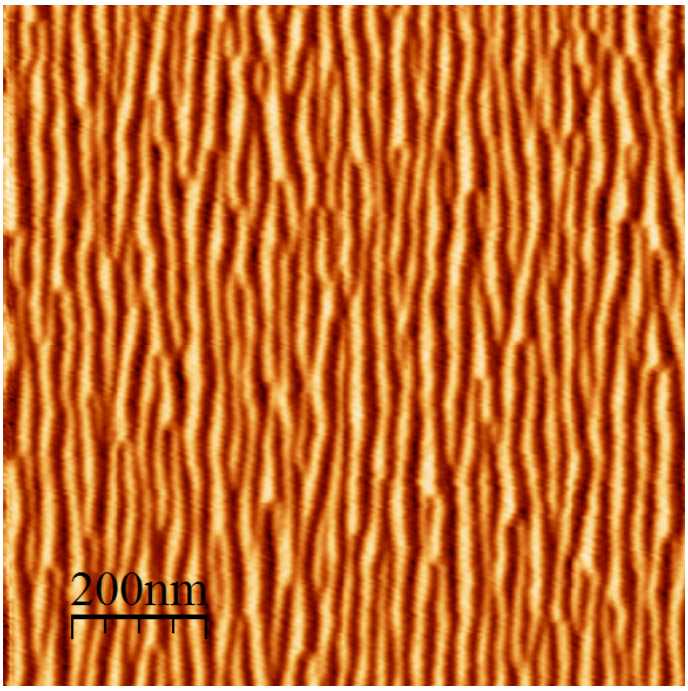

Figure 4.12: AFM image of as-grown sample of 2.5 nm $Si_{0.5}Ge_{0.5}$ deposited on the 10 ° off substrate

4.7 Conclusion

We demonstrate a simple route to fabricate high-density arrays of SiGe planar nanowires using anisotropic elastic strain relaxation induced self-assembled morphology of SiGe ATG instability. The dimensions and lateral density of the NWs array are directly related

by the anisotropy of elastic relaxation (lateral over longitudinal ratio) and by the epitaxial strain respectively. The substrate misorientation i.e. the density of steps is used to create the anisotropy of strain relaxation. The theoretical assessment of the islands elongation when considering an anisotropy of misfit in the plane deduced from the reduction of the deformation measured by x-ray diffraction, is in quantitative agreement with the morphological evolution measured experimentally.

The dynamic evolution of of epilayer tuned by the misorientation steps is investigated during long-term annealing. The flat epilayer first turns to dense array of NWs, and subsequently break up into isolated islands, which are also (105)-faceted as other coherent islands in SiGe system. In addition, we demonstrated that the size of NWs can be conveniently tuned by varying the composition of $Si_{1-x}Ge_x$.

Chapter 5

New strategy to prevent the development of the instability

Contents

In this chapter, a method to fabricate fully-strained SiGe thin layer via the condensation of dilute SiGe is investigated. On the contrary to the common epitaxial growth, the condensation of SiGe allows to produce a strained thin layer without introducing dislocations and the 3D islands which always appear above critical wetting layer during the direct epitaxial growth are significantly inhibited. This fully-strained layer has great potentials in the applications of FD-SOI technology which is regarded as main building block of the next-generation CMOS transistor.

5.1 FD-SOI technology and SiGe condensation process

The development of next-generation CMOS is significantly limited by the current leakage while continuing the miniature of transistor node scale. To resolve this issue and revive Moore's law, CMOS block fabricated on SOI substrate, which could hinder the current leakage via the buried SiO_2 insulator, is regarded as one of the most promising solutions. In addition, the integration of SiGe strained layer onto SOI, which eventually acts as the channel material in a SOI-based CMOS, is a of great significance to enhance the charge carriers mobility in CMOS as this various strain induced by lattice mismatch could achieve the mobility enhancement required in each transistor and raise the drive current of the device.

Many of the expected advances will depend on further steps of the CMOS process on SOI, in particular the epitaxial integration of defect-free Si and SiGe ultrathin layers[75, 76]. SGOI is commonly produced by a Ge condensation technique that a dilute (typically $Si_{0.9}Ge_{0.1}$ layer) is first epitaxially grown on SOI and followed by an oxidation step to produce a Ge-enriched layer which intermixes with the underlying Si layer to form a quasi-homogeneous SiGe layer, see Figure 5.1. The mechanism of condensation stems from the much lower formation energy of SiO_2 than that of GeO_2,(-8.2 eV and -4.7 eV respectively), which leads to the preferential oxidation of Si in SiGe alloy[77]. The strain state in the structure of SOI with epitaxial SiGe layer atop is also

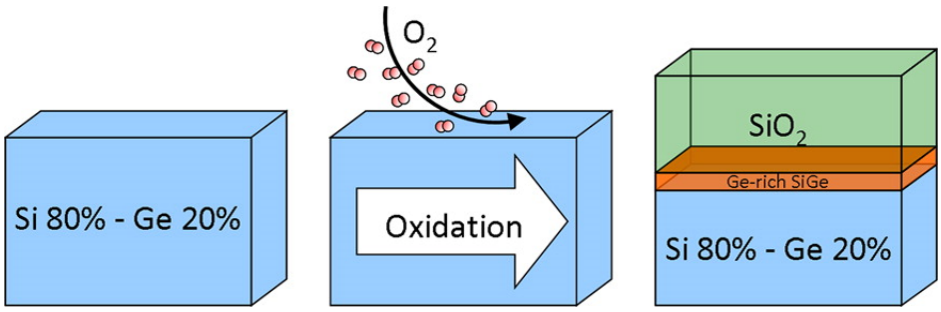

Figure 5.1: Oxidation of SiGe and formation of a Ge-rich layer by condensation of the germanium at the interface[78].

under extensive investigation. The partitioning of strain between the epitaxial layer

and its substrate causes a reduction of the overall strain energy. Despite extensive studies, the major issue whether SOI behaves as a compliant substrate is still under debate. The first problem is that, in several studies, the thickness of the compliant top Si SOI layers was not thin enough to avoid dislocations in the epitaxial layers according to our model. The second problem comes from the Si/SiO_2 interface which is not fully slippery at temperatures of growth and start to glide only at very high temperatures in conjunction with the formation of misfit dislocations.

Moreover, several studies aimed to investigete the compositional evolution of SiGe condensation process commonly reported that at high oxidation temperature SiGe interdiffusion is dominant resulting a SiGe layer with smooth but gradually diffuse Ge concentration profile. Such a layer can be easily homogenized by a nonoxidizing high-temperature annealing and forms a dilute SiGe layer on top of the oxide. In these conditions, the process of SiGe interdiffusion is strong enough to homogenize all the Ge accumulated beneath the oxidation front across the SiGe/Si structure. The composition of these homogeneous diluted SiGe layers stems from the intermixing between the nominal SiGe epitaxial layer and the SOI pseudosubstrate without any visible loss of Ge during oxidation.

In contrast, at low oxidation temperature, the Ge pile-up mechanism is dominant and produces a germanium-rich layer (GRL) with a surprisingly constant Ge concentration, $x = 0.5$, regardless of the experimental conditions (i.e., initial SiGe composition, epitaxial stress, oxidation duration). The very abrupt GRL/SOI interface and the constant composition of the GRL($Si_{0.5}Ge_{0.5}$) over a range of 700-850 °C oxidation temperatures results from the dramatic decrease of germanium diffusion in Si compared to $Si_{0.5}Ge_{0.5}$. In these conditions, the final GRL concentration is enriched compared to that of the initial $Si_{0.8}Ge_{0.2}$ and reaches $Si_{0.5}Ge_{0.5}$. The enriched layers are found to be fully strained, perfectly flat, and free of extended defects.

The formation kinetics of $Si_{0.5}Ge_{0.5}$ during the oxidation process has been systematically studied, In this chapter, in order to understand the role played by SOI substrate on the strain and morphology of GRL, we compare the morphological and structural features of SiGe thinlayers fabricated by direct epitaxial growth and rationalize the formation mechanism of this $Si_{0.5}Ge_{0.5}$ layer.

5.2 Experiments

In this study we focus on the comparison of three samples: Sample A was obtained by the condensation process, i.e., epitaxy of a 30 nm thick $Si_{0.8}Ge_{0.2}$ layer on SOI followed by rapid thermal oxidation (RTO) to obtain 8 nm of $Si_{0.5}Ge_{0.5}$ on the SOI. Sample B was obtained by direct MBE of 8 nm of $Si_{0.5}Ge_{0.5}$ on SOI, and sample C was obtained by direct MBE of 8nm ofSi $Si_{0.5}Ge_{0.5}$ but on nominal (001) Si substrate. A schematic representation of the three structures is given in Figure 5.2

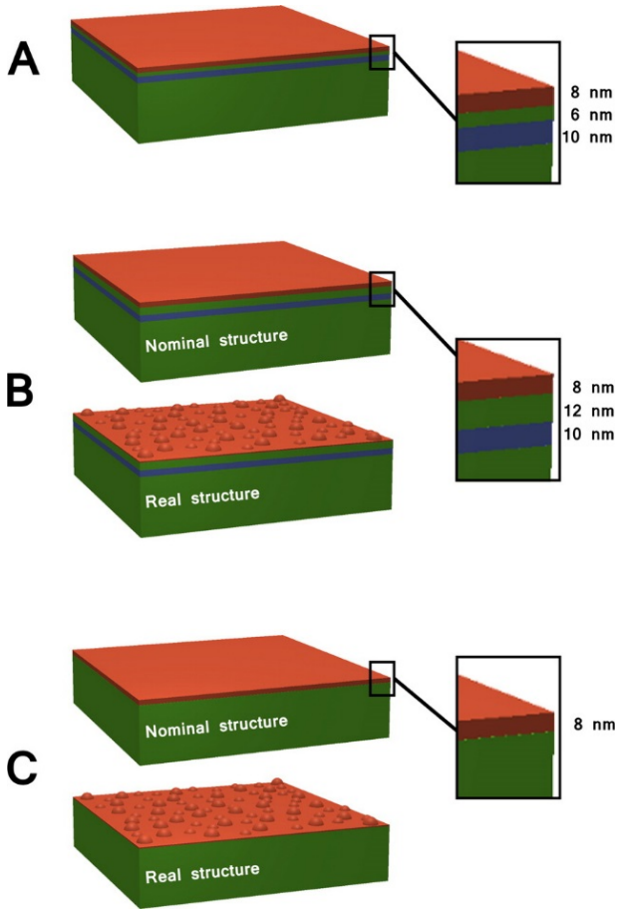

Figure 5.2: Schematic representation of the three structures. Sample A is a 8 nm thick $Si_{0.5}Ge_{0.5}$ layer on a 6 nm thick SOI (10 nm) obtained by oxidation of a thicker (30 nm) initial $Si_{0.8}Ge_{0.2}$ layer. Sample B is a 8 nm thick $Si_{0.5}Ge_{0.5}$ layer on a 12 nm SOI, and sample C is a 8 nm thick $Si_{0.5}Ge_{0.5}$ layer on a bulk Si substrate. Samples B and C were both obtained by direct MBE deposition; therefore, the $Si_{0.5}Ge_{0.5}$ layer is not flat and island formation occurred

5.2.1 Sample preparation

The specific Ge-rich layers have been obtained via three different processes either on a SOI substrate or a Si(001) nominal substrate. The commercial SOI substrate was fabricated using the SmartCut process which consists of a top 12 nm ultrathin Si layer on 25 nm SiO_2. Then, $Si_{1-x}Ge_x$ layers of different thicknesses and compositions of $x = 0.2$ or $x = 0.5$, were epitaxially grown by molecular beam epitaxy on the cleaned SOI substrates.

Surface preparation for epitaxy consists of ex-situ and in-situ cleaning. Ex-situ, the silicon cleaning follows a modified Shiraki recipe: (i) 10 min in HNO_3(65%) heated at 70 °C , (ii) 1 min in deionized water, and (iii) 30s in HF (5%). The samples are introduced into an ultrahigh-vacuum MBE Riber MBE32 growth chamber with a base pressure below 10^{-10} Torr. To avoid the dewetting instability of SOI substrate, in-situ cleaning process via high-temperature heating cannot be applied. Instead, we finish the ex-situ cleaning by HF to leave the surface passivated by H^+ , and we introduce the

sample immediately in the chamber. Then, we anneal it at 550 °C in growth chamber for 30 min to in-situ dettach H^+. SiGe layers are deposited at 450 °C . Low-temperature oxidation was carried out at 750 °C for 8 h by steps of 30 min in accordance with the RTO furnace JIPELEC technical specifications. These conditions were extracted from previous experiments using a similar condensation process, which provided accurate data on the experimental RTO conditions to obtain a single $Si_{0.5}Ge_{0.5}$ layer on SOI. To prevent SiGe/Si intermixing, the RTO temperature was kept relatively low compared to conventional temperatures, typically reaching 1100 °C . A complete study on the formation of this $Si_{0.5}Ge_{0.5}$ layer has already been published. The two-step process with oxidation refers to the condensation process (sample A), while the direct deposition of $Si_{0.5}Ge_{0.5}$ refers to the epitaxy processes (samples B and C).

5.2.2 Characterization

Cross-sectional samples were prepared using a dual-beam FIB Helios 600 nanolab or tripod polishing followed by PIPS (Ar+) thinning. Transmission electron microscopy (TEM) was done using a FEI Tecnai G2 and a FEI Titan 80-300 with Cs-corrector in TEM and scanning transmission electron microscopy (STEM) modes. Energy-dispersive spectrometry (EDS) analysis and line profiles are carried out with the FEI Tecnai G2 using a probe size of approximately 3 nm. The k factors of Si, Ge, and O were measured on reference samples and allowed the determination of absolute concentrations. Geometric phase analysis (GPA) was done using Digitalmicrograph software on high-resolution TEM (HRTEM) and high-resolution STEM (HRSTEM) images.

X-ray measurements were performed using a nanofocused X-ray beam at beamline ID01 of the European Synchrotron Facility in Grenoble (France). The nanobeam was focused down to a 150 × 300 nm^2 (vertical × horizontal) spot size using a Fresnel zone-plate (FZP) of 270 μm diameter and 80 nm outermost zone width. The nanodiffraction experiments were carried out at a beam energy of 8 keV (wavelength, λ, of 1.55 Å). The diffracted beam was recorded with a two-dimensional (2D) MAXIPIX photon-counting detector, characterized by 516 × 516 pixels of 55 μm pixel size. The sample was mounted on a fast xyz scanning piezoelectric stage, with a lateral stroke of 100 μm and a resolution of 2 nm.

5.3 Results and Analysis

5.3.1 Composition confirmation

First the composition of the SiGe layers obtained by the three different processes was measured by semiquantitative EDS. We show here the in-depth line profile of Si, Ge, and O only for sample A. A similar composition close to $x = 0.50 \pm 0.05$ was found in the three samples. In the present case (sample A, condensation process), the $Si_{0.5}Ge_{0.5}$

rests on top of a 6 nm thin layer of pure Si remaining from the initial UT-SOI, with an abrupt interface between the two layers ($Si_{0.5}Ge_{0.5}$/Si).

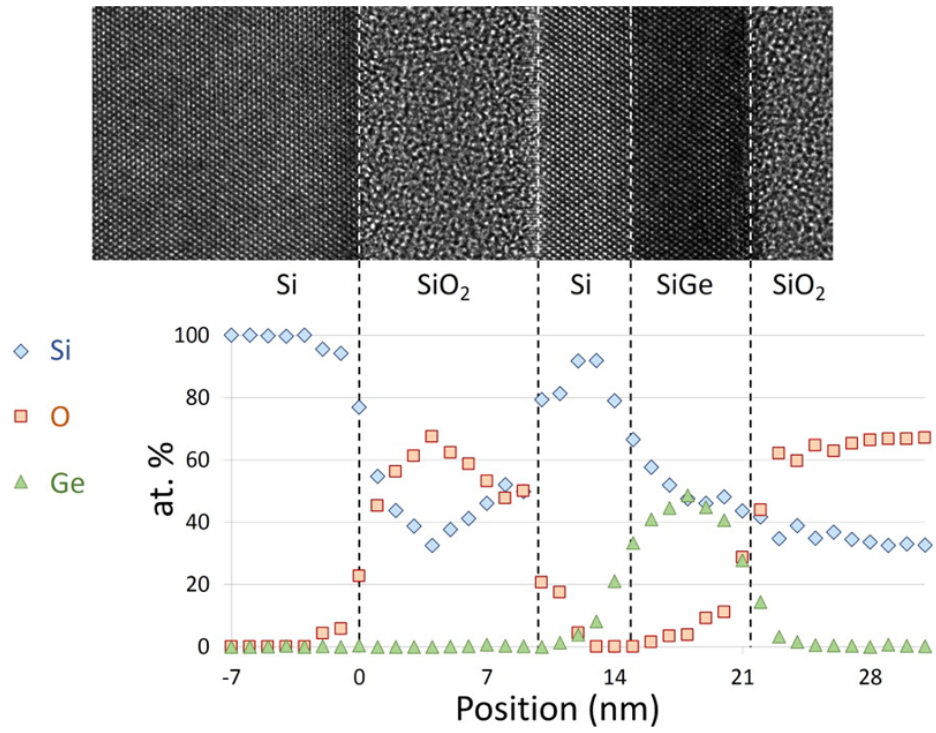

Figure 5.3: TEM EDS profile of sample A and the corresponding HRTEM image identical to the one in Figure 3.

Figure 5.4 shows cross-sectional TEM images of the three structures. Samples B and C both exhibit island and/or dislocations in the $Si_{0.5}Ge_{0.5}$ layer. Defects are highlighted in the case of sample B in the higher-magnification image shown in the inset. On a semi-infinite silicon substrate such as sample C, the critical thickness for island nucleation (h_{3D}) is evaluated in our experimental conditions to be 2 nm (see Results) and is slightly larger for dislocation nucleation (h_c). Both are much lower than the deposited thickness. The results are then consistent with previous studies, and the morphologies and structures are explained by the biaxial strain relaxation.

On the two substrates, the SiGe epitaxial layers evolve similarly; therefore, an initial observation is that in spite of the small thickness (12 nm) of the Si top layer, the relative compliance of UT-SOI is not sufficient to avoid three-dimensional (3D) islands or dislocations in these experiments. We then investigated more precisely the 2D-3D growth transition for $Si_{0.5}Ge_{0.5}$ deposition. In these experiments, the growth temperature was maintained at a lower value, typically 550 °C , to avoid the nucleation of dislocations. As indicated by AFM images of three $Si_{0.5}Ge_{0.5}$ layers with $h = 2, 2.3$, and 2.5 nm, the 2D-3D transition occurs at a critical thickness of approximately 2 nm (Figure 4). One can easily observe the increasing density of small islands from $h = 2.3$ and $h = 2.5$ nm, while only prepyramids are observed at $h = 2$ nm. It is the nucleation of these prepyramids which indicates the onset of the 2D-3D growth transition.

In contrast, neither dislocations nor islands could be observed on sample A obtained in similar experimental conditions via the two-step process. An even more intriguing result is that while critical thicknesses of both island nucleation and dislocation nucleation are largely overcome, the $Si_{0.5}Ge_{0.5}$ layers about 8 nm thick remain totally flat and free of extended defects.

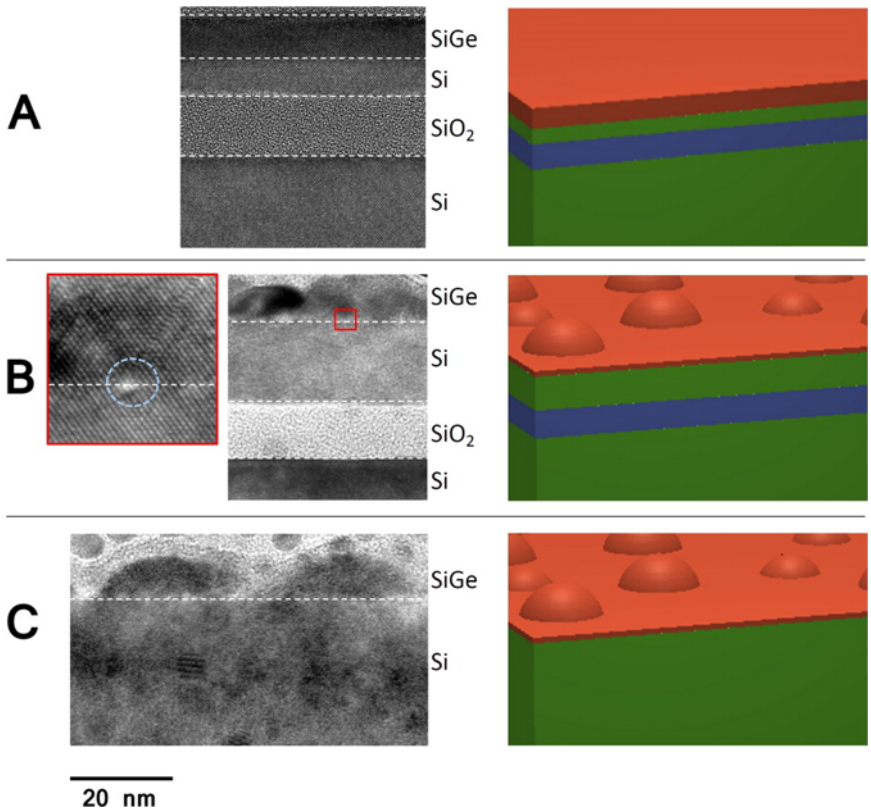

Figure 5.4: High-resolution TEM cross-sectional images of the three structures A, B, and C. For each structure, the corresponding schematic representation similar to Figure 1 is presented on the right. For sample B, the inset shows a higher-magnification TEM image to highlight the presence of defects in the crystal.

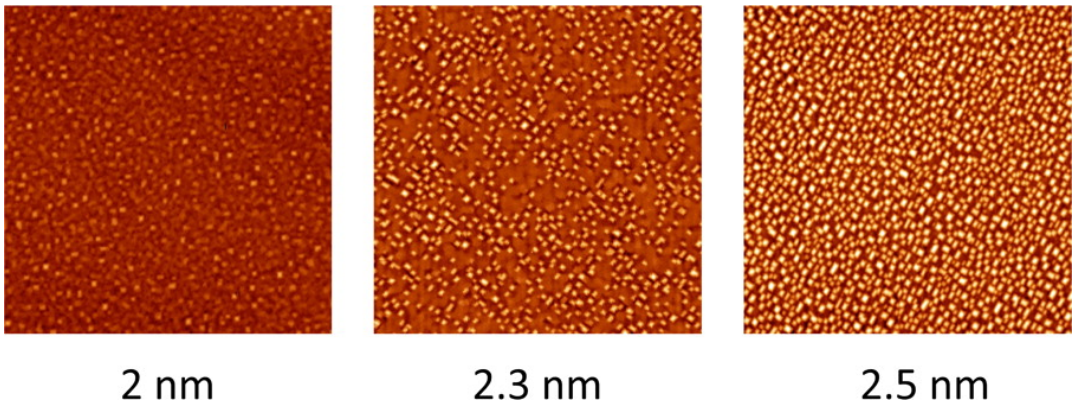

Figure 5.5: AFM images of a 2 × 2 μm^2 area of the surface of 2, 2.3, or 2.5 nm thick$Si_{0.5}Ge_{0.5}$ layers which were epitaxially deposited on silicon at 550 °C .

To address this question we undertook a detailed study of the strain in the different samples using geometric phase analysis on TEM images 24 and X-ray diffraction. When applied to the very flat and uniform layer of sample A, the GPA method provided accurate measurements while it was made difficult by the presence of islands and dislocations that relieve inhomogeneously the strain in samples B and C. Figure.5 shows GPA analysis of a TEM image of sample A. The HRTEM image analyzed is shown in Figure.5a. Figure.5 b shows the corresponding GPA image of the deformation along the in-plane x axis. No variation of the lattice parameter could be observed between the silicon substrate, the UT-SOI, and the $Si_{0.5}Ge_{0.5}$ layer.

This accounts for a fully biaxially strained $Si_{0.5}Ge_{0.5}$/UT-SOI, having a lattice parameter aligned to that of the relaxed Si and without any strain sharing between the Si and SiGe membranes. Along the out-of-the-plane y axis, the SiGe lattice parameter is distorted following Poisson's law. We name a(x) the lattice parameter of a fully relaxed $Si_{1-x}Ge_x$. When the SiGe is epitaxially grown on silicon, the lattice is deformed and we name b the in-plane lattice parameter (equal to the silicon lattice parameter aSi) and c(x) the out-of-the-plane lattice parameter resulting from the tetrahedral deformation dictated by Poisson's law. The lattice deformation under biaxial strain is given by

$$a(x) = (c(x) + bP)/(1+P) \tag{5.1}$$

with $p = \frac{2\nu}{1-\nu}$, where ν is Poisson's ratio. The lattice parameter of relaxed $Si_{1-x}Ge_x$ can be calculated from a_{Si} and a_{Ge} (lattice parameters of pure relaxed Si and pure relaxed Ge, respectively)[79]:

$$a(x) = 0.02733x^2 + 0.1992x + 5.431 \tag{5.2}$$

On the GPA image representing the deformation along the out-of-plane y axis, seeFigure 5.6 c, it is clear that the lattice parameter in the $Si_{0.5}Ge_{0.5}$ layer is higher than the one in Si. As evidenced on the plot, seeFigure 5.6 d, the difference is approximately 3%. Because the composition of this layer is known (50% Ge) and thanks to **??**, we can deduce a corresponding 3.4% out-of-plane expected expansion, resulting from the biaxial in-plane compressive strain between the $Si_{0.5}Ge_{0.5}$ and Si layers. The slight difference with the GPA measurements (4%) is attributed to the imprecision of this technique in the determination of stress and strain values.

An important issue with GPA measurements is also the very small size of the surface measured which does not give a statistical representation of the full sample. More global and accurate information can be provided by X-ray diffraction experiments. Figure Figure 5.7a-c shows reciprocal space maps (RSMs) around 004 Si and SiGe Bragg peaks on the three samples (respectively A, B and C) and a RSM around (115) Si and SiGe Bragg peaks on the sample A (Figure 5.7 a, right panel). The intensity attributed to the SiGe layer has been circled in black in all RSMs, and the expected Qz positions for the Si and pseudomorphic $Si_{0.5}Ge_{0.5}$ layer on Si are indicated by horizontal dashed lines. RSMs around (004) reflections give information about the out-of-plane lattice

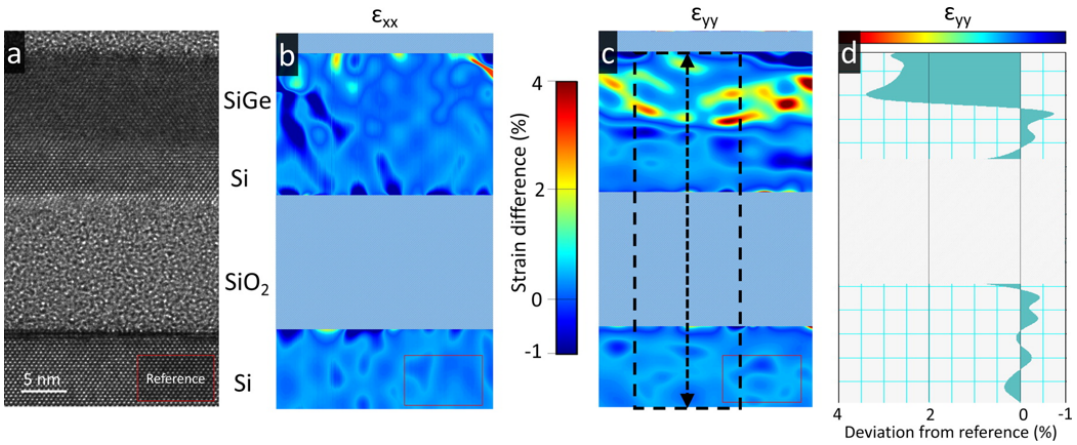

Figure 5.6: TEM cross-sectional image of sample A (a) and geometric phase analysis of the image along the x (horizontal) axis (b) and y (vertical) axis (c). GPA is irrelevant in the SiO_2 part of the image and was masked to improve clarity. Panel d is a line profile along the y (vertical) axis from GPA image (c) and summed over 250 pixels. The corresponding area is marked by a black dashed rectangle on the GPA image (c). Reference for the lattice deformation was taken in the red rectangle area indicated on the STEM image (a) and on both GPA images (b and c). The color scale for GPA images is indicated along the axis of the plot in panel d.

parameters of Si and SiGe, while the RSM around (115) reflections shows information about both the in-plane and the out-of-plane lattice parameters.

For the three samples, the RSMs around (004) Si and SiGe reflections exhibit a sharp intense peak centered at $Qz = 4.62\text{Å}^{-1}$ attributed to the Si substrate. In samples A and B, the SOI system is slightly twisted from the Si substrate as evidenced by the small difference in Qy between the peaks of the Si top-SOI layer and the Si substrate on RSMs (see the left panel in Figure Figure 5.7 a and Figure 5.7 b. The peak of the $Si_{1-x}Ge_x$ layer is broader and positioned at $Qz = 4.47\text{Å}^{-1}$ for sample A and $Qz = 4.51\text{Å}^{-1}$ for sample C. It is virtually invisible for sample B because of thickness fringes coming from the 12 nm thick silicon layer of the SOI.

On the RSM around (115) (see Figure 5.7 a, right panel), the peak of the SiGe layer is positioned at the same Qy as the peak of the Si substrate. This confirms that the SiGe layer is pseudomorphic, i.e., it has the same in-plane lattice parameter as the Si substrate.

From the Qz coordinates of the peaks, we can deduce the lattice parameters along the out-of-plane axis for Si and SiGe and then calculate a difference of lattice parameters (Δa_z). For sample A using the (004) RSM (see Figure 5.7a, left panel), we find a difference of (Δa_z) = 3.5%, and using the (115) RSM (see Figure 5.7a, right panel), a difference of (Δa_z) = 3.68%. These distorsions correspond (following eqs 1 and 2) to a concentration in Si of 52.2% and 50.1%, respectively, in good agreement with the 50% value determined by EDS (Figure 2). For sample C using the 004 RSM (see Figure 5.7c), we find a noticeably smaller value of (Δa_z) = 2.6%. This smaller strain is representative of a partial relaxation of the $Si_{0.5}Ge_{0.5}$ layer in agreement with the presence of disloca-

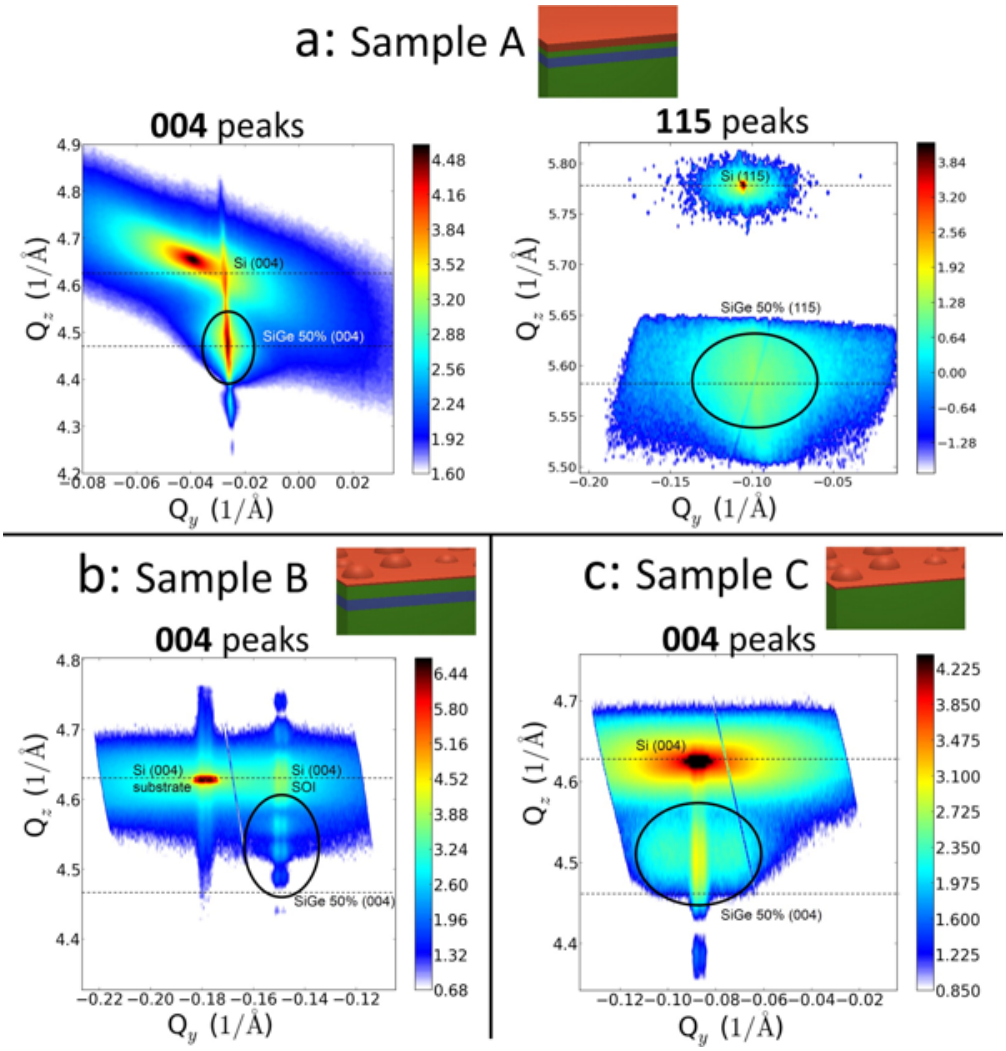

Figure 5.7: (a) Reciprocal space maps (RSMs) around 004 (left panel) and 115 (right panel) Si and SiGe Bragg peaks of sample A. (b and c) RSMs around 004 Si and SiGe Bragg peaks of samples B and C, respectively.

tions and islands evidenced in Figure 3.

For sample B (see Figure 5.7b), while an accurate position of the SiGe peak along the z-axis can not be determined, a bright diffuse intensity is attributed to SiGe at a Qz position larger than 4.5 $Å^{-1}$, which is again representative of a partial relaxation exactly like that in the case of sample C.

We did not record RSMs around (115) reflections for sample B and C, but the difference in Qz between the peak of the SiGe and the one of the Si visible on the (004) RSMs shows the partial relaxation of the SiGe.

These measurements already show that the strain of the SiGe layers obtained by direct deposition (on Si and on SOI) is completely different from the one with the two-step deposition-condensation process. Using the focused X-ray beam, a mapping of a 20 × 20 μm^2 region of sample A was performed using the quick continuous mapping (K-Map) technique developed at the ID01 beamline. Figure 5.8 shows a map of the

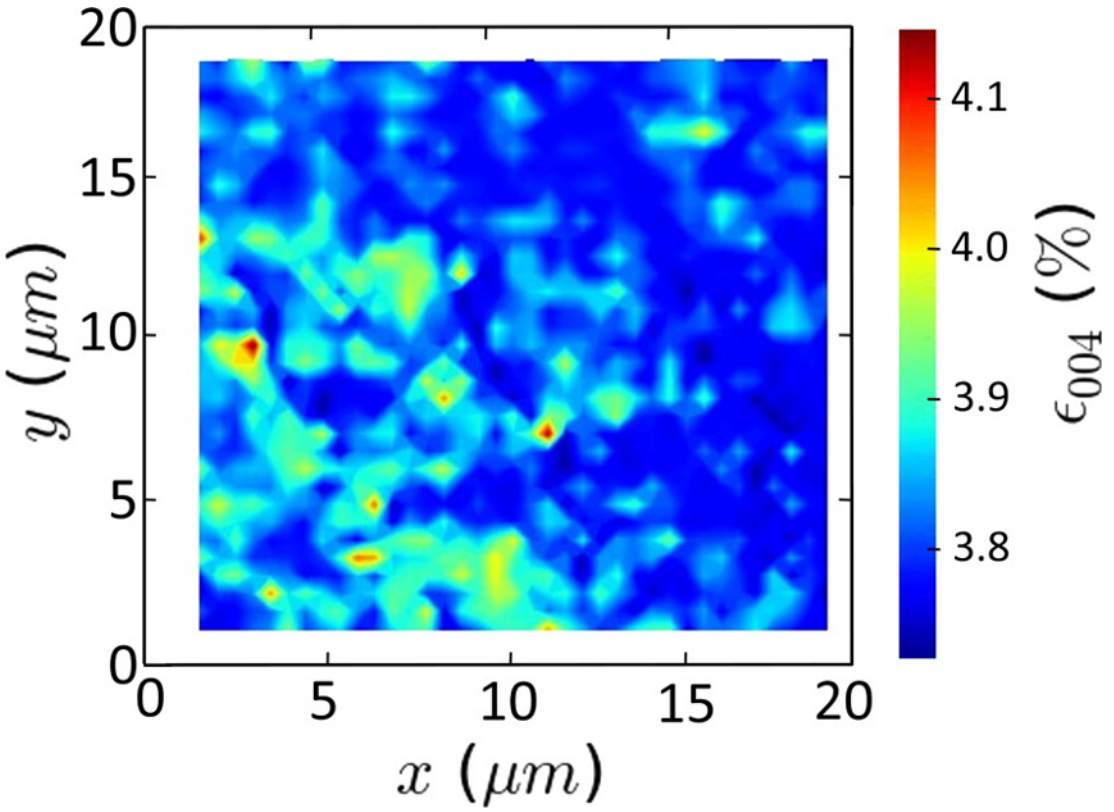

Figure 5.8: Map of a region of 20 × 20 μm^2 of the strain of the 004 planes of the SiGe layer for sample A. The strain is calculated with strain-free silicon as a reference (aSi = 5.4309Å).

strain on the (004) planes of the SiGe in this region. The origin of the strain values is taken for strain-free silicon. The map shows an average strain of about $3.85 \pm 0.05\%$ on large areas (20 × 20 μm^2) with low variations, which reflects a very good homogeneity over the entire region. This average strain corresponds to a $Si_{0.47}Ge_{0.53}$ alloy fully biaxially strained on Si substrate. This result is in very good agreement with the electron microscopy results. It confirms the absence of relaxation of the $Si_{0.5}Ge_{0.5}$ layer over large areas and probably over the entire sample.

5.4 Discussions

In summary, we have compared the morphological and structural evolution of $Si_{0.5}Ge_{0.5}$ epitaxial layers obtained by direct deposition on Si and on SOI and by a two-step deposition-condensation process. It should first be noted that the Si-top SOI layer is in principle sufficiently thin (12 nm) to produce a significant increase of the critical thickness of misfit dislocations nucleation as would predict the effect of the substrate compliance. The experiments were then well-suited to determine the compliant effect of SOI substrate.

In spite of that, it is found that the relaxation of $Si_{0.5}Ge_{0.5}$ is similar on bulk Si and SOI. This first reveals that the SiO_2/Si interface is rigid as discussed below. In both

cases, relaxation is accompanied by both the growth of 3D islands and the introduction of misfit dislocations at the SiGe/Si interface. Tensile strain in the Si-top layer, as predicted for a sufficiently thin compliant substrate, has not been observed either by GPA or by X-ray diffraction.

In addition, even in sample A obtained via deposition- condensation (where the $Si_{0.5}Ge_{0.5}$ layer after condensation is much thicker and unrelaxed), the amount of strain in the Si-top layer was also too low to be observed. These results confirm that at this temperature (750 °C), the SiO_2/Si interface is fully rigid and the SOI does not behave as a compliant substrate for the epitaxial growth of SiGe.

In this last case, the large increase of the critical thickness for an epitaxial overlayer, i.e., for both the 2D-3D growth transition and dislocations, nucleation is then attributable only to the deposition followed by condensation process. Indeed, with this process, the 8 nm thick $Si_{0.5}Ge_{0.5}$ layer is still flat and fully strained as indicated by both GPA and X-ray diffraction measurements. In similar conditions, the same SiGe layers obtained by direct deposition exhibit 3D islands and are partially relaxed by misfit dislocations. The delay of the nucleation of 3D islands in sample A is easily understood by the presence of the SiO_2 cap layer which fully inhibits the surface diffusion at the $Si_{0.5}Ge_{0.5}$ top surface and thus prohibits the nucleation of islands.

The increase of the critical thickness of dislocation nucleation is more difficult to understand. Indeed, it should be noted that in spite of the extensive literature on dislocations, the nucleation mechanism is extremely difficult to observe and the nature of dislocation sources remains unknown. Various mechanisms have been suggested to favor the nucleation of dislocations, such as the presence of surface steps, surface dislocation loops, point defects, extended defects, and interfacial impurities.

The presence of the SiO_2 cap layer can inhibit the nucleation of dislocations. However, while surface mechanisms prevail in various heteroepitaxial systems, they are commonly considered as negligible in SiGe/Si.

In this system, the source of dislocations commonly reported is the density of point defects and their ability to nucleate clusters. In our experimental conditions, the SiGe layers are subjected to thermal oxidation which is known to induce silicon self-interstitial (I's) injection into the subsurface. Therefore, in the whole SiGe/SOI system considered, the density of self-interstitials is much larger than in conventional epitaxial systems. We suggest that this large density of I's can be at the origin of the strengthening of the SiGe layer. The increase of the critical thickness of nucleation of dislocations would then be attributed to a mechanism similar to the Cottrel atmosphere in face-centered cubic metals.

5.5 Conclusion

We compared SiGe membranes fabricated by three different processes: direct deposition of$Si_{0.5}Ge_{0.5}$ either on Si(001) nominal substrate or on UT-SOI, and deposition of SiGe with low Ge concentration on silicon-on-insulator followed by Ge enrichment by condensation.

In spite of the very thin top Si layer of the UT-SOI, no compliance effect was observed for the sample of $Si_{0.5}Ge_{0.5}$ deposited on UT-SOI. Instead, we observed the same relaxation by island nucleation and dislocation nucleation as on Si(001) nominal substrate.

We show that the formation of 8 nm thick fully strained Ge-rich layers free of defects with flat surface is possible only by the two-step epitaxy-condensation process. We demonstrate that this process enables the total inhibition of the morphological instability, together with the hindering of dislocations for a $Si_{0.5}Ge_{0.5}$ thickness of 8 nm, which is much greater than those commonly obtained by direct deposition. We verify that the $Si_{0.5}Ge_{0.5}$ layer is fully strained and homogeneous over large areas. This remarkable stability can be explained by the injection of self-interstitials in the GRL during the condensation even if a reduced surface diffusion at the SiO_2/SiGe interface can not be ruled out. The results can be generalized to different systems, and we think that this work will promote and expand possibilities on a wide variety of devices.

Chapter 6

Conclusions

The aim of my PhD thesis was to understand and control the formation of SiGe nanostructures for different applications in the field of micro- nano- and opto-electronics and also in photovoltaics for the fabrication of third generation solar cells. In this context, my research project was focused on the self-organisation of SiGe 1D and 0D nanostructures on Si(001) substrate.

Epitaxial growth technique has been one of the cornerstones of semiconductor industry, which is used in almost all the semiconductor devices, and in particular the hetero-epitaxy is ubiquitously used to fabricate hetero-interfaces and hetero-structures which control flows of charge carriers in semiconductor devices. It is well-known that the hetero-epitaxial growth is dramatically affected by the mismatch strain due to the different lattice constants between substrate and deposited layer materials. It has attracted lots of research interests to rationalize the influence of strain on the growth. The epitaxial strain commonly called strain-engineering, is regarded as another degree of freedom for tuning physical properties of semiconductors including band gap and charge carrier mobility etc. Nanostructures such as quantum dots and quantum wires could be fabricated by taking advantage of the hetero-epitaxial strain. Moreover, the SiGe epitaxy has drawn considerable attention not only because of its great potential applications but also because it is regarded as a prototype system of hetero-epitaxy since the two materials have the same crystallographic structure. The morphological evolution of SiGe epitaxy follows the Stranski-Krostanov growth mode with the transition from 2D to 3D growth. In order to control the growth of 3D ultra-small islands for the foreseen applications, we need to fully understand the driving force of the 2D-3D transition as well as the kinetic and energetic pathways. I have first investigated both experimentally and theoretically this 2D-3D transition in this thesis. Second I studied the spontaneous self-organisation of quantum dots in a very narrow regime.

The first part of this thesis was dedicated to a a non-exhaustive review on the SiGe nanostructures, from the fundamental to their applications. In chapter 2, I addressed a fundamental issue in Stranski–Krastanov growth mode hetero-epitaxy which concerns

the pathways of 2D-3D transition in Stranski-Krostanov. It was suggested in various studies that there exist two pathways : nucleation in high-strain regime and ATG instability in low-strain regime. However, no quantitative assessment of these two regimes and evolution was given. With classic nucleation theory and master equation, we estimated the nucleation time scale with respect to different amount of strain, which is actually proportional to SiGe concentration. On the other hand, when the morphological evolution is treated in the scenario of ATG instability, which is described by continuum equation governed by surface diffusion, we could also estimate the time scale of its morphological evolution. We found that the time scale of nucleation increases exponentially when lowering composition or amount of strain as e^{1/x^4}, while the characteristic time of ATG instability t^{ATG} merely evolves as $1/x^8$ ruled by the competition between elasticity and capillarity. In high-strain regime, the time scale of nucleation τ^{nuc} is smaller than that of ATG instability. Nucleation will then take place firstly, while it is larger and τ^{nuc} would rapidly exceed t^{ATG} at low-strain regime. The crossover composition x_c between these two regimes is found around 0.5 at growth temperature $T = 550\,°C$. Experimentally we varied the composition of SiGe to identify the cross-over between the growth pathways at $T = 550\,°C$. The thickness was adjusted to catch the onset of 3D growth. We experimentally find that the crossover composition lies between 0.5 and 0.6 in good agreement with theoretical predictions. This work demonstrated for the first time, the different driving forces of the 2D-3D transition and the competition between ATG instability and nucleation. The results rationalized the mechanism of transition depending on the amount of strain, which is evidenced in SiGe system. The proposed model shed some new light onto the nature of epitaxial growth and could be used to other epitaxy system.

In chapter 3, I investigated the driving force that could control the spontaneous self-organisation of islands. For that, I determined the interactions between coherent islands. These interactions play also a crucial role in the islands size homogeneity and density. In the literature, the coherent islands have been widely recognized as energetically repulsive due to their elastic field. In experiments, within specific conditions, the islands are found to be clustering into aggregates, indicating the presence of preferential nucleation centers in the vicinity of islands or an attraction between islands during the formation. First-principle calculations revealed a non-intuitive strong effect of strain-dependent surface energy, which is actually also affecting the interaction between islands. In the model, we consider the interplay of strain-dependent surface energy and elastic energy. We found that in a narrow growth regime, strain-dependent surface energy could over-compensate the elastic energy repulsion and induce attractions between islands. The regime of attraction is only obtained for relatively small and highly strained (105) faceted islands. Considering the kinetic point of view, we then calculated the nucleation energy barrier of a growing island in the elastic field created by an existing island. The nucleation energy barrier is significantly reduced

about 0.1 eV, because of the existence of elastic inhomogeneity, which could modify the sites of preferential nucleation . As a consequence, this effect also contributes to the self-organisation of islands in very close vicinity. This findings open a new way to fabricate high-density quantum dots or quantum dot molecules and could be generalized to various heteroepitaxial systems.

In chapter 4, I investigated the self-organisation of islands on self-patterned substrate and I considered especially the presence of steps on a substrate in the case of a vicinal substrate. The latter could be used to tune the growth of coherent islands as the geometrical elasticity is broken compared with nominal substrate. In this part of my work, I studied the dynamic evolution of strained epitaxial films on vicinal substrates with parallel miscut steps along <110> direction. In this part the aim was to determine the effect of anisotrocic elasticity on the morphology of islands. We assessed both theoretically and experimentally the morphological evolution of islands on a vicinal substrate. We have shown that the anisotropic in plane relaxation is responsible of the elongation of islands on the substrate. We extracted from the perpendicular strain measured by x-ray diffraction, the planar strain relaxation ascribed to the step edges. We find that the elongation is in quantitative agreement with the value predicted theoretically. Nanowires 1µm long with very narrow (25nm) lateral dimensions were obtained on a 10°off misoriented substrate.

In Chapter 5, the use of a compliant buffer layer was investigated to control the epitaxial growth and possibly increase the Ge concentration in the coherent SiGe nanostructures. We have shown that the condensation of dilute SiGe alloy on silicon on insulator substrate could be efficiently used to fabricate highly strained Ge-rich epilayer. in this part, the kinetics of condensation is systematically studied on different substrates. The process of condensation shows very intriguing mechanisms with the stabilization of a 50% concentration SiGe alloy during the whole set of experiments whatever the concentration of the initial layer is. The process provides a simple and efficient way to fabricate fully strained and free of defect pure Ge 5nm thick layer, which is an unsurpassed result. The process also allows to fabricate fully strained SiGe epilayers which are not viable by direct epitaxial growth. The Ge-rich layers obtained by condensation could be used subsequently for the self-organisation of highly strained pure Ge islands free of dislocations. This work is still under investigation and will require further work to be completed.

In conclusion, we have clarified different fundamental mechanisms that were unsuspected before. We have also developed generic processes that could be applied to various different systems. The work has been supported by a combination of theoretical and experimental work. It relies on systematic studies that have provided a deep understanding of the phenomena and solid foundation for future work.

Appendix A

Elasticity of Epitaxy

A.1 Elastic Equations

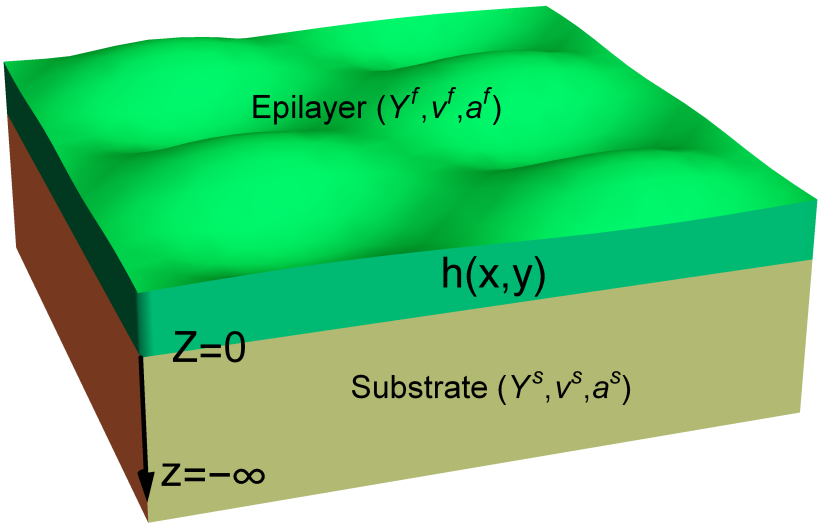

Figure A.1: Elasticity issues of epitaxial growth we deal with

The issue aimed to resolve here is approximately in mechanical equilibrium which could be achieved in very short time scale[49]. The system satisfies equilibrium equation:

$$\partial_j \sigma_{ij} = 0 \tag{A.1}$$

where $i, j = x, y, z$. According to Hulk's law, in isotropic elasticity, we have:

$$\sigma_{ij} = \frac{Y^p}{1+\nu^p}[e_{ij} + \frac{\nu^p}{1-2\nu^p} e_{ij}\delta_{ij}] \tag{A.2}$$

where Y^p is the Young's modulus and ν^p is Poisson ratio with $p = s, f$ representing substrate and epilayer respectively.
For the whole system, the substrate is taken as reference.The geometric equation for

substrate is:

$$e^s_{ij} = \frac{1}{2}(u_{i,j} + u_{j,i}) \tag{A.3}$$

Combining Equation A.1, Equation A.2, Equation A.3, one could get Lam*é* equation:

$$\boldsymbol{\nabla}(div\ \boldsymbol{u}) + (1 - 2\nu^p)\boldsymbol{\Delta u} = \mathbf{0}. \tag{A.4}$$

Note that for epilayer with respect to substrate when it is taken as reference in x and y directions:

$$e^f_{ij} = \frac{1}{2}(u_{i,j} + u_{j,i}) - \delta\mathbb{1} \tag{A.5}$$

where δ is the lattice mismatch between epilayer and substrate and $\mathbb{1}$ is identical matrix.

A.2 Boundary Conditions

The epitaxy at the substrate/epilayer interface ($z = 0$) enforces the continuity of displacements and streses:

$$\boldsymbol{u}|_{z=0^-} = \boldsymbol{u}|_{z=0^+} \tag{A.6}$$

$$\boldsymbol{\sigma}[\boldsymbol{u}] \cdot \boldsymbol{z}|_{z=0^-} = \boldsymbol{\sigma}[\boldsymbol{u}] \cdot \boldsymbol{z}|_{z=0^+} \tag{A.7}$$

On the surface of epilayer($z = h(\boldsymbol{r})$), negligible pressure on the surface implies that the surface is free of stress in normal direction:

$$\boldsymbol{\sigma}[\boldsymbol{u}] \cdot \boldsymbol{n}|_{z=h(\boldsymbol{r})} = 0 \tag{A.8}$$

where $\boldsymbol{n}|_{z=h(\boldsymbol{r})}$ is the nornal direction, which in general case could be calculated as:

$$\boldsymbol{n} = \frac{1}{\sqrt{1 + (\frac{\partial h}{\partial x})^2 + (\frac{\partial h}{\partial y})^2}}(-\frac{\partial h}{\partial x}, -\frac{\partial h}{\partial y}, 1) \tag{A.9}$$

and merely $\boldsymbol{n} = (0, 0, 1)$ for flat film case.

A.3 Flat Case

We consider a flat epilayer with infinit size ($x, y \in \{-\infty, \infty\}$), the symmetry of the system enforces that displacement $\boldsymbol{u}$ and strain $\boldsymbol{\sigma}$ are independent of x and y. Together with Equation A.1, one could consequently get $\boldsymbol{\sigma} = \boldsymbol{c}$ are all constants. By solving inversely Equation A.2 we can know that $\boldsymbol{e}$ are also constants. Substituting into Equation A.3 and Equation A.5 one would get that $\boldsymbol{u}$ are merely a linear function of z, as they are independent of x and y.
Consequently we can write displacement $\boldsymbol{u}$ as:

$$\begin{bmatrix} u^p_x \\ u^p_y \\ u^p_z \end{bmatrix} = \begin{bmatrix} C^p_1 z \\ C^p_3 z \\ C^p_5 z \end{bmatrix} + \begin{bmatrix} C^p_2 \\ C^p_4 \\ C^p_6 \end{bmatrix}$$

where $p = s, f$ representing substrate and epilayer.
For substrate, at the limit $z = -\infty$, the materials are supposed to be immune to the elasticity caused by epilayer, so we get $C_\alpha^s = 0$ where $\alpha = 1,2,..6$ and $\boldsymbol{u}^s = \mathbf{0}$. Consequently we have $\boldsymbol{e}^s = \mathbf{0}$ and $\boldsymbol{\sigma}^s = \mathbf{0}$ by solving Equation A.3 and Equation A.2.
For epilayer, boundary condition of continuity Equation A.6 leads to:

$$\begin{bmatrix} C_2^f \\ C_4^f \\ C_6^f \end{bmatrix} = \mathbf{0}$$

and $\sigma_{xz} = \sigma_{yz} = 0$ enforce $C_1^f = C_3^f = 0$ Then we get:

$$\begin{bmatrix} e_{xx}^f \\ e_{yy}^f \\ e_{zz}^f \end{bmatrix} = \begin{bmatrix} -\delta \\ -\delta \\ C_5^f - \delta \end{bmatrix}$$

which is subsequently substituted into Equation A.2, we get:

$$\sigma_{zz}^f = \frac{Y^f}{1+\nu^f}\{C_5^f + \frac{\nu^f}{1-2\nu^f}(C_5^p - 3\delta)\} = 0$$

using boundary condition Equation A.7, we have $e_{zz}^f = 0$, solve this equation and finally get:

$$C_5^f = \frac{1+\nu}{1-\nu}\delta \tag{A.10}$$

and:

$$\boldsymbol{u^f} = \begin{bmatrix} 0 \\ 0 \\ \frac{1+\nu^f}{1-\nu^f}\delta z \end{bmatrix}$$

Finally the elastic energy density or elastic chemical potential of flat film is calculated as:

$$\mu_0 = \frac{1}{2}e_{ij}\sigma_{ij} = \frac{Y^f\delta^2}{1-\nu^f} \tag{A.11}$$

A.4 First-order approximation

Morphological function $h(\boldsymbol{r})$ is decomposed as:

$$h(\boldsymbol{r}) = \bar{h} + \epsilon h(\boldsymbol{r}) \tag{A.12}$$

where $\bar{h}$ is the mean height of epilayer and $\epsilon h(\boldsymbol{r})$ describes the small undulations with respect to $\bar{h}$. To solve the linear derivative equation Equation A.4, the undulation $\epsilon h(\boldsymbol{r})$ is represented in Fourier space as:

$$\hat{h}_{\boldsymbol{k}} = \frac{1}{(2\pi)^2}\int h(\boldsymbol{r})e^{-i\boldsymbol{k}\cdot\boldsymbol{r}}d\boldsymbol{r} \tag{A.13}$$

where $e^{-i\boldsymbol{k}\cdot\boldsymbol{r}} = e^{-i(k_x x + k_y y)}$ is the 2D wave vector and accordingly, the displacement is decomposed as $\boldsymbol{u} = \bar{\boldsymbol{u}}_0 + \epsilon\boldsymbol{u}$. $\bar{\boldsymbol{u}}_0$ and $\bar{\boldsymbol{h}}$ correspond to displacement and morphological function in the flat case as zeroth order. The linear derivative equation could be conveniently numerically resolved in Fourier space. In the first order, we search a solution of displacement $\boldsymbol{u}$ as:

$$\epsilon\boldsymbol{u} = \epsilon\hat{\boldsymbol{u}}_{(\boldsymbol{k},z)}e^{-i\boldsymbol{k}\cdot\boldsymbol{r}} \tag{A.14}$$

Substituting into Equation A.4, we get:

$$-\begin{bmatrix} k_x^2\hat{u}_x + k_x k_y\hat{u}_y + ik_x\hat{u}_z' \\ k_x k_y\hat{u}_x + k_y^2\hat{u}_y + ik_x\hat{u}_z' \\ ik_x\hat{u}_x' + ik_y\hat{u}_y' - \hat{u}_z'' \end{bmatrix} + (1-2\nu^{sf})(-\boldsymbol{k}^2 + \frac{\partial^2}{\partial^2 z})\begin{bmatrix}\hat{u}_x\\ \hat{u}_y\\ \hat{u}_z\end{bmatrix} = \begin{bmatrix}0\\0\\0\end{bmatrix} \tag{A.15}$$

which is a second-order linear differential equation set with $\nu^{sf} = \nu^s, \nu^f$ are the Poisson ratio of substrate and epilayer. In their solutions, there would be 12 constants supposed to be determined by Boundary Conditions Equations.

Boundary Conditions Equations(B.C.E)

1. In substrate, at the limit $z = -\infty$, $\boldsymbol{u}^s$ shoul not goes to infinity , resulting in 3 B.C.E.

2. At the interface, Equation A.6 and Equation A.7 offer 6 B.C.E.

3. The state of free epilayer Equation A.8then offers 3 B.C.E

With these 12 B.C.E, one could finally determine the $\hat{\boldsymbol{u}}_{(\boldsymbol{k},z)}$ of substrate and epilayer.

A.5 First-order Solutions

The 0th order has been resolved as in flat case, here we search the first-order solutions. Displacements of substrate $\boldsymbol{u}^{sf}$ are resolved to be:

$$\boldsymbol{u}^{sf} = \frac{e^{-|\boldsymbol{k}|z}}{8|\boldsymbol{k}|^3(1-\nu^{sf})(1-2\nu^{sf})} \times \begin{bmatrix}A_1^{sf}\\A_2^{sf}\\A_3^{sf}\end{bmatrix} + \frac{e^{|\boldsymbol{k}|z}}{8|\boldsymbol{k}|^3(1-\nu^{sf})(1-2\nu^{sf})} \times \begin{bmatrix}B_1^{sf}\\B_2^{sf}\\B_3^{sf}\end{bmatrix} \tag{A.16}$$

where

$$\begin{bmatrix} A_1^{sf} \\ A_2^{sf} \\ A_3^{sf} \end{bmatrix} = \begin{bmatrix} (1-2\nu^{sf})[k_x^2(|\boldsymbol{k}|z+1)-4(1-\nu^{sf})\boldsymbol{k}^2]\boldsymbol{C}_1^{sf}+(1-2\nu^{sf})(|\boldsymbol{k}|z+1)k_xk_y\boldsymbol{C}_2^{sf} \\ -2i(1-\nu^{sf})|\boldsymbol{k}|^2k_xz\boldsymbol{C}_3^{sf}+2(1-\nu^{sf})[2(1-2\nu^{sf})|\boldsymbol{k}|-k_x^2z]|\boldsymbol{k}|^2\boldsymbol{C}_4^{sf} \\ -2(1-\nu^{sf})|\boldsymbol{k}|^2k_xk_yz\boldsymbol{C}_5^{sf}+i(1-2\nu^{sf})(|\boldsymbol{k}|z+1)|\boldsymbol{k}|^2\boldsymbol{C}_6^{sf} \\ \\ (1-2\nu^{sf})(|\boldsymbol{k}|z+1)k_xk_y\boldsymbol{C}_1^{sf}+(1-2\nu^{sf})[k_y^2(|\boldsymbol{k}|z+1)-4(1-\nu^{sf})|\boldsymbol{k}|^2]\boldsymbol{C}_2^{sf} \\ -2i(1-\nu^{sf})|\boldsymbol{k}|^2k_yz\boldsymbol{C}_3^{sf}-2(1-\nu^{sf})|\boldsymbol{k}|^2k_xk_yz\boldsymbol{C}_4^{sf} \\ +2(1-\nu^{sf})[2(1-2\nu^{sf})|\boldsymbol{k}|-k_yz]|\boldsymbol{k}|^2\boldsymbol{C}_5^{sf}+i(1-2\nu^{sf})(|\boldsymbol{k}|z+1)|\boldsymbol{k}|^2k_y\boldsymbol{C}_6^{sf} \\ \\ -i(1-2\nu^{sf})k_x|\boldsymbol{k}|^2z\boldsymbol{C}_1^{sf}-i(1-2\nu^{sf})k_y|\boldsymbol{k}|^2z\boldsymbol{C}_2^{sf} \\ -2(1-\nu^{sf})(3-4\nu^{sf}+|\boldsymbol{k}|z)|\boldsymbol{k}|^2\boldsymbol{C}_3^{sf}+2i(1-\nu^{sf})(|\boldsymbol{k}|z+1)k_x|\boldsymbol{k}|^2\boldsymbol{C}_4^{sf} \\ +2i(1-\nu^{sf})(|\boldsymbol{k}|z+1)k_y|\boldsymbol{k}|^2\boldsymbol{C}_5^{sf}+(1-2\nu^{sf})[4(1-\nu^{sf})+|\boldsymbol{k}|z]|\boldsymbol{k}|^3 \end{bmatrix}$$

and

$$\begin{bmatrix} B_1^{sf} \\ B_2^{sf} \\ B_3^{sf} \end{bmatrix} = \begin{bmatrix} (1-2\nu^{sf})[k_x^2(|\boldsymbol{k}|z-1)+4(1-\nu^{sf})\boldsymbol{k}^2]\boldsymbol{C}_1^{sf}+(1-2\nu^{sf})(|\boldsymbol{k}|z-1)k_xk_y\boldsymbol{C}_2^{sf} \\ +2i(1-\nu^{sf})|\boldsymbol{k}|^2k_xz\boldsymbol{C}_3^{sf}+2(1-\nu^{sf})[2(1-2\nu^{sf})|\boldsymbol{k}|+k_x^2z]|\boldsymbol{k}|^2\boldsymbol{C}_4^{sf} \\ +2(1-\nu^{sf})|\boldsymbol{k}|^2k_xk_yz\boldsymbol{C}_5^{sf}+i(1-2\nu^{sf})(|\boldsymbol{k}|z-1)|\boldsymbol{k}|^2\boldsymbol{C}_6^{sf} \\ \\ (1-2\nu^{sf})(|\boldsymbol{k}|z-1)k_xk_y\boldsymbol{C}_1^{sf}+(1-2\nu^{sf})[k_y^2(|\boldsymbol{k}|z-1)-4(1-\nu^{sf})|\boldsymbol{k}|^2]\boldsymbol{C}_2^{sf} \\ +2i(1-\nu^{sf})|\boldsymbol{k}|^2k_yz\boldsymbol{C}_3^{sf}+2(1-\nu^{sf})|\boldsymbol{k}|^2k_xk_yz\boldsymbol{C}_4^{sf} \\ +2(1-\nu^{sf})[2(1-2\nu^{sf})|\boldsymbol{k}|+k_yz]|\boldsymbol{k}|^2\boldsymbol{C}_5^{sf}+i(1-2\nu^{sf})(|\boldsymbol{k}|z-1)|\boldsymbol{k}|^2k_y\boldsymbol{C}_6^{sf} \\ \\ i(1-2\nu^{sf})k_x|\boldsymbol{k}|^2z\boldsymbol{C}_1^{sf}+i(1-2\nu^{sf})k_y|\boldsymbol{k}|^2z\boldsymbol{C}_2^{sf} \\ +2(1-\nu^{sf})(3-4\nu^{sf}+|\boldsymbol{k}|z)|\boldsymbol{k}|^2\boldsymbol{C}_3^{sf}+2i(1-\nu^{sf})(|\boldsymbol{k}|z+1)k_x|\boldsymbol{k}|^2\boldsymbol{C}_4^{sf} \\ +2i(1-\nu^{sf})(|\boldsymbol{k}|z+1)k_y|\boldsymbol{k}|^2\boldsymbol{C}_5^{sf}+(1-2\nu^{sf})[4(1-\nu^{sf})-|\boldsymbol{k}|z]|\boldsymbol{k}|^3 \end{bmatrix}$$

In these equations the superscript sf denotes the substrate and epilayer respectively, for instance, ν^{sf} should be replaced by the Poisson's ratio of substrate material ν^s, $|\boldsymbol{k}| = \sqrt{k_x^2+k_y^2}$ and $\boldsymbol{C}_j^{sf}$ $(j=1,2...6)$ are the 12 constants to be determined.

A.5.1 B.C.E Apply

Firstly, $\boldsymbol{u}^s$ is supposed to be finite at $z=-\infty$, then we must have:

$$\begin{bmatrix} A_1^{sf} \\ A_2^{sf} \\ A_3^{sf} \end{bmatrix} = \boldsymbol{0} \tag{A.17}$$

thence 6 constants in substrate $\boldsymbol{C}_j^s (j = 1,2...6)$ reduce to 3 since we have:

$$\begin{bmatrix} \boldsymbol{C}_2^s \\ \boldsymbol{C}_4^s \\ \boldsymbol{C}_6^s \end{bmatrix} = \frac{1}{|\boldsymbol{k}|(4\nu^s - 3)} \begin{bmatrix} -4k_x^2(1-\nu^s)\boldsymbol{C}_1^s + k_y^2(-3+4\nu^s)\boldsymbol{C}_1^s - k_x k_y \boldsymbol{C}_3^s - ik_x|\boldsymbol{k}|\boldsymbol{C}_5^s \\ -k_x k_y \boldsymbol{C}_1^s + k_x^2(-3+4\nu^s)\boldsymbol{C}_3^s - 4k_x k_y(1-\nu^s)\boldsymbol{C}_3^s - ik_y|\boldsymbol{k}|\boldsymbol{C}_5^s \\ -ik_x|\boldsymbol{k}|\boldsymbol{C}_1^s - ik_y|\boldsymbol{k}|\boldsymbol{C}_3^s + 2\boldsymbol{k}^2(2\nu^s - 1)\boldsymbol{C}_5^s \end{bmatrix} \tag{A.18}$$

Secondly, substituting $z = 0$ into A.5, we get $\boldsymbol{u}^s$ and $\boldsymbol{u}^f$ at interface:

$$\boldsymbol{u}^s(z = 0^-) = \begin{bmatrix} \boldsymbol{C}_1^s \\ \boldsymbol{C}_3^s \\ \boldsymbol{C}_5^s \end{bmatrix} \tag{A.19}$$

and

$$\boldsymbol{u}^f(z = 0^+) = \begin{bmatrix} \boldsymbol{C}_1^f \\ \boldsymbol{C}_3^f \\ \boldsymbol{C}_5^f \end{bmatrix} \tag{A.20}$$

the continuity of displacement at $z = 0$ in A.6 enforces

$$\begin{bmatrix} \boldsymbol{C}_1^f \\ \boldsymbol{C}_3^f \\ \boldsymbol{C}_5^f \end{bmatrix} = \begin{bmatrix} \boldsymbol{C}_1^s \\ \boldsymbol{C}_3^s \\ \boldsymbol{C}_5^s \end{bmatrix} \tag{A.21}$$

We substitute A.5.1 into A.5 and get the displacement in substrate, which merely contains 3 constants $\boldsymbol{C}_1^s, \boldsymbol{C}_3^s, \boldsymbol{C}_5^s$. using A.3 and A.2, we calculate the stress at $z = 0$ to be:

$$\begin{aligned} \boldsymbol{\sigma}[\boldsymbol{u}] \cdot \boldsymbol{z}|_{z=0^-} = & \frac{Y^s}{2|\boldsymbol{k}|(4\nu^s - 3)(\nu^s + 1)} \\ & \begin{bmatrix} 4k_x^2(\nu^s - 1)\boldsymbol{C}_1^s + k_y^2(4\nu^s - 3)\boldsymbol{C}_1^s - k_x(k_y \boldsymbol{C}_3^s + 2i|\boldsymbol{k}|(2\nu^s - 1)\boldsymbol{C}_5^s) \\ -k_x k_y \boldsymbol{C}_1^s + k_x^2(4\nu^s - 3)\boldsymbol{C}_3^s + 2k_y(2k_y(\nu^s - 1)\boldsymbol{C}_1^s + i|\boldsymbol{k}|(-2\nu^s + 1)\boldsymbol{C}_5^s) \\ |\boldsymbol{k}|(2\nu^s - 1)(ik_x \boldsymbol{C}_1^s + ik_y \boldsymbol{C}_3^s) + 2\boldsymbol{k}^2(\nu^s - 1)\boldsymbol{C}_5^s \end{bmatrix} \end{aligned}$$

equal to $\boldsymbol{\sigma}[\boldsymbol{u}] \cdot \boldsymbol{z}|_{z=0^+}$ from the epilayer, which could be obtained similarly by using A.5 and A.2, resulting in three equations of $\boldsymbol{C}_j^f, j = 1,2...6$. Solve the equations and write

$\boldsymbol{C}_2^f, \boldsymbol{C}_4^f, \boldsymbol{C}_6^f$ explicitly we have:

$$\begin{bmatrix} \boldsymbol{C}_2^f \\ \boldsymbol{C}_4^f \\ \boldsymbol{C}_6^f \end{bmatrix} = \frac{1}{Y^f \left|\boldsymbol{k}\right| (4\nu^s - 3)(\nu^s + 1)}$$

$$\begin{bmatrix} 4k_x^2(\nu^s+1)(\nu^s-1)\boldsymbol{C}_1^f + k_y^2 Y^s(\nu^f+1)(4\nu^s-3)\boldsymbol{C}_1^f - Y^s k_x k_y(\nu^f+1)\boldsymbol{C}_3^f \\ +ik_x\left|\boldsymbol{k}\right|[2Y^s(1+\nu^f-2\nu^s-2\nu^s\nu^f)+Y^f(4\nu^s-3)(\nu^s+1)]\boldsymbol{C}_5^f \\ \\ -k_x k_y Y^s(1+\nu^f)\boldsymbol{C}_1^f + k_y^2 Y^s(1+\nu^f)(4\nu^s-3)\boldsymbol{C}_3^f + 4Y^s K_y^2(1+\nu^f)(-1+\nu^s)\boldsymbol{C}_3^f \\ +ik_y\left|\boldsymbol{k}\right|[2Y^s(1+\nu^f-2\nu^s-2\nu^s\nu^f)+Y^f(4\nu^s-3)(\nu^s+1)]\boldsymbol{C}_5^f \\ \\ \frac{|\boldsymbol{k}|}{\nu^f-1}\big(ik_x(Y^s(-1+\nu^f+2(\nu^f)^2)(-1+2\nu^f) - Y^f\nu^f(-3+\nu^s+4(\nu^f)^2)\boldsymbol{C}_1^f \\ +ik_y(Y^s(-1+\nu^f+2(\nu^f)^2)(-1+2\nu^s) - Yf\nu^f(-3+\nu^s+4(\nu^f)^2)))\boldsymbol{C}_3^f + \\ 2\left|\boldsymbol{k}\right| Y^s(-1+\nu^f+2(\nu^f)^2)(-1+\nu^s)\boldsymbol{C}_5^f\big) \end{bmatrix}$$

which are then substituted into A.5 and $\boldsymbol{u}^f$ of the first order could now be written as formulas merely containing $\boldsymbol{C}_1^f, \boldsymbol{C}_3^f, \boldsymbol{C}_5^f$. The formula is simple but too long, here we just use

$$\boldsymbol{u}_1^f\left(\boldsymbol{C}_1^f, \boldsymbol{C}_3^f, \boldsymbol{C}_5^f\right) \tag{A.22}$$

to represent it. And the final $\boldsymbol{u}^f$ is then the sum of 0th order and first order:

$$\boldsymbol{u}^f = \begin{bmatrix} 0 \\ 0 \\ \frac{1+\nu^f}{1-\nu^f}\delta z \end{bmatrix} + \boldsymbol{u}_1^f\left(\boldsymbol{C}_1^f, \boldsymbol{C}_3^f, \boldsymbol{C}_5^f\right) \tag{A.23}$$

, in which these three constants can be finally determined by the last B.C.E,that epilayer surface is free of strain in the normal direction.

Similarly as above, the stress on the epilayer surface could be calculated using A.5 and A.2, represented as:

$$\boldsymbol{\sigma}^f\left(\boldsymbol{C}_1^f, \boldsymbol{C}_3^f, \boldsymbol{C}_5^f\right) \tag{A.24}$$

For surface morphological function

$$h(\boldsymbol{r}) = \bar{h} + \epsilon e^{-i(k_x x + k_y y)}$$

its vector of normal direction on the surface is:

$$\boldsymbol{n} = \begin{bmatrix} \epsilon k_x e^{-i(k_x x + k_y y)} \\ \epsilon k_y e^{-i(k_x x + k_y y)} \\ 1 \end{bmatrix} \tag{A.25}$$

and the stress on the surface is:

$$\boldsymbol{\sigma}^f_{(z=h(\boldsymbol{r}))}\left(\boldsymbol{C}_1^f, \boldsymbol{C}_3^f, \boldsymbol{C}_5^f\right) \tag{A.26}$$

The final equation to determine these three constants is merely:

$$\boldsymbol{\sigma}^f_{(z=h(\boldsymbol{r}))}\left(\boldsymbol{C}^f_1,\boldsymbol{C}^f_3,\boldsymbol{C}^f_5\right)\cdot\boldsymbol{n}=\boldsymbol{0} \tag{A.27}$$

from which the last 3 undetermined constants can be resolved.

Till here all the constants are determined. And the elastic chemical potential is obtained as:

$$\mu=\left(\frac{1}{2}e^f_{ij}\sigma^f_{ij}\right)_{z=h(\boldsymbol{r})} \tag{A.28}$$

$$=\mu_0+\mu_1 \tag{A.29}$$

where μ_0 is given in A.3 and μ_1 to the second order is[72]:

$$\mu_1/\mu_0=-\omega_1\mathscr{H}_{ii}(h)+\omega_2(2h\boldsymbol{\Delta}h+\left|\boldsymbol{\Delta}h\right|^2)+\omega_2^*\left(2\mathscr{H}_{ij}[h\theta_{ijkl}\mathscr{H}_{kl}(h)]+\mathscr{H}_{ij}(h)\theta_{ijkl}\mathscr{H}_{kl}(h)\right)$$

with $i,j,k,l=x,y$ and notation $\theta_{ijij}=1,\theta_{xxxy}=\theta_{yyxx}=\nu^f,\theta_{xxyx}=\theta_{yxxy}=-\nu^f$, in other cases, $\theta_{ijkl}=0$; we also define the operator $\mathscr{H}$ as:

$$\mathscr{H}_{ij}(h)=\mathscr{F}^{-1}\{(k_ik_j/\left|\boldsymbol{k}\right|)\mathscr{F}[h]\}$$

with $=\mathscr{F},=\mathscr{F}^{-1}$ are respectively the Fourier Transform operator an the inverse. The elastic constant parameters $\omega_1,\omega_2,\omega_2^*$ are: $\omega_1=2Y^f(1-(\nu^s)^2)/Y^s(1-\nu^f)$, $\omega_2=(1+\nu^f)(1-\nu^f)+Y^f(1-2\nu^s)(1+\nu^s)/Y^s(1-\nu^f)$, $\omega_2^*=2(Y^f)^2(1-(\nu^s)^2)/(Y^s)^2(1-(\nu^f)^2)(1+\nu^f)$.

A.6 Elastic Energy and Biaxial Strain for thin epilayer

With the resolved surface elastic chemical potential for a given morphological function $h(x,y)$, assuming that the epilayer is very thin, one could approximately calculate the elastic energy in the epilayer using functional integration from the substrate to epilayer surface and obtain to the first order as:

$$E^{el}=\mu_0\int d\boldsymbol{r}\left\{h(\boldsymbol{r})-\zeta h(\boldsymbol{r})\mathscr{H}_{ii}[h(\boldsymbol{r})]\right\} \tag{A.30}$$

where μ_0 is given in A.3 and $\zeta=Y_f(1-\nu_s^2)/Y_s(1-\nu_f)$.

The biaxial strain on the surface $\epsilon(\boldsymbol{r})=\frac{1}{2}(e_{xx}+e_{yy})_{z=h(\boldsymbol{r})}$ could be deduced as :

$$\epsilon(\boldsymbol{r})=-\delta+\zeta\mathscr{H}_{ii}[h(\boldsymbol{r})] \tag{A.31}$$

Appendix B

Dynamics of ATG instability

The morphological evolution of epilayer at low-strain regime is governed by the ATG instability, for which materials redistribution proceeds via surface diffusion. We study the dynamics of morphological function $h(x,y,t)$ here.

The flux of materials on the epilayer surface stems from deposition F and surface diffusion and $\boldsymbol{J}_s$. Let us consider the diffusion of a small surface area dS and the variation of $h(x,y,t)$ in the normal direction $\boldsymbol{n}$ is actually the projection of the surface diffusion gradient along the surface onto $\boldsymbol{n}$, which is $-\int_s \boldsymbol{\nabla}_s \cdot \boldsymbol{J} dS$, where $\boldsymbol{\nabla}_s = \boldsymbol{\nabla} - (\boldsymbol{n}\cdot\boldsymbol{\nabla})\boldsymbol{n}$ and normal direction $\boldsymbol{n}$ is given in A.2. According to Fick's law, the dynamic equation of $h(x,y,t)$ could be written as:

$$\frac{\partial h(x,y,t)}{\partial t} = F + D\sqrt{1+\left|\boldsymbol{\nabla} h(x,y,t)\right|^2}\boldsymbol{\Delta}_s \mu \tag{B.1}$$

where D is the surface diffusion coefficient, $\boldsymbol{\Delta}_s = \partial^2/\partial x^2 + \partial^2/\partial y^2$ is the surface Laplacian and μ is the surface chemical potential including contributions from surface elasticity μ^{el}, given in Appendix A and capillarity $\mu^{\gamma} = \boldsymbol{\kappa}\gamma$ where $\boldsymbol{\kappa}$ and γ are surface curvature and surface energy respectively. The mean curvature is merely:

$$\boldsymbol{\kappa} = -\frac{h_{xx}(1+h_y^2) - 2h_x h_y h_{xy} + h_{yy}(1+h_x^2)}{(1+\left|\boldsymbol{\nabla} h\right|^2)^{3/2}} \tag{B.2}$$

As a result, we get:

$$\mu = \boldsymbol{\kappa}\gamma + \mu^{el} \tag{B.3}$$

We consider the case of $F = 0$ and let an epilayer with small noise fluctuation be the initial state which is written as:

$$h(x,y,t) = \bar{h} + h_1 \tag{B.4}$$

$$= \bar{h} + \epsilon e^{\sigma t + i(k_x x + k_y y)} \tag{B.5}$$

where $e^{\sigma t}$ describes the growth of undulation with respect to flat film $\bar{h}$. We substitute it into B.1 and in the first order, the factor $\sqrt{1+\left|\boldsymbol{\nabla} h(x,y,t)\right|^2}$ reduces to 1, curvature $\boldsymbol{\kappa}$

reduces to $\epsilon\left|\boldsymbol{k}\right|^2 e^{\sigma t+i(k_x x+k_y y)}$ and

$$\begin{aligned}\mu^{el} &= \mu_0(1-\omega_1\mathscr{H}_{ii}(h)) \\ &= \mu_0(1-\epsilon\omega_1\left|\boldsymbol{k}\right| e^{\sigma t+i(k_x x+k_y y)})\end{aligned}$$

then B.1 turns to:

$$\sigma = D(\mu_0\omega_1\left|\boldsymbol{k}\right|^3-\left|\boldsymbol{k}\right|^4\gamma) \tag{B.6}$$

which then turns to be a dimensionless formula:

$$\sigma = \left|\boldsymbol{k}\right|^3-\boldsymbol{k}^4 \tag{B.7}$$

where we define the the characteristic length scale and time scale:

$$l_0 = \frac{\gamma}{\mu_0\omega_1} = \frac{\gamma Y^s(1-\nu^f)^2}{2(Y^f)^3(1-(\nu^s)^2\delta^2} \tag{B.8}$$

$$t_0 = \frac{l_0^4}{D\gamma} \tag{B.9}$$

Here we could furthermore find the maximum ATG mode is $\boldsymbol{k}=3/4$, corresponding to a wavelength

$$\lambda_{ATG} = \frac{2\pi}{3/4}l_0 = \frac{4\pi\gamma Y^s(1-\nu^f)^2}{3(Y^f)^3(1-(\nu^s)^2\delta^2} \tag{B.10}$$

which, in case of $Y^s=Y^f=Y, \nu^s=\nu^f=\nu$, reduces to

$$\lambda_{ATG} = \frac{4\pi\gamma(1-\nu)}{3Y(1+\nu)\delta^2} \tag{B.11}$$

Appendix C

Equipements for experiments

Here we list the main experimental set-ups on which our experiments are performed. The NANOTECMAT experimental set-up installed in IM2NP is composed of various equipments including MBE (Molecular Beam Epitaxy) , AFM (Atomic Force Microscope), FIB (Focused Ions Beam), RTO (Rapid Thermal Oxidation), which thence offers plenty of possibility in nanostructure fabrications and characterizations.

C.1 MBE

The epitaxial growth of SiGe are all performed in the Riber MBE CBE32 system with a pressure to 10^{-11} torr in growth chamber. The Si flux comes from an electron beam evaporation system and Ge flux from effusion cell. Both the deposition rates of Si and Ge are precisely calibrated by in-situ RHEED system combined with a kSA 400 camera which permits the detection of the oscillation of RHEED e-beam patterns induced by the variation monolayer roughness on the sample surface. The sample could be heated up by the filaments installed on the backside of sample and the temperature is in-situ measured by a pyrometer. To keep the high vacuum during experiments, the growth chamber could be cooled down by a system with cycling liquid nitrogen to adsorb some gas desorbed from sample and sample holder. The set-up of growth chamber is shown in Figure C.1.

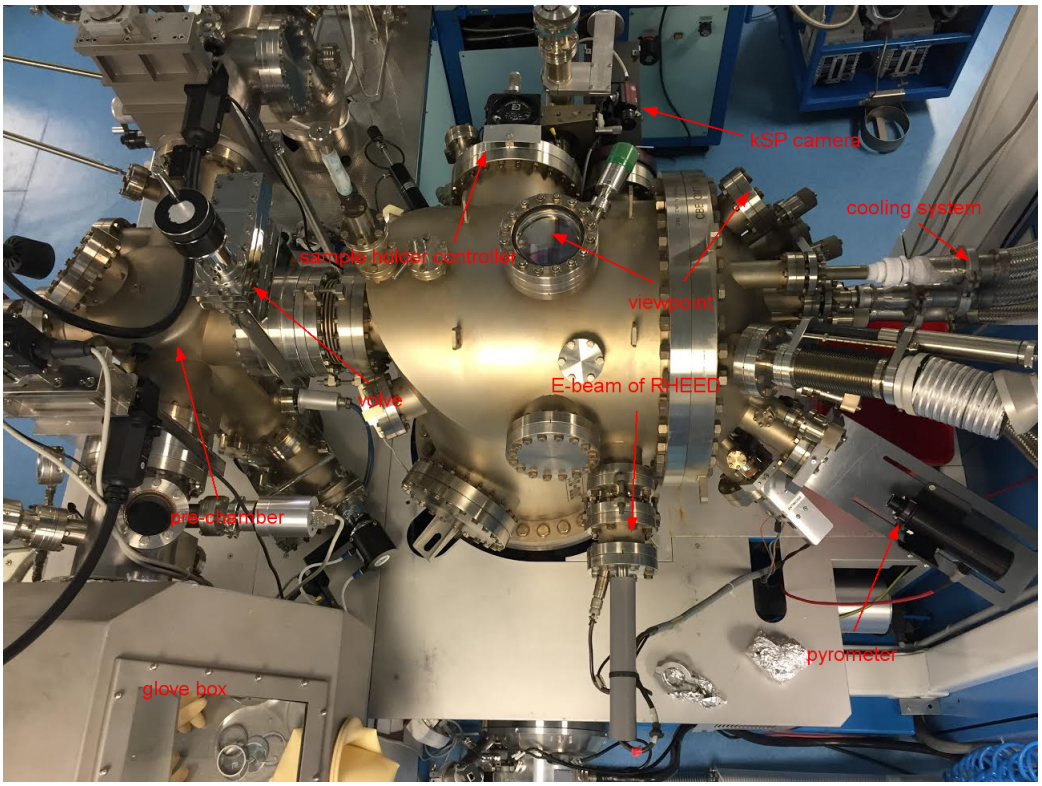

Figure C.1: Riber CBE32 MBE system

C.2 AFM

The AFM (XE-100 SPM system, PSIA co.) is mainly used to do the morphological characterization of samples.All the AFM images obtained in this thesis were obtained from this AFM system.

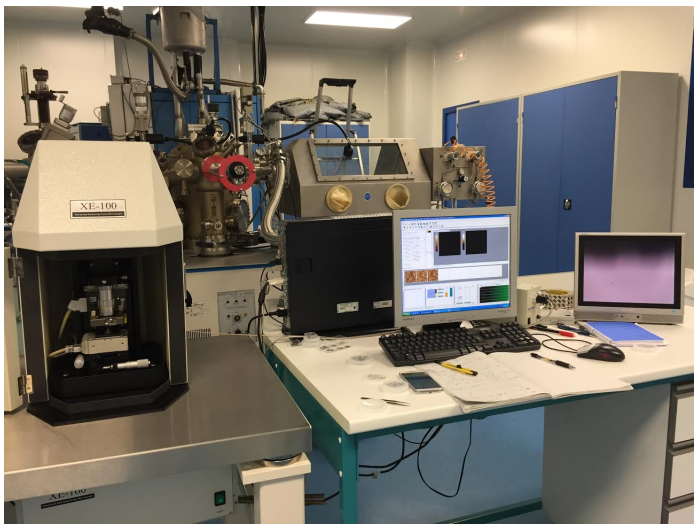

Figure C.2: AFM XE-100 SPM system

C.3 Dual-Beam FIB-SEM system

The Dual-Beam FIB-SEM system permits not only the morphology characterization, but also the high-resolution processes of nano-fabrication. In this system the FIB source is SiAu alloy, heated up to liquid during process, which then extracted and accelerated with high voltage. The ions beam then goes through a Wiens filter with which the ions species can be separated and selected on purpose. To avoid the contamination of implanted ions, we select the Si^{++} as the process ions to fabricate the patterns on Si substrate. In addition, a GIS (Gas Injection System) is installed onto the Dual-Beam system which could be used to deposit Pt or etch with XeF2 with the assistance of FIB or electron beam.

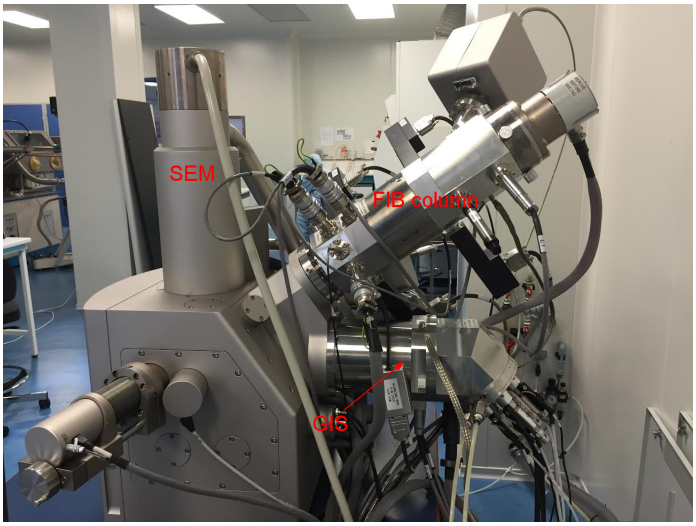

Figure C.3: Tescan FIB-SEM dual beam system

C.4 RTP

The commercial Jipelec JetFirst Rapid Thermal Processor allows to proceed the oxidation of SiGe or Si and annealing process. The oxidation of SiGe to condensate is performed in this system. The sample loaded into the furnace is heated up with lamps which allows a temperature increase rate about 100 °C /s, to a maximum process temperature about 1000 °C /s.

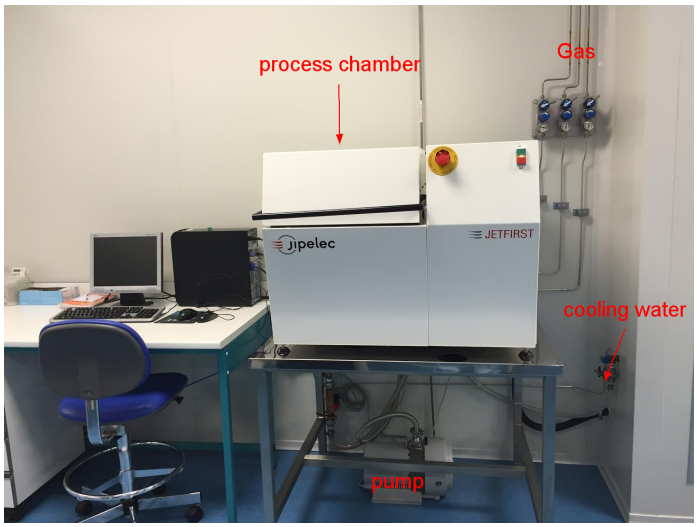

Figure C.4: Jipelec JetFirst Rapid Thermal Processor.

Appendix D

Elastic Constants

In the calculations of elasticity, we use some elastic constants for Si and Ge. The values of these constants are listed here for convenience.

Table D.1: Elastic Constants

Symbol	Representation	Value
Y_{Si}	Young's modulus of Si	$1.30 \times 10^{11} J/m^3$
Y_{Ge}	Young's modulus of Ge	$1.03 \times 10^{11} J/m^3$
Y_f	Young's modulus of $Si_{1-x}Ge_x$	Y_{Si}(1-x)+Y_{Ge} x
ν_{Si}	Poisson ratio of Si	0.279
ν_{Ge}	Poisson ratio of Ge	0.273
ν_f	Poisson ratio of $Si_{1-x}Ge_x$	ν_{Si}(1-x)+ ν_{Ge}x

Bibliography

[1] Udo W. Pohl (auth.). *Epitaxy of Semiconductors: Introduction to Physical Principles*. Graduate Texts in Physics. Springer-Verlag Berlin Heidelberg, 1 edition, 2013.

[2] Class for Physics of the Royal Swedish Academy of Sciences. Scientific background on the nobel prize in physics 2014"efficient blue light-emitting diodes leading to bright and energy-saving white light sources", 2014.

[3] Shuji Nakamura, Takashi Mukai, and Masayuki Senoh. Candela-class high-brightness ingan/algan double-heterostructure blue-light-emitting diodes. *Applied Physics Letters*, 64(13):1687–1689, 1994.

[4] Xin Guan, Jeanne Becdelievre, Benjamin Meunier, Abdennacer Benali, G Saint-Girons, Romain Bachelet, Philippe Regreny, Claude Botella, Geneviève Grenet, NP Blanchard, et al. Gaas core/srtio3 shell nanowires grown by molecular beam epitaxy. *Nano letters*, 16(4):2393–2399, 2016.

[5] AY Cho. Gaas epitaxy by a molecular beam method: observations of surface structure on the (001) face. *Journal of Applied Physics*, 42(5):2074–2081, 1971.

[6] MJ Ying, XL Du, YZ Liu, ZT Zhou, ZQ Zeng, ZX Mei, JF Jia, H Chen, QK Xue, and Z Zhang. Interface engineering for lattice-matched epitaxy of zno on (la, sr)(al, ta) o3 (111) substrate. *Applied Physics Letters*, 87(20):202107, 2005.

[7] Ravi Pillarisetty. Academic and industry research progress in germanium nanodevices. *Nature*, 479(7373):324–328, 2011.

[8] Ju Li, Zhiwei Shan, and Evan Ma. Elastic strain engineering for unprecedented materials properties. *MRS Bulletin*, 39:108–114, 2 2014.

[9] Minjoo L Lee, Eugene A Fitzgerald, Mayank T Bulsara, Matthew T Currie, and Anthony Lochtefeld. Strained si, sige, and ge channels for high-mobility metal-oxide-semiconductor field-effect transistors. *Journal of Applied Physics*, 97(1):011101, 2005.

[10] Tahir Ghani, Michael Armstrong, Chris Auth, M Bost, P Charvat, G Glass, T Hoffmann, K Johnson, C Kenyon, J Klaus, et al. A 90nm high volume manufacturing logic technology featuring novel 45nm gate length strained silicon cmos transistors. In *Electron Devices Meeting, 2003. IEDM'03 Technical Digest. IEEE International*, pages 11–6. IEEE, 2003.

[11] Michele Amato, Maurizia Palummo, Riccardo Rurali, and Stefano Ossicini. Silicon–germanium nanowires: chemistry and physics in play, from basic principles to advanced applications. *Chemical reviews*, 114(2):1371–1412, 2013.

[12] Neil W Ashcroft and N David Mermin. *Solid state physics (saunders college, philadelphia, 1976)*. 2010.

[13] Guang-Hong Lu, Martin Cuma, and Feng Liu. First-principles study of strain stabilization of ge (105) facet on si (001). *Physical Review B*, 72(12):125415, 2005.

[14] J-N Aqua, I Berbezier, L Favre, T Frisch, and A Ronda. Growth and self-organization of sige nanostructures. *Physics Reports*, 522(2):59–189, 2013.

[15] Feng Liu, Fang Wu, and MG Lagally. Effect of strain on structure and morphology of ultrathin ge films on si (001). *Chemical Reviews*, 97(4):1045–1062, 1997.

[16] Peter Lodahl, Sahand Mahmoodian, and Søren Stobbe. Interfacing single photons and single quantum dots with photonic nanostructures. *Reviews of Modern Physics*, 87(2):347, 2015.

[17] Mingjin Tang, Daniel J Cziczo, and Vicki H Grassian. Interactions of water with mineral dust aerosol: Water adsorption, hygroscopicity, cloud condensation, and ice nucleation. *Chemical reviews*, 116(7):4205–4259, 2016.

[18] A Vailionis, B Cho, G Glass, P Desjardins, David G Cahill, and JE Greene. Pathway for the strain-driven two-dimensional to three-dimensional transition during growth of ge on si (001). *Physical review letters*, 85(17):3672, 2000.

[19] DE Jesson, M Kästner, and B Voigtländer. Direct observation of subcritical fluctuations during the formation of strained semiconductor islands. *Physical review letters*, 84(2):330, 2000.

[20] Bert Voigtländer. Fundamental processes in si/si and ge/si epitaxy studied by scanning tunneling microscopy during growth. *Surface Science Reports*, 43(5):127–254, 2001.

[21] Philippe Gaillard, Jean-Noël Aqua, and Thomas Frisch. Kinetic monte carlo simulations of the growth of silicon germanium pyramids. *Physical Review B*, 87(12):125310, 2013.

[22] DB Migas, S Cereda, Francesco Montalenti, and Leo Miglio. Electronic and elastic contributions in the enhanced stability of ge (105) under compressive strain. *Surface science*, 556(2):121–128, 2004.

[23] Shklyaev OE, MJ Beck, M Asta, MJ Miksis, and PW Voorhees. Role of strain-dependent surface energies in ge/si (100) island formation. *Physical review letters*, 94(17):176102, 2005.

[24] Francesco Montalenti, P Raiteri, DB Migas, H Von Känel, A Rastelli, C Manzano, G Costantini, U Denker, OG Schmidt, K Kern, et al. Atomic-scale pathway of the pyramid-to-dome transition during ge growth on si (001). *Physical review letters*, 93(21):216102, 2004.

[25] RM Tromp, FM Ross, and MC Reuter. Instability-driven sige island growth. *Physical review letters*, 84(20):4641, 2000.

[26] P Sutter and MG Lagally. Nucleationless three-dimensional island formation in low-misfit heteroepitaxy. *Physical review letters*, 84(20):4637, 2000.

[27] J Tersoff, BJ Spencer, A Rastelli, and H Von Känel. Barrierless formation and faceting of sige islands on si (001). *Physical review letters*, 89(19):196104, 2002.

[28] Jean-Noël Aqua, Adrien Gouyé, Antoine Ronda, Thomas Frisch, and Isabelle Berbezier. Interrupted self-organization of sige pyramids. *Physical review letters*, 110(9):096101, 2013.

[29] A Malachias, S Kycia, G Medeiros-Ribeiro, R Magalhaes-Paniago, TI Kamins, and R Stanley Williams. 3d composition of epitaxial nanocrystals by anomalous x-ray diffraction: Observation of a si-rich core in ge domes on si (100). *Physical review letters*, 91(17):176101, 2003.

[30] A Portavoce, I Berbezier, and A Ronda. Sb-surfactant-mediated growth of si and ge nanostructures. *Physical Review B*, 69(15):155416, 2004.

[31] L Persichetti, A Sgarlata, M Fanfoni, and A Balzarotti. Shaping ge islands on si (001) surfaces with misorientation angle. *Physical review letters*, 104(3):036104, 2010.

[32] I Berbezier, A Ronda, F Volpi, and A Portavoce. Morphological evolution of sige layers. *Surface science*, 531(3):231–243, 2003.

[33] Tong Zhou, Guglielmo Vastola, Yong-Wei Zhang, Qijun Ren, Yongliang Fan, and Zhenyang Zhong. Unique features of laterally aligned gesi nanowires self-assembled on the vicinal si (001) surface misoriented toward the [100] direction. *Nanoscale*, 7(13):5835–5842, 2015.

[34] J Tersoff, Ch Teichert, and MG Lagally. Self-organization in growth of quantum dot superlattices. *Physical Review Letters*, 76(10):1675, 1996.

[35] VA Zinovyev, AV Dvurechenskii, PA Kuchinskaya, and VA Armbrister. Strain-induced formation of fourfold symmetric sige quantum dot molecules. *Physical review letters*, 111(26):265501, 2013.

[36] Soonshin Kwon, Zack CY Chen, Ji-Hun Kim, and Jie Xiang. Misfit-guided self-organization of anticorrelated ge quantum dot arrays on si nanowires. *Nano letters*, 12(9):4757–4762, 2012.

[37] H-J Kim-Lee, DE Savage, CS Ritz, MG Lagally, and KT Turner. Control of three-dimensional island growth with mechanically responsive single-crystal nanomembrane substrates. *Physical review letters*, 102(22):226103, 2009.

[38] Bin Yang, Feng Liu, and Max G Lagally. Local strain-mediated chemical potential control of quantum dot self-organization in heteroepitaxy. *Physical review letters*, 92(2):025502, 2004.

[39] Hao Hu, HJ Gao, and Feng Liu. Theory of directed nucleation of strained islands on patterned substrates. *Physical review letters*, 101(21):216102, 2008.

[40] Isabelle Berbezier and A Ronda. Sige nanostructures. *Surface Science Reports*, 64(2):47–98, 2009.

[41] R Hull, J Floro, J Graham, J Gray, M Gherasimova, A Portavoce, and FM Ross. Synthesis and functionalization of epitaxial quantum dot nanostructures for nanoelectronic architectures. *Materials Science in Semiconductor Processing*, 11(5):160–168, 2008.

[42] Martyna Grydlik, Gregor Langer, Thomas Fromherz, Friedrich Schäffler, and Moritz Brehm. Recipes for the fabrication of strictly ordered ge islands on pit-patterned si (001) substrates. *Nanotechnology*, 24(10):105601, 2013.

[43] Jianjun Zhang, Moritz Brehm, Martyna Grydlik, and Oliver G Schmidt. Evolution of epitaxial semiconductor nanodots and nanowires from supersaturated wetting layers. *Chemical Society Reviews*, 44(1):26–39, 2015.

[44] Detlev Grützmacher, Thomas Fromherz, Christian Dais, Julian Stangl, Elisabeth Müller, Yasin Ekinci, Harun H Solak, Hans Sigg, Rainer T Lechner, Eugen Wintersberger, et al. Three-dimensional si/ge quantum dot crystals. *Nano letters*, 7(10):3150–3156, 2007.

[45] X Xu, Jean-Noël Aqua, and T Frisch. Growth kinetics in a strained crystal film on a wavy patterned substrate. *Journal of Physics: Condensed Matter*, 24(4):045002, 2012.

[46] X Xu and J-N Aqua. Quantum dot growth on a stripe-pattern. *Thin Solid Films*, 543:7–10, 2013.

[47] Jean-Noël Aqua and Xianbin Xu. Directed self-organization of quantum dots. *Phys. Rev. E*, 90:030402, Sep 2014.

[48] Guang-Hong Lu and Feng Liu. Towards quantitative understanding of formation and stability of ge hut islands on si (001). *Physical review letters*, 94(17):176103, 2005.

[49] Jean-Noel Aqua and Thomas Frisch. Influence of surface energy anisotropy on the dynamics of quantum dot growth. *Physical Review B*, 82(8):085322, 2010.

[50] I Berbezier, M Descoins, B Ismail, H Maaref, and A Ronda. Influence of si (001) substrate misorientation on morphological and optical properties of ge quantum dots. *Journal of applied physics*, 98(6):063517, 2005.

[51] CM Retford, M Asta, MJ Miksis, PW Voorhees, and EB Webb III. Energetics of {105}-faceted ge nanowires on si (001): An atomistic calculation of edge contributions. *Physical Review B*, 75(7):075311, 2007.

[52] G Chen, B Sanduijav, D Matei, G Springholz, D Scopece, MJ Beck, F Montalenti, and L Miglio. Formation of ge nanoripples on vicinal si (1110):from stranski-krastanow seeds to a perfectly faceted wetting layer. *Physical review letters*, 108(5):055503, 2012.

[53] Kirill A Lozovoy, Andrey P Kokhanenko, and Alexander V Voitsekhovskii. Influence of edge energy on modeling the growth kinetics of quantum dots. *Crystal Growth & Design*, 15(3):1055–1059, 2015.

[54] C. Duport, C. Priester, and J. Villain. *Equilibrium shape of a coherent epitaxial cluster*, page 73. World Scientific, Singapore, 1997.

[55] D. Kashchiev. *Nucleation, basic theory with application.* Butterworth-Heinemann, 2000.

[56] L. Ratke and P. W. Voorhees. *Growth and Coarsening: Ostwald Ripening in Material Processing.* Springer, 2002.

[57] BJ Spencer, PW Voorhees, and SH Davis. Morphological instability in epitaxially strained dislocation-free solid films. *Physical review letters*, 67(26):3696, 1991.

[58] Feng Liu. Modeling and simulation of strain-mediated nanostructure formation on surface. *Handbook of Theoretical and Computational Nanotechnology*, 4:577–625, 2006.

[59] I Daruka, C Grossauer, G Springholz, and J Tersoff. Equilibrium phase diagrams for the elongation of epitaxial quantum dots into hut-shaped clusters and quantum wires. *Physical Review B*, 89(23):235427, 2014.

[60] TU Schülli, G Vastola, M-I Richard, A Malachias, G Renaud, F Uhlík, F Montalenti, G Chen, L Miglio, F Schäffler, et al. Enhanced relaxation and intermixing in ge islands grown on pit-patterned si (001) substrates. *Physical review letters*, 102(2):025502, 2009.

[61] Hao Hu, Hongjun Gao, and Feng Liu. Quantitative model of heterogeneous nucleation and growth of sige quantum dot molecules. *Physical review letters*, 109(10):106103, 2012.

[62] CJ Moore, CM Retford, MJ Beck, M Asta, MJ Miksis, and PW Voorhees. Orientation dependence of strained-ge surface energies near (001): role of dimer-vacancy lines and their interactions with steps. *Physical review letters*, 96(12):126101, 2006.

[63] Michele Amato, Stefano Ossicini, and Riccardo Rurali. Band-offset driven efficiency of the doping of sige core- shell nanowires. *Nano letters*, 11(2):594–598, 2010.

[64] Lijun Zhang, Mayeul d'Avezac, Jun-Wei Luo, and Alex Zunger. Genomic design of strong direct-gap optical transition in si/ge core/multishell nanowires. *Nano letters*, 12(2):984–991, 2012.

[65] Jianping Wang, Jun-Wei Luo, Lijun Zhang, and Alex Zunger. Reinterpretation of the expected electronic density of states of semiconductor nanowires. *Nano letters*, 15(1):88–95, 2014.

[66] JB Hannon, S Kodambaka, FM Ross, and RM Tromp. The influence of the surface migration of gold on the growth of silicon nanowires. *Nature*, 440(7080):69–71, 2006.

[67] Thomas David, Luc Roussel, Thomas Neisius, Martiane Cabie, Marc Gailhanou, and Claude Alfonso. Gold coverage and faceting of mbe grown silicon nanowires. *Journal of Crystal Growth*, 383:151–157, 2013.

[68] Jun Tatebayashi, Satoshi Kako, Jinfa Ho, Yasutomo Ota, Satoshi Iwamoto, and Yasuhiko Arakawa. Room-temperature lasing in a single nanowire with quantum dots. *Nature Photonics*, 9(8):501–505, 2015.

[69] JW Ma, Woo-Jung Lee, Jung Min Bae, Kwang-Sik Jeong, Seung Hoon Oh, Jeong Hun Kim, S-H Kim, J-H Seo, J-P Ahn, Hyoungsub Kim, et al. Carrier mobility enhancement of tensile strained si and sige nanowires via surface defect engineering. *Nano letters*, 15(11):7204–7210, 2015.

[70] Pierre-David Szkutnik, Anna Sgarlata, Adalberto Balzarotti, Nunzio Motta, Antoine Ronda, and Isabelle Berbezier. Early stage of ge growth on si (001) vicinal surfaces with an 8° miscut along [1 1 0]. *Physical Review B*, 75(3):033305, 2007.

[71] Hyeong-Chai Jeong and Ellen D Williams. Steps on surfaces: experiment and theory. *Surface Science Reports*, 34(6):171–294, 1999.

[72] Jean-Noël Aqua, Thomas Frisch, and Alberto Verga. Nonlinear evolution of a morphological instability in a strained epitaxial film. *Physical Review B*, 76(16):165319, 2007.

[73] Chaouqi Misbah, Olivier Pierre-Louis, and Yukio Saito. Crystal surfaces in and out of equilibrium: A modern view. *Rev. Mod. Phys.*, 82:981, 2010.

[74] William W Mullins. Theory of thermal grooving. *Journal of Applied Physics*, 28(3):333–339, 1957.

[75] Junkyo Suh, Ryosho Nakane, Noriyuki Taoka, Mitsuru Takenaka, and Shinichi Takagi. Highly strained-sige-on-insulator p-channel metal-oxide-semiconductor field-effective transistors fabricated by applying ge condensation technique to strained-si-on-insulator substrates. *Applied Physics Letters*, 99(14):142108, 2011.

[76] Y Jiang, N Singh, TY Liow, GQ Lo, DSH Chan, and DL Kwong. Reduced carrier backscattering in heterojunction sige nanowire channels. *Applied Physics Letters*, 93(25):253105, 2008.

[77] D Fathy, OW Holland, and CW White. Formation of epitaxial layers of ge on si substrates by ge implantation and oxidation. *Applied physics letters*, 51(17):1337–1339, 1987.

[78] Thomas David, Abdelmalek Benkouider, Jean-Noël Aqua, Martiane Cabie, Luc Favre, Thomas Neisius, Marco Abbarchi, Meher Naffouti, Antoine Ronda, Kailang Liu, et al. Kinetics and energetics of ge condensation in sige oxidation. *The Journal of Physical Chemistry C*, 119(43):24606–24613, 2015.

[79] JP Dismukes, L Ekstrom, and RJ Paff. Lattice parameter and density in germanium-silicon alloys1. *The Journal of Physical Chemistry*, 68(10):3021–3027, 1964.